AGGREGATION AND TRANSPORT KINETICS OF CRUDE OIL AND

SEDIMENT IN ESTUARINE WATERS

A Dissertation

by

MICHAEL CONROY STERLING, JR.

Submitted to the Office of Graduate Studies of
Texas A&M University
in partial fulfillment of the requirements for the degree of

DOCTOR OF PHILOSOPHY

December 2003

Major Subject: Civil Engineering

AGGREGATION AND TRANSPORT KINETICS OF CRUDE OIL AND

SEDIMENT IN ESTUARINE WATERS

A Dissertation

by

MICHAEL CONROY STERLING, JR.

Submitted to Texas A&M University
in partial fulfillment of the requirements
for the degree of

DOCTOR OF PHILOSOPHY

Approved as to style and content by:

James S. Bonner	Aydin Akgerman
(Chair of Advisory Committee)	(Member)
Robin L. Autenrieth	Paul Roschke
(Member)	(Head of Department)
Andrew N.S. Ernest	
(Member)	

December 2003

Major Subject: Civil Engineering

ABSTRACT

Aggregation and Transport Kinetics of Crude Oil

and Sediment in Estuarine Waters. (December 2003)

Michael Conroy Sterling, Jr., B.S., University of Oklahoma;

M.S., Texas A&M University

Chair of Advisory Committee: Dr. James S. Bonner

Modeling the transport and fate of spilled crude oil is important for estimating short and long-term toxicity effects in coastal ecosystems. This research project investigates the partitioning of hydrocarbons from a surface crude oil slick, the resurfacing of chemically dispersed crude oil droplets, the suitability of in-situ field instruments for oil and sediment characterization, and the aggregation and settling of dispersed oil and suspended sediments.

An initial laboratory study was conducted to investigate apparent hydrocarbon solubility in petroleum/water systems. Mixing shear and initial crude oil layer thickness were related empirically to oil entrainment rate. A model describing hydrocarbons partitioned in colloidal and soluble phases was consistent with experimental data. A second laboratory study was conducted to investigate the influence of coalescence kinetics on mean droplet size and resurfacing rate of chemically dispersed crude oil droplets. Increased mean shear rates resulted in mean droplet diameters and oil resurfacing rates. A third laboratory study was conducted to compare particle size and fractal dimension measurements obtained using a submersible flow cytometer, an

electrozone particle counter, and a light scattering particle sizer. Measured particles included latex beads, crude oil, clay, crude oil-clay aggregates, and crude oil-silica aggregates. Tested instruments gave consistent size measurements for all particle systems, suggesting their suitability for sizing marine particles.

To describe the aggregation kinetics of oil-sediment systems, a modified Smoluchowski model based on coalesced sphere (CS) assumptions was developed. Observed collision efficiency values (α_{OBS}) were related to collision efficiency values for single particle type systems (α_{HOMO}) and those for two particle type systems (α_{HET}) using a probabilistic approach. For clay and crude oil, α_{HOMO} values were higher than the α_{HOMO} value for silica. Clay-oil and silica-oil have similar α_{HET} values. Thus, crude oil can significantly increase the aggregation rates of noncohesive sediments such as silica.

The CS model above was modified to incorporate sediment fractal geometry. The ability of this modified coalesced fractal sphere (mCFS) model to fit experimental data sets was better than that of a coalesced sphere (CS) model. Because of their reduced settling rates, sediments with lower fractal dimension form more aggregate with dispersed oil.

DEDICATION

To my wife, Kenyatta, who is proof positive that at times in life you get more than you dreamed of and a lot better than you deserve. She's my friend, my confidant, my motivation, my teacher, my advisor and the love of my life. She's a big part of why I am here today.

ACKNOWLEDGMENTS

A great deal of support and cooperation was required to complete this project. I thank Dr. Jim Bonner, my committee chair, for the guidance, inspiration, suggestions, criticism and support given throughout the course of this investigation. I also thank Dr. Robin Autenrieth for her support and counsel during this work. I thank Dr. A. Ernest and Dr. A. Ackerman for their patience and time commitment as committee members.

In addition to my committee members, a number of others helped in the completion of this work. I thank Dr. Tom McDonald and Don Golden for their support and help with petroleum chemistry analysis. I also thank Dr. Cheryl Page for her project suggestions and her conscientious manuscript review. I thank the Texas General Land Office (TGLO) and the Texas Water Resources Institute (TWRI) for their financial support. Further, I thank all my colleagues and fellow lab workers in Environmental Engineering for their friendship, support, and generosity.

Finally, a very special thanks goes to my parents, family, church family, and friends for years of patience, affection, and encouragement.

TABLE OF CONTENTS

LIST OF TABLES

LIST OF FIGURES

CHAPTER I
INTRODUCTION

STATEMENT OF PURPOSE

Petroleum poses a range of environmental risks when released into the environment. Although the sources of petroleum input to the sea are diverse, they can be categorized effectively into four major groups: natural seeps, petroleum extraction, petroleum transportation, and petroleum consumption (National Research Council (NRC), 2003). Natural seeps are purely natural phenomena that occur when crude oil seeps from the geologic strata beneath the seafloor to the overlying water column. Petroleum extraction can result in releases of both crude oil and refined products as a result of human activities associated with efforts to explore for and produce petroleum. Petroleum transportation releases range from major spills associated with tanker accidents such as the Exxon Valdez to relatively small operational releases that occur regularly. Inputs due to petroleum consumption results from sources as varied as the human activities that consume petroleum. In North America, the largest and best known natural seeps appear to be restricted to the Gulf of Mexico and the waters off of southern California, regions that also have extensive oil and gas production (NRC, 2003). Releases due to petroleum transportation and petroleum consumption are less restricted geographically (NRC, 2003).

The style and format of this thesis follows that of Water Research.

In addition to physical impacts of large crude releases, the toxicity of many of the individual compounds contained in petroleum is significant. Compounds such as polycyclic aromatic hydrocarbons (PAHs) are known human carcinogens and occur in varying proportions in crude oil and refined products (NRC, 2003). Federal legislation including the Oil Pollution Act of 1990 requires the development of effective contingency plans to limit environmental and economic impacts of spills resulting from petroleum extraction and transportation. Understanding the relative effects of oil spill countermeasures on the transport and toxicity of spilled oil aids in development of these plans. Chemical dispersants are an oil spill countermeasure being investigated for nearshore marine oil spill response. Besides a lower cost of implementation than most mechanical responses, other touted benefits include increased biodegradation due to higher bioavailability and greater solubility in water, limiting coagulation with suspended sediment. Understanding the transport and resulting toxicity of crude oil requires an understanding of the oil entrainment and vertical transport in the water column. When spilled at sea, oil often forms minute droplets, ranging from tens to hundreds of microns. Crude oil constituents, such as PAHs, partition between the dispersed oil droplets and the surrounding water (Figure 1.1). In addition, these droplets may coalesce or aggregate with suspended aquatic particles, impacting the transport of resulting aggregates (Figure 1.1). System hydrodynamics and salinity are expected to influence the PAH partitioning and aggregation kinetics within these dispersions. In-situ instrumentation is desired for real time field monitoring and for transport model calibration.
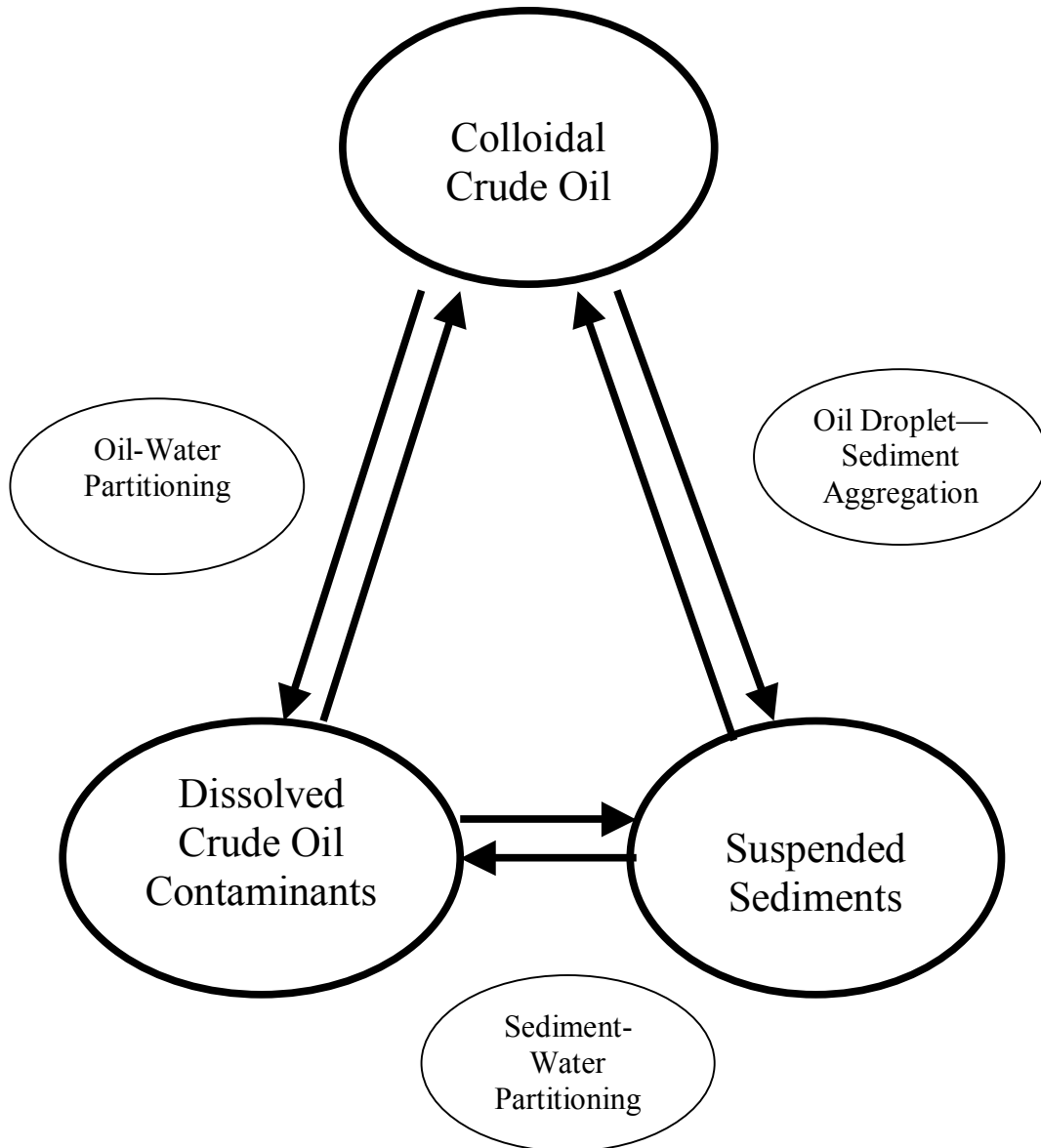
Figure 1.1. Distribution of crude oil constituents in the water column

BACKGROUND

Catastrophic oil spills often occur in near shore regions, affecting coastal ecosystems (Bartha and Atlas, 1977). According to a 1987 U.S. Coast Guard report (USCG, 1987), ports and harbors, river channels, and open sheltered waters receive the vast majority of oil spills, in contrast to offshore areas. Texas has 2360 miles of shoreline and two of the country's top 10 ports, Houston and Corpus Christi. These ports handle 50% of the nation's crude oil import, while 80% of Corpus Christi's commerce is petroleum related. As a consequence, Texas coasts are particularly vulnerable to disastrous spills.

After crude oil enters the aquatic system, the mixing conditions in the natural water impact both the size distribution and chemical composition of entrained oil droplets. Differences in chemical makeup as a function of droplet size will be reflected as a difference in bioavailability (Shaw and Reidy, 1979). Colloidal oil droplets that could be taken up as food by filter feeders and small grazers, while dissolved oil constituents could enter the circulatory system through the gills of all animals. In fish, hydrocarbons taken up through the gut from food are deposited in the liver, whereas hydrocarbons absorbed from water preferentially accumulates in muscle tissue. Thus, it is possible that differences in the form of entrained oil may result in kinds of oil exposures with markedly different biochemical and physiological consequences.

One portion of this research investigates the effects of mixing shear and initial slick thickness on crude oil entrainment rate and droplet size distribution. A laboratory study was conducted in which the chemical composition and droplet size distributions of

the oil-water dispersions were analyzed at different levels of mean shear rates and initial oil loadings. Because of the controlled nature of the investigation, insights on the relationship between subsurface generated shear and oil entrainment were gained. In addition, a model describing oil constituent partitioning at these conditions can be applied for toxicity or chemical partitioning studies in laboratory apparatuses.

To counter potential environmental damages resulting from crude oil spills, chemical dispersants are being investigated for nearshore marine oil spill response. Besides a lower cost of implementation than most mechanical responses, other potential benefits include increased biodegradation due to higher bioavailability and greater dispersion in water, limiting shoreline deposition (Page *et al.*, 2000b). However, nearshore environments can vary significantly in mixing energy and salinity, two parameters that are likely to impact dispersed oil droplet coalescence and vertical transport.

To investigate the potential impacts of the nearshore environment on dispersant effectiveness, a laboratory study was conducted to determine the effects of salinity and mixing energy on dispersed crude oil coalescence. Size distribution of dispersed oil droplets in water has been noted as an important measure of dispersant effectiveness. Mackay *et al.* (1986) used in their model the concept of a critical oil droplet diameter, above which most oil will resurface and below which most oil remains dispersed (NRC, 1989). The higher the mixing energy, the larger this critical droplet diameter will be (NRC, 1989). However, Mackay's model does not detail mechanisms of droplet interactions or predict likely droplet size distributions as required for conserved mass

based models.   For this research, the dispersed oil resurfacing process was modeled using a vertical transport and particle aggregation model. The significance of vertical oil transport has been demonstrated in field, laboratory, and modeling studies (Delvigne and Sweeney, 1988; Reed *et al.*, 1999a). Quantifying oil entrainment is important not only for mass balance calculations, but also in determining spatial and temporal distribution of oil on the sea surface.

In terms of oil spill response, technological advances have led to an evolution of oil spill monitoring instrumentation. The simplest is basic areal visual monitoring, in which trained observers photograph the oil plume, estimate the actual dispersion, and the sheen reappearance. More sophisticated monitoring can be conducted using a variety of analytical instrumentation coupled with the actual collection of oil samples throughout the treatment areas at specified depths of the water column. Traditionally, single wavelength fluorometry has been used in monitoring the dispersion of a spilled crude oil slick. The fluorescence principle is based on the ability of a compound (aromatic hydrocarbons) to be subjected to a specific wavelength of light (excitation) and to re-emit this light at one, or more, higher wavelengths (emission). The wavelengths are registered as peaks. The measured fluorescence is a direct indicator of the hydrocarbon concentration. The aromatic hydrocarbon concentration is used as a proportional indicator of total hydrocarbons, which is then displayed as parts per million (ppm).

One portion of this research investigates the use of in-situ particle sizers/counters as an alternate means to monitor crude oil dispersion. Nearly all of the dispersed oil volume exists in the water column as entrained droplets. For a light scattering particle

sizer, a laser beam, formed by collimating the output of a diode laser, illuminates the droplets. Scattering by droplets is detected in the focal plane of a receiving lens. Fraunhoffer light scattering theory is used to estimate the droplet size distribution. For an optical particle counter, droplets pass through a focusing tube, magnified using a microscope objective, and digitally photographed. Through analysis of the digital images, size distributions are determined.

With appropriate instrumentation, models describing oil coalescence and aggregation with suspended sediment can be calibrated. A number of authors have presented state of the art reviews of oil spill models (Spaulding, 1988; ASCE, 1996; Reed *et al.*, 1999a). While simple two dimensional trajectory models remain most common, three-dimensional trajectory and fate models that include simulation of response actions are being developed (Reed *et al.*, 1999b). Interest in developing three-dimensional models has been stimulated by efforts to quantify toxicology risks to aquatic organisms. Vertical transport and dispersion algorithms model key processes in three-dimensional transport models. Yet, the empiricism upon which these algorithms have been created limit the prediction of chemical dispersion impacts, especially outside the applicable range of the empirical relationships.

Dispersion models based on the work of Delvigne and Sweeney (1988) have become standard, used in the ADIOS model (NOAA, 1994), the SINTEF oil weathering (Aamo *et al.*, 1993; Daling *et al.*, 1997), OSCAR (Reed *et al.*, 1995a,b; Aamo *et al.*, 1997a,b), and OILMAP (Spaulding *et al.*, 1992). This approach may significantly affect model behavior by assuming that droplets below a certain threshold diameter (70-150

um) are presumed to be permanently dispersed (Lunel, 1993). This assumption is true if the magnitude of vertical turbulent motions is high compared with the rise velocity of the droplets. Delvigne and Sweeney (1988) achieved a significant advance in algorithms for natural dispersion, but the resulting equation is strictly a curve fit, with no grounding in fundamental physics or dimensional analysis.

Published descriptions of spill response models are few. Reed *et al.* (1995b, 1999a) and Aamo *et al.* (1997a,b) describe the oil spill contingency and response model OSCAR, developed specifically as a tool for quantitative comparison for oil spill response strategies. Model couples weathering, surface trajectory, water column, and oil spill response components. Application of chemical dispersants is simulated based on observations from field trials (Daling *et al.*, 1995; Lewis *et al.*, 1995). However, this is a limited dataset, which does allow predictability of dispersant effectiveness or droplet behavior in nonsimilar environmental situations.

Few algorithms describing oil-sediment interactions have been published. A coastal oil spill model, COZOIL (Reed *et al.*, 1989; Howlett, 1998) includes a relatively thorough representation of oil-sediment interactions occurring in a surf zone. These interactions are coastline deposition and removal processes. The model also uses highly parameterized equations, which do not attempt to directly describe governing processes.

This research describes oil-sediment aggregation and resulting deposition using a series of advection-dispersion-reaction equations with the aggregation reaction described with modified Smoluchowski kinetics. An initial modeling effort was based on coalesced sphere (CS) assumptions and an observed collision efficiency term derived

based on a probabilistic approach. A second modeling effort incorporated the fractal character of the sediment. Experimental results were analyzed using the revised model, a modified coalesced fractal sphere (mCFS) model, and the CS model. This approach reduces the number or required model parameters and incorporates interactions between suspended sediment and entrained oil droplets.

RESEARCH OBJECTIVES

This project will investigate PAH partitioning and aggregation kinetics in crude oil-sediment systems. The specific objectives, represented by three experiments and two modeling studies, were the following:

1. To estimate the relative partitioning of PAHs between entrained crude oil droplets and the surrounding water phase. Because of the weathering process, only slightly soluble hydrocarbons are available for dissolution from the surface oil. Thus, it is expected that a significant portion of the hydrocarbons are present in a colloidal phase.

2. To evaluate the effects of mean shear rate and salinity on crude oil coalescence and resurfacing rates. Salinity and pH effects on crude oil interdroplet repulsion energy were measured. Collision efficiencies and coalescence rates were estimated using an aggregation kinetic model. Resurfacing rates were estimated using a vertical transport model.

3. To validate the performance of three particle sizing/counting instruments for determining sizes of latex beads, dispersed oil, clay aggregates, oil-clay aggregates, and oil-silica aggregates. Latex beads and dispersed oil

systems have spherical forms that are handled straightforwardly by instrument software. The remaining systems are expected to exhibit a fractal character that would highlight material differences in the sizing techniques.

4. To use modified Smoluchowski coalesced sphere (CS) model to describe multiple particle type aggregation, including that of oil and suspended sediment. The model is used to estimate the homogeneous coalescence efficiencies of crude oil droplets, silica particles, and clay aggregates and the heterogeneous collision efficiencies of crude oil-silica aggregates and crude oil-clay aggregates.

5. To develop a modified coalesced fractal sphere (mCFS) model to describe multiple particle type aggregation, including that of oil and suspended sediment. The fit with experimental data is compared between mCFS and CS models. The effect of fractal dimension on the aggregation and aggregate settling rates is determined.

CHAPTER II

PARTITIONING OF CRUDE OIL POLYCYCLIC AROMATIC

HYDROCARBONS IN ESTUARINE WATERS

OVERVIEW

This chapter investigates the hypothesis that observed polycyclic aromatic hydrocarbon (PAH) concentrations in an aqueous system are equal to the sum of the organic phase and soluble phase molar concentrations. While the organic phase concentrations are proportional to the PAH mole fraction in the oil, the soluble phase molar concentrations are estimated using Raoult's law. A batch laboratory mixing vessel with a scalable mixing energy was loaded initially at various oil layer thicknesses (0.4 – 3.2 mm) which correspond to oil surface loadings (40—310 mg/cm^2). The vessel was agitated at constant mean shear rates (G_m = 5, 20 s^{-1}). Total petroleum hydrocarbon (TPH) samples were taken periodically to estimate the entrainment rate as a function of initial oil layer thickness. TPH concentrations were measured in-situ using a laser scattering instrument (LISST-100) and ex-situ using gravimetric analysis. At a steady state TPH concentration (>72 hrs), additional samples were analyzed for PAH concentration using GC/MS analysis. TPH concentrations increased over time according to a first order kinetic model. Generally, the first order rate constant and steady state concentration both increased with increased oil loading and with increased G_m. In addition, measured PAH concentrations correlated well (r^2 > 0.96) with those predicted

by the hypothesized model. These results are useful for assessing the effects of mixing and oil loading conditions on crude oil PAH partitioning.

INTRODUCTION

In a surface spill, oil first forms a slick that is then broken into smaller droplets and entrained in the water column. This entrainment can result from primarily physical factors such as wind, currents, and wave action, or from chemical factors such as the addition of surfactant based chemical agents. Once entrained, oil can be truly dissolved, or form particles in the form of emulsions, or can associate with organic or inorganic materials (Neff, 1979). For this research, oil compounds existing in the water column on a molecular level are defined as "dissolved". Alternatively, larger oil droplets with radii of tens to hundreds of microns are defined in this research as "colloidal". The organisms that reside in the water column are susceptible to chemical uptake in some or all of these forms that oil can assume.

Understanding the dissolution of PAHs is critical for estimating exposure, uptake, and bioaccumulation by affected organisms (Neff, 1979). Due to their nonpolar, hydrophobic nature, PAH solubilities are relatively low. PAHs are generally less soluble in aqueous salt solutions such as seawater than in pure water (Xie *et al.*, 1997). The solubility behavior of a compound in a complex mixture such as crude oil may not correspond to that predicted from pure component data (Banerjee, 1987). The aqueous solubility of individual PAHs decreases when they are part of a mixture because the pure component has a stronger affinity for the non-polar oil phase than the water (Shiu *et al.*, 1990). Lee *et al.* (1992 a, b) described the partitioning of PAHs into water from diesel

fuel and coal tars using a Raoult's law convention for solute activity coefficients and assuming ideal behavior. Page *et al.* (2000a) applied the same modeling paradigm in describing partitioning of PAHs into water from crude oil.

Because the form of the oil impacts its toxicity and transport, it is important to understand the inception criteria for oil droplet entrainment into the water column. Several different mechanisms for the production of the turbulence responsible for mixing at density interfaces have been studied. These mechanisms include surface jets, bottom currents, oscillating grids, and a surface stress. Absolute comparisons between these methods are uncertain due to the variety of length and velocity scales used in different geometries (Turner, 1973). However, the choice of length and velocity scales does not influence the shape of the logarithmic entrainment plot. Thus, many mixing geometries can be used to determine an entrainment relation.

Conventionally, mean shear rate, G_m, has been used as a scaling parameter to relate laboratory and large scale manifestations of physical phenomena caused by fluid shear. In natural water systems, entrainment and mixing result primarily from wind and current stresses. G_m values range on the order of 0.1-10 s^{-1} for deep sea and lake systems and on the order of 1-50 s^{-1} for river and estuarine systems (Delvigne and Sweeney, 1988).

Because of the complexity of oil chemistry, empirically determined mixing laws may not be applicable to contaminant toxicity tests in batch mixing tests. In previous studies, tracer dyes or single component hydrocarbons were used to estimate entrainment in fluid dynamics studies. The surfactants in crude oil may cause significant deviations

from the expected entrainment. Therefore, the objectives of this investigation were to estimate the relative amounts of dissolved and colloidal phase oil present in the water column within a range of G_m values. Specific tasks included (1) empirically relating surface oil entrainment rates to G_m and surface oil loading and (2) estimating the concentration of PAHs for a range of mean shear rates and surface tensions in a baffled stirred tank. Experimental results indicate that the presence of surfactant components in crude oil influences the onset entrainment energy and the partitioning of PAHs in water appears to follow the hypothesized partitioning model. These combined findings can be used to model the exposure regime in a baffled stirred tank reactor. Furthermore, this work yields insights on the influence of current shear on crude oil entrainment in natural aquatic systems.

BACKGROUND

Turbulent Entrainment

The observed rate of oil entrainment can be viewed as parallel processes: the dispersion of oil from the surface slick entering the water column and the resurfacing of entrained droplets larger than a critical size due to their buoyancy. This exchange can be described by the following differential equation:

$$\frac{d\phi}{dt} = r_{ent} + r_{resurf}, \quad \phi(0) = \phi_o$$
$$r_{ent} = k(\phi_{s.s.} - \phi)$$
$$r_{resurf} = k'(\phi)$$

(2.1)

where ϕ, ϕ_o, and $\phi_{s.s.}$ are the actual, initial, and steady state volume fractions and k and k'

are the entrainment and resurfacing rate constants. Equation 2.2 is the general solution

of equation 2.1

$$\phi(t) = \frac{k\phi_{s.s.}}{k-k'} - \left(\frac{k\phi_{s.s.}}{k-k'} - \phi_o\right)e^{-(k-k')t}$$
(2.2)

As t approaches $t_{s.s.}$, then $\phi(t)$ becomes approximately equal to $\phi_{s.s.}$. This implies that k

>> k', and equation 2.2 simplifies to the following:

$$\frac{\phi(t) - \phi_{s.s.}}{\phi_o - \phi_{s.s.}} = e^{-kt}$$
(2.3)

Values of k were estimated by using nonlinear least-squares regression of equation 2.3.

Apparent PAH Solubility

At steady state, it is assumed that oil in the water column exists in an aqueous

solution in two separate forms, dissolved and colloidal. The concentration of a given

chemical dissolved in the aqueous phase (C_i) can be described by Raoult's Law (Eq.

2.4):

$$C_i = X_i S_i$$
(2.4)

where X_i is a chemical's dimensionless mole fraction in the organic phase and S_i is the

aqueous solubility of the pure hydrocarbon contaminant liquid in water (in mol/L).

Although the O/W emulsion is not an ideal system, Raoult's Law is used as an

approximation to solution behavior. The colloidal concentration of a given hydrocarbon

contaminant in the aqueous phase can be described by equation 2.5:

$$C_i = \frac{\phi X_i}{\upsilon}$$
(2.5)

where ϕ = volume fraction of oil emulsion in water (vol emulsion/vol water), and υ = average molar volume of component in the oil. Combining equations 2.4 and 2.5 provides an equation (Page *et al.*, 2000a) which can be used to attain the total observed aqueous contaminant concentration (mol/l) for a given component i:

$$C_i = \frac{\phi X_i}{\upsilon} + X_i S_i \qquad (2.6)$$

EXPERIMENTAL APPROACH

Surface Tension Measurements

  The surface tension of water with a Medium Arabian crude oil film was measured using a computer controlled and user programmable tensiometer (KSV Sigma70, Helsinki, Finland). A platinum/iridium alloy DuNouy Ring was used as the measurement probe. Measuring vessels and probe were rinsed with methylene chloride. Before each measurement, the probe was flamed using a Bunsen burner. A nominal volume of crude oil (1-10 ml) was added to the surface of 20 ml of synthetic sea water (salinity = 30 ‰).

  The surface tension is estimated by measuring the interaction of the platinum ring with the surface being tested. The ring is below the interface and subsequently raised upwards. As the ring moves upwards, it raises a meniscus of the liquid. Eventually, this meniscus tears from the ring and returns to its original position. Prior to this event, the force exerted passes through a maximum value and begins to diminish prior to the actually tearing event. The calculation of surface tension is based on the measurement of this maximum force.

Entrainment Apparatus

The reactor configuration used for this experiment is a derivative of the Phipps & Bird jar test apparatus. The rectangular reactor vessel has internal dimensions of 20 in. x 10 in. x 12 in., which provides a nominal working volume of 32-L. The reactor and its internals have been constructed from ½ in thick Plexiglas and assembled using solvent welding. A series of sampling ports and a drain port have also been fitted to the reactor.

As with the jar test apparatus, the reactor configuration is agitated using a stainless steel mixing impeller. The mixing energy transferred to the reactor fluid by impeller rotation at a given speed was determined using a torquemeter. The impeller is composed of four cylindrical rods evenly staggered throughout the depth of the reactor. This impeller design, along with the addition of side baffles and internals of the reactor ends increase the uniformity of reactor mixing.

An in-situ laser scattering particle sizer (LISST-100, Sequoia Instruments, Richmond, WA) was installed through one end wall of the reactor. This instrument can be used in bench scale as well as field scale measurements. Incorporating this instrument in the reactor design allowed measurement of droplet size distributions and total volume concentration.

Entrainment Measurements

Entrainment experiments were conducted to determine the influence of oil loading on the entrainment kinetics at a pair of G_m values. For each entrainment experiment, the chamber was filled with 32-L of artificial seawater, made from distilled deionized water and Instant Ocean (Aquarium Systems, Mentor, OH). For the

entrainment kinetics measurements, a nominal oil volume (100, 200, or 400 mL) was

added to the reactor as above. At the entrainment G_m, four 250 mL samples were taken

periodically throughout the experiment duration (> 72 hr). The aqueous samples were

drawn from a port situated at the mid-height of the reactor. During sampling, the motor

controlling the impeller continued to rotate until all sampling for chemical and physical

analysis was complete. Prior to sampling, approximately 50-ml was drawn through the

sampling port to clear any potential blockages. A 250-ml water sample was drawn

through the sampling port. This sample for petroleum analysis was collected in pre-

cleaned amber bottles with Teflon-lined lids. The pH of the samples was immediately

lowered to pH 2 by adding approximately 25-30 drops of 0.1 N hydrochloric acid (HCl)

to inhibit any biological growth. The pH of the sample was verified by testing the

sample with litmus paper. The samples were immediately refrigerated until they were

extracted for chemical compound analysis; sample processing was conducted within 1

week of sampling.

One of the samples (250 ml) drawn was analyzed for immediate emulsion

volume fraction determination using an electronic particle counter (Coulter Counter

Multisizer and Sampling Stand II). Emulsion volume fractions were measured using (1)

an in-situ laser scattering particle sizer (LISST-100, Sequoia Instruments, Richmond,

WA) and (2) an electrozone particle counter (Coulter Counter Multisizer and Sampling

Stand II, Miami, FL). Emulsion volume fractions were measured every 5 minutes using

the LISST-100. Emulsion volume fractions also were measured periodically using the

Coulter Counter Multisizer. A 140-μm diameter aperture and a 2000 μl sample volume

were used in Coulter Counter measurements. After the experimental run was concluded, the reactor was drained, cleaned using a mixture of Simple Green and water, and rinsed thoroughly with distilled water.

Three of the 250 mL samples were solvent extracted for petroleum analysis as described below and analyzed gravimetrically (Mills *et al.*, 1999). The samples were spiked with surrogate recovery standards and transferred to separatory funnels for extraction using methlyene chloride, using accepted procedures as per USEPA Method 413.1. The sample extract was concentrated to approximately 1 ml by evaporative concentration (TurboVap II Concentration Workstation, Zymark, Hopkinton, MA). The concentrated extract was reconstituted to a final volume of 5 ml and refrigerated until analysis. The samples were analyzed using the method described by Page *et al.* (2000a). For compound analysis, a 1-μL aliquot of the extracted sample was injected into a Hewlett-Packard 5890 Series II gas chromatograph (GC) interfaced to a Hewlett-Packard 5972 mass selective (MS) detector and operated using Hewlett-Packard MS Chemstation software. This quantitative method is for the determination of PAHs and their alkylated homologues in extracts of water. Quantitation is performed by capillary gas chromatography/mass spectrometry (GC/MS) in selected ion monitoring mode (SIM). Running the sample in SIM can lower detection limits for PAH dramatically from those achieved by normal full scan. SIM sets the Mass Selective Detector to scan a few selected ions rather than a full spectrum.

RESULTS AND DISCUSSION

Entrainment Kinetics

A series of entrainment kinetic measurements were conducted at $G_m = 5$ and 20 s^{-1} for oil surface loading ranging from 76—304 g/cm^2 ($d_{oil} = 0.8 - 3.2$ mm). Time series data from each set of measurement conditions were fit to equation 2.6 to estimate k and ϕ_{ss}. The averaged estimations of k and ϕ_{ss} for each experimental condition are presented in Figures 2.1 and 2.2, respectively. The error bars in these figures represent one standard deviation. Figure 2.1 shows that for a given oil surface loading, increased G_m values result in significantly higher entrainment rates. However, for the tested G_m values, oil surface loading does not significantly impact entrainment rate. This pair of findings suggest that fluid velocity is the dominant factor influencing entrainment rates.

Figure 2.2 shows that for a given oil surface loading, increased G_m values result in significantly higher ϕ_{ss} concentrations. However, the influence of oil surface loading on ϕ_{ss} concentrations is more complex. At $G_m = 5$ s^{-1}, ϕ_{ss} at $d_{oil} = 0.8$ mm is significantly lower than ϕ_{ss} at $d_{oil} = 1.6$ mm or at $d_{oil} = 3.2$ mm. Conversely, there is not a significant difference in the ϕ_{ss} values at $d_{oil} = 1.6$ mm or at $d_{oil} = 3.2$ mm. Similar trends occur at $G_m = 20$ s^{-1}. However, at $G_m = 20$ s^{-1}, the ϕ_{ss} concentrations at oil depths 1.6 and 3.2 mm are two orders of magnitude higher than that at oil depth 0.8 mm. These results suggest an interaction effect of fluid velocity and oil depth on the steady state entrainment concentration.
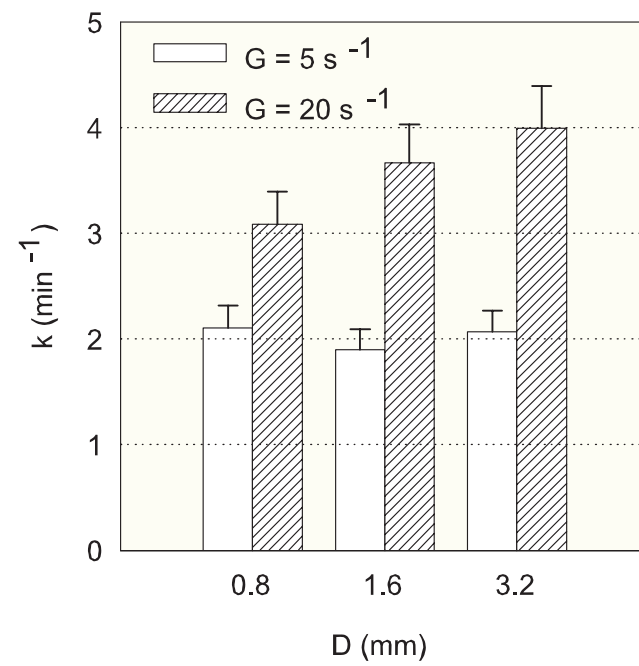
Figure 2.1. First order entrainment rate constants (k) at initial oil layer thickness (D)
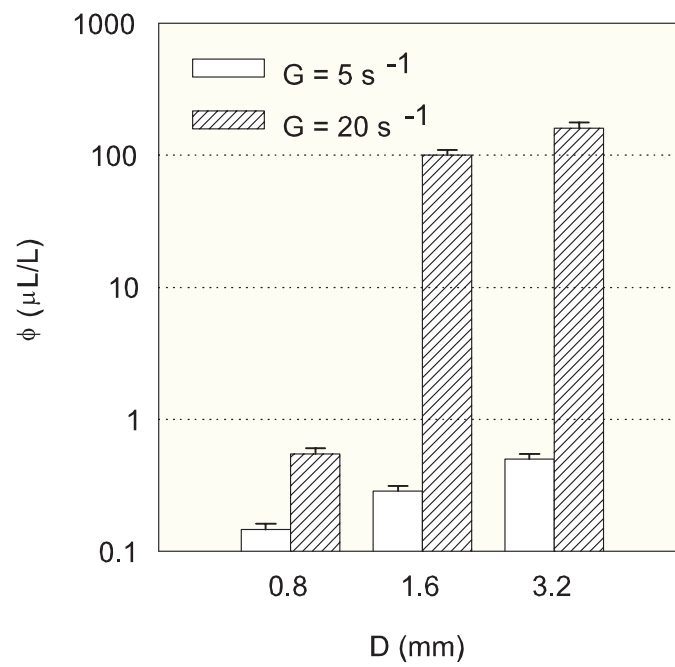
Figure 2.2. Steady state entrainment concentrations (ϕ_i) at initial oil layer thickness (D)

The presence of natural surfactants in crude oil is one potential reason for the results exhibited in Figure 2.2. Because of the polar constituents of surfactants, these compounds prefer to orient at the oil-water interface. As a result, increasing the concentration of crude oil surfactants up to the critical micelle concentration (CMC) reduces the water surface tension. Above the CMC, the surface tension remains constant.

Surface tension measurements were conducted in order to find the relationship between oil layer thickness and surface tension. The surface tension dependence on the surfactant concentration for the concentrations below CMC can be described by the Gibbs adsorption equation:

$$\Gamma = \frac{-1}{RT} \frac{d\gamma}{d \ln C_{surf}} \qquad (2.7)$$

where γ is the surface tension, R is the gas constant, T is the temperature, Γ is the surface excess of the surface active compound, and C_{surf} is the surfactant concentration. For a given crude oil sample and measurement vessel, C_{surf} and vessel cross-sectional area A_{cs} are constant. Therefore, C_{surf} is related to the oil layer thickness D_{oil} by the equation 2.8:

$$D_{oil} \propto C_{surf} \qquad (2.8)$$

Combining equations 2.7 and 2.8 relates surface tension and oil layer thickness:

$$\Gamma = \frac{-1}{RT} \frac{d\gamma}{d \ln D_{oil}} \qquad (2.9)$$

The results from surface tension measurements are presented in Figure 2.3.
Plotted points are averages of the data points for each measurement, while the error bars
indicate the range for each data point. One regression line was drawn through the points
in which the surface tension decreases with increased oil depth. A second regression line
was drawn through the data points in which the surface tension remains constant with oil
depth. The intersection of these regression lines corresponds to the critical depth (D_{crit})
at which the surfactant concentration reaches CMC. For the crude oil studied, D_{crit} is
1.61 ± 0.05 mm while Γ is 2.48 ± 0.52 $\mu mol/m^2$. This result means that for the lowest oil
layer depth tested in the kinetic entrainment study ($d_{oil} = 0.8$ mm), the oil-water interface
was not saturated with surfactant. This suggests that this interfacial surface was more
resistant to entrainment than those at the higher oil loadings.

For dimensional analysis, the entrainment rate k could be expressed as

$$k = f\left(\gamma, G_m, \rho_{H_2O}, l\right) \tag{2.10}$$

where ρ_{H2O} is the water density and l is a characteristic length. For this study, the tank
depth was chosen as the characteristic length as this scale corresponds with that used to
determine G_m. Using the Buckingham Pi method, the following dimensionless
parameters were determined:

$$\pi_1 = \frac{k}{G_m} \tag{2.11}$$

$$\pi_2 = \frac{\rho_{H_2O} G_m^2 l^3}{\gamma} \tag{2.12}$$
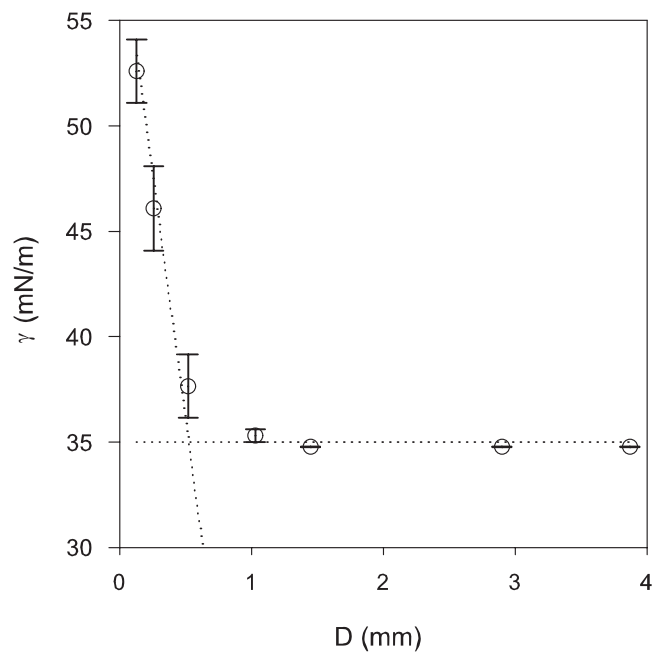
Figure 2.3. Effect of oil layer thickness (D) on interfacial tension (γ)

Equation 2.11, a ratio of oil entrainment and shearing time scales, is the reciprocal of a modified mass Peclet number. Equation 2.12, a ratio of the inertial force of the water and the interfacial force, is a Weber number. Figure 2.4 illustrates that data from this experiment fit the power relationship $\pi_1 = A\pi_2^b$, where A and b are empirically determined parameters. The values for the A and b were found to be 0.1036 ± 0.0341 and 0.2974 ± 0.0436, respectively.

While this entrainment relation may be generalized across many laboratory apparatuses, its direct application for field measurements is limited for two reasons. Because of the impact of winds in coastal and some estuarine environments, it may be difficult to separate entrainment due to wave breaking from that of current shear. A second limitation resulted from the confined tank volume which disallows oil spreading. This restrictions on spreading allowed a higher interfacial surfactant concentration than may be expected in an unconfined field setting. Despite these limitations, this laboratory work is relevant as it allowed controlled conditions for elucidating entrainment mechanisms. The entrainment relation can be incorporated into modeling work and field data analysis to separate entrainment effects from wave breaking and current shear. In oil spill models, this entrainment relation can be coupled with an oil slick spreading algorithm to estimate changes in entrainment rate over time. A number of empirical relations for entrainment resulting from wave breaking and for oil slick spreading have been utilized in oil spill modeling (Reed et al, 1999a; ASCE, 1996). Future studies will be conducted to estimate the influence of oil characteristics (i.e., oil
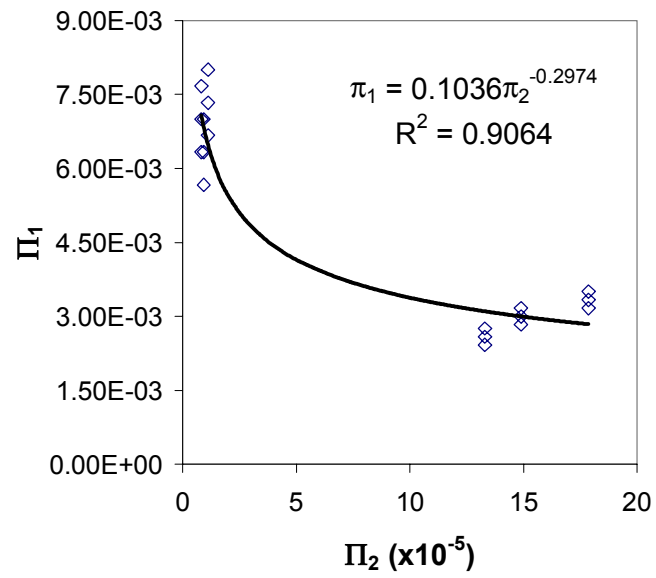
Figure 2.4. Normalized entrainment rate ($\Pi_1 = k/G_m$) versus Weber number ($\Pi_2 = \rho_{H2O}G_m^2 l^3/\gamma$)

density and viscosity, weathering state, temperature) and of additives such as surfactants on shear entrainment parameters.

Apparent PAH Solubility

The second phase of this study is to determine whether Raoult's law can be used to estimate PAH solubility. Equation 2.6 was used to estimate the expected concentration of a given PAH in the water. Values for ϕ ,X_i, and S_i were determined from ϕ_{ss}, oil fingerprint analyses, and literature values respectively. Table 2.1 lists the PAH concentrations and solubilities used for these calculations. As expected, the larger molecular weight PAHs have smaller concentrations in the oil and lower aqueous solubilities.

Figure 2.5a shows that at $G_m = 5$ s^{-1}, naphthalene concentrations did not increase with increased oil loading. Under the same conditions, TPH concentrations increased although the emulsion volume concentration remained on the order of 1 ppm. The same effect was noted by Page *et al.* (2000a) who reasoned that under relatively low emulsion volume fractions, the influence of PAH solubility dominates the observed PAH concentration. Thus, at a relatively low G_m where the entrained volume fraction is minimized, the observed PAH concentrations may be predicted primarily using Raoult's law.

Figure 2.5b shows that at $G_m = 20$ s^{-1}, naphthalene concentrations were constant and the methyl-substituted naphthalenes increased with increased oil loading. Under these conditions, TPH concentrations increased from 1 ppm to 100 ppm. With this large increase in entrained volume fraction, the observed PAH concentration is

Table 2.1. Selected physicochemical properties for the PAHs investigated

PAH Analyte	PAH MW[a]	Component Fingerprint[c] ($\mu g_i/mg_{oil}$)	Component mole fraction (X^o)	Water Solubility[b] (mol_i/L_{H2O})
Naphthalene	128	0.15	4.688E-04	2.477E-04
C1-Naphthalenes	142	0.93	2.620E-03	1.882E-04
C2-Naphthalenes	156	2.59	6.641E-03	3.822E-05
C3-Naphthalenes	170	2.69	6.329E-03	1.000E-05
Biphenyl	154	0.02	5.195E-05	4.870E-05
Acenaphthene	154	0.01	2.597E-05	2.253E-05
Fluorene	166	0.04	9.639E-05	1.193E-05
Dibenzothiophene	184	0.21	4.565E-04	5.598E-06
Anthracene	178	0	0.000E+00	4.213E-07
Phenanthrene	178	0.08	1.798E-04	6.011E-06
Pyrene	202	0.07	1.386E-04	3.663E-10
Benz(a)anthracene	228	0	0.000E+00	5.702E-12
Benzo(k)fluoranthene	252	0	0.000E+00	5.159E-14
Benzo(e)pyrene	252	0	0.000E+00	2.976E-13
Benzo(a)pyrene	252	0	0.000E+00	2.976E-13

[a] Lee *et al.*, 1992. [b] Solubility at salinity = 30 . [c] Taken from GC/MS analysis.
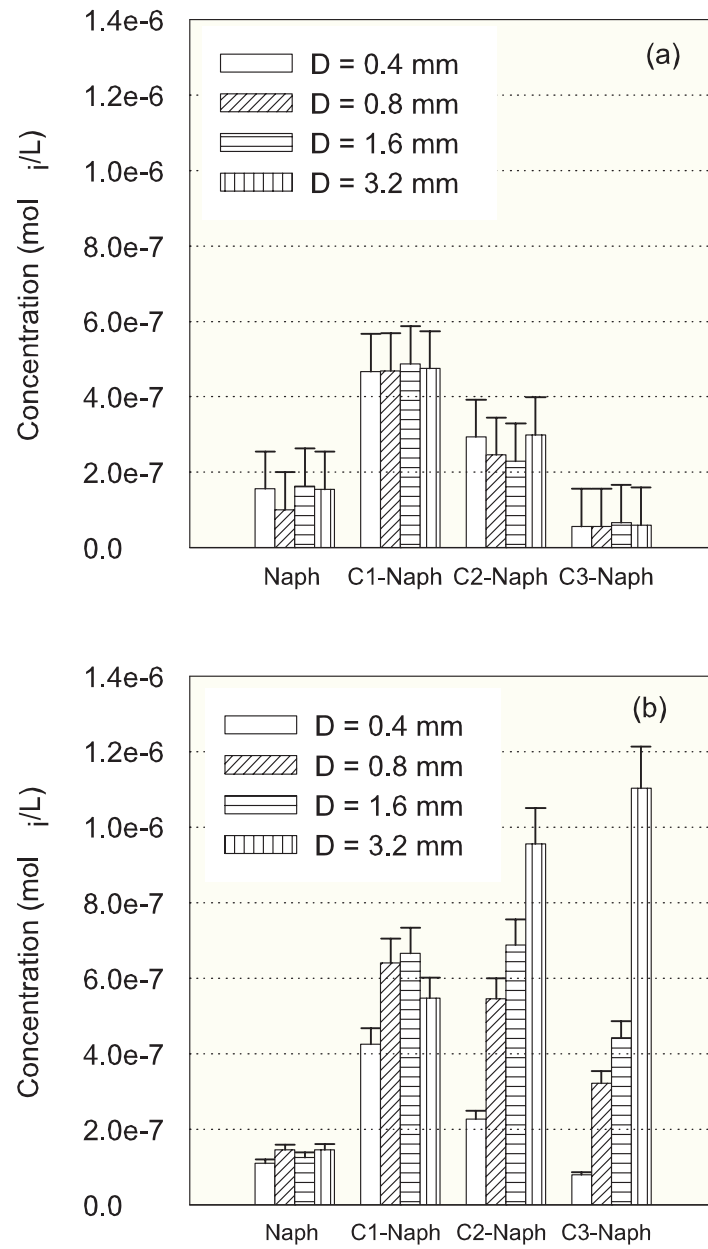
Figure 2.5. Naphthalene concentration at (a) $G_m = 5s^{-1}$ and (b) $G_m = 20s^{-1}$

influenced primarily by the PAH mole fraction in entrained oil colloids. These results were consistent with those obtained by Page *et al.* (2000a).

Equation 2.6 relates the crude oil PAH composition (X_i), emulsion volume fraction (ϕ_i), and PAH solubility (S_i) to the observed PAH concentration in an aquatic system. Figure 2.6 compares predicted PAH aqueous concentrations and those measured during the laboratory partitioning studies. The error bars shown in Figure 2.6 for the laboratory measured concentrations represent the standard errors calculated from replicate averages. The best fit line through the data occurs at MW_{oil} of 400 g/mole. For $G_m = 5s^{-1}$ and $G_m = 20 \ s^{-1}$, the r^2 values were 0.96 and 0.99, respectively. Deviations from the 1:1 line were likely due to errors in experimentally determined values.

Confidence in the C_i values predicted using equation 2.9 is dependent on several factors other than the premise of ideal behavior, including uncertainty about the input parameters (e.g., ϕ_i, MW_{oil}, ρ_{oil}, X_i, and S_i). Errors associated with experimentally determined values, including ϕ_i, ρ_{oil}, and X_i, were estimated using replicate measurements. Errors in a given S_i value would have resulted in a bias at low emulsion volume fractions.

Figures 2.7a and 2.7b highlight the fraction of naphthalenes present due to colloid entrainment. As the compound molecular weight increases, the relative fraction of the compound in the colloidal phase increases. This occurs regardless of the level of oil entrainment. This has significant implications for the fate and transport of crude oil PAHs in natural aquatic systems. In most natural systems, significant entrainment is expected.
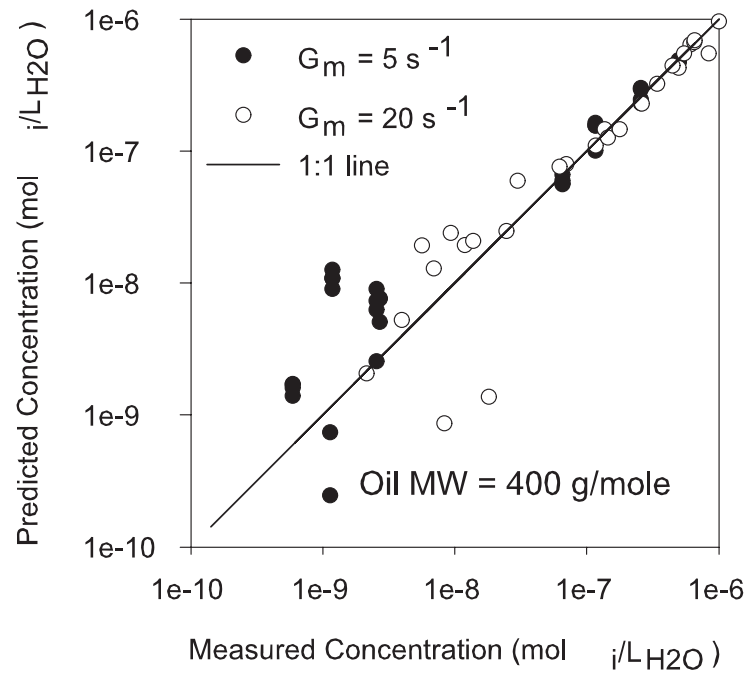
Figure 2.6. PAH concentrations: model predictions versus measured values
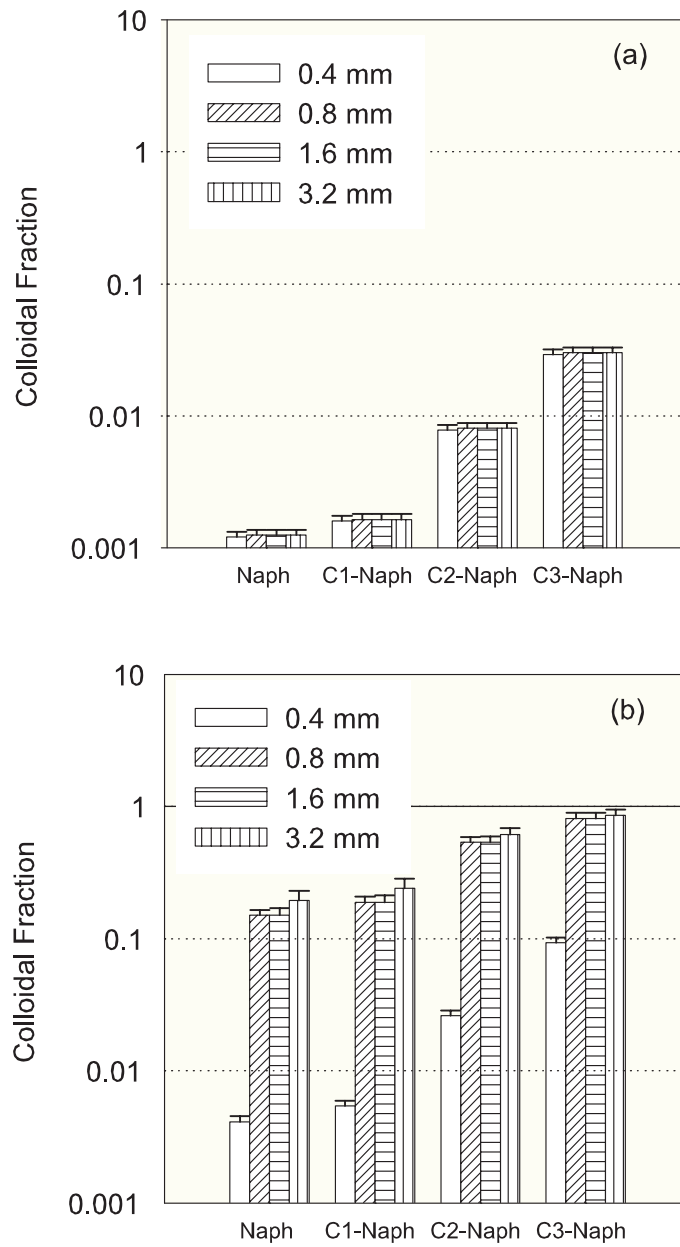
Figure 2.7. Fraction of naphthalene concentration due to colloidal entrainment at (a) $G_m = 5s^{-1}$ and (b) $G_m = 20s^{-1}$

Thus, the majority of PAH transport would be coupled to the transport of entrained oil droplets. Consequently, for toxicity calculations, the predominant exposure mechanisms should be centered on colloidal uptake. In laboratory toxicity systems, the level of entrainment can be controlled. Thus, mechanistic studies investigating the relative impacts of soluble and colloidal fractions on aquatic toxicity can be conducted.

CONCLUSIONS

Experiments were conducted to develop a shear entrainment relation using an impeller agitated tank and to verify a partitioning model for PAHs in aquatic systems. For the entrainment measurements, entrainment data was fit to a power law expression. In addition, measured TPH concentrations were fit to a first order kinetic equation in order to compare entrainment rates and steady state entrainment concentrations. Below a threshold mean shear rate, TPH concentrations increase with increased oil loading. However, naphthalene concentrations remain constant due to low colloidal entrainment and relatively high naphthalene solubility. Above a threshold mean shear rate, TPH and naphthalene concentrations both increase due to increased colloidal entrainment. The interdependence of mean shear rate and oil surface loading on entrainment rates was explained using the Gibbs interfacial adsorption model. These results are useful for assessing the effects of mixing and oil loading conditions on crude oil PAH partitioning.

CHAPTER III

CHEMICAL DISPERSANT EFFECTIVENESS TESTING: INFLUENCE OF DROPLET COALESCENCE

OVERVIEW

Thermodynamic and kinetic investigations were performed to determine the influence of coalescence of chemically dispersed crude oil droplets in saline waters. For the range of pH (4-10) and salinity (10, 30, 50 ‰) values studied, ζ-potential values ranged from -3 to -10 mV. As the interaction potential values calculated using Derjaguin-Landau-Verway-Overbeek (DLVO) theory were negative, the electrostatic barrier did not produce significant resistance to droplet coalescence.

Coalescence kinetics of premixed crude oil and chemical dispersant were determined within a range of mean shear rates ($G_m = 5, 10, 15, 20$ s^{-1}) and salinity (10, 30 ‰) values. Coalescence reaction rates were modeled using Smoluchowski reaction kinetics. Measured coalescence efficiency values ($\alpha=0.25$) suggest insignificant resistance to coalescence in shear systems. Experimentally determined dispersant efficiencies ($\alpha=0.25$) were 10-50% lower than that predicted using a non-interacting droplet model ($\alpha=0.0$). Unlike other protocols in which the crude oil and dispersant are not premixed, salinity effects were not significant in this protocol. This approach allowed the effects of dispersant-oil contact efficiency ($\eta_{contact}$) to be separated from those of water column transport efficiency ($\eta_{transport}$) and coalescence efficiency ($\eta_{coalescence}$).

INTRODUCTION

Oil spilled on the surface of a water body consists of a floating surface slick and of suspended oil droplets in the water column. While simple two-dimensional trajectory models remain common, three-dimensional trajectory and fate models that include simulation of oil spill response actions are being developed (ASCE, 1996; Reed *et al.*, 1999a). Because of oil buoyancy, vertical transport also may be significant in modeling oil plume trajectory. If Stokes law governs vertical transport of dispersed crude oil droplets, coalescence kinetics can significantly impact the oil-resurfacing rate. This is because the vertical velocity is proportional to the square of the droplet diameter.

Nearshore environments can vary significantly in mixing energy and salinity, two parameters that likely impact droplet coalescence kinetics and transport. The dominant causes of mixing energy are wind and current stresses. The energy dissipation in an estuary ranges from 10^{-1}-10^{0} W/m^{3}, which is lower than the dissipation expected in the oceanic surface layer (10^{0}-10^{1} W/m^{3}) (Delvigne and Sweeney, 1988). Variations in salinity in nearshore systems are caused by dilution of seawater (30 ‰) with freshwater inputs from rivers or evaporation from stagnant lagoons.

The influences of mixing energy and salinity are not fully understood for chemical dispersion of crude oil. Dispersion is the net result of three separate processes: initial globulization, in which the formation of oil droplets occurs under the influence of wave action, water column transport, which results from kinetic energy of the oil droplets supplied by the wave action and buoyancy forces, and coalescence of the oil droplets. Chemical dispersants enhance the dispersion process by reducing the oil-water interfacial tension, increasing the initial globulization. The observed efficiency (η_{obs}) of

the chemically enhanced crude oil dispersion depends on the efficiency of each of the dispersion processes. The dispersant-oil contact efficiency ($\eta_{contact}$) can limit the initial globulization. Sea state as well as dispersant application procedure both impact $\eta_{contact}$. Size distribution of dispersed oil droplets influences the water column transport efficiency ($\eta_{transport}$). Mackay *et al.* (1986) used in their model the concept of a critical oil droplet diameter, above which most oil will resurface and below which most oil remains dispersed (Reed *et al.*, 1999a; NRC, 1989). The higher the mixing energy, the larger this critical droplet diameter will be (NRC, 1989).

The influence of coalescence in dispersant efficiency ($\eta_{coalescence}$) has not been documented explicitly for chemically dispersed crude oil. However, a number of authors have examined the effects of droplet interactions on the coalescence rate in dilute emulsions of micrometer-sized droplets (Lobo *et al.*, 1993; Danov *et al.*, 1994; Dukhin *et al.*, 2001). Experimental and theoretical investigations show that during the approach of two micrometer-sized droplets, a flat liquid film can appear between their closest regions (Edwards *et al.*, 1991; Exerowa and Kruglyakov, 1998). Hydrodynamic interactions as well as DVLO and non-DVLO interactions can be involved in film formation, thinning, and rupture (Danov *et al.*, 1993a; Danov *et al.*, 1993b; Denkov *et al.*, 1993; Valkovska *et al.*, 1999). While these previous experimental investigations have focused on simple oils and surfactants, this study involves a complex hydrocarbon droplet (crude oil), mixed surfactants (chemical dispersant), and salts as present in a coastal crude oil release.

Therefore, the objectives of this investigation were to study (1) the effects of salinity and pH on droplet interaction energy and (2) the effects of salinity and mixing energy on the resurfacing and coalescence rates of chemically dispersed crude oil droplets. In thermodynamic studies, ζ-potential values for chemically dispersed crude oil droplets were determined for a range of salinity and pH values. Interpotential energy values were calculated using DLVO theory. In kinetic studies, mean shear rate (G_m), a scaling parameter used in designing field flocculators, was used to characterize the mixing energy in the laboratory reactor. Observed droplet distributions were fit to a transport-reaction model to estimate collision efficiency (α) values and their dependence on salinity and mixing energy. Using the calibrated transport-reaction model, hydrodynamic influences of droplet collision mechanisms were compared. Finally, observed dispersant efficiency (C/C_o) and droplet distributions obtained were compared with those obtained using other laboratory testing apparatus.

COALESCENCE KINETICS MODEL DESCRIPTION

The basis of the current theories used in modeling changes in droplet size distribution dates back to the work by Smoluchowski (1917). The aggregation kinetic rate (r_k) of dispersed oil droplets is described using the Smoluchowski coalescence equation, presented in the following discretized form:

$$r_k = \frac{1}{2} \sum_{i+j=k} \alpha\beta(v_i, v_j) n_i n_j - \sum_{i=1}^{\infty} \alpha\beta(v_i, v_j) n_i n_k \tag{3.1}$$

where α is the droplet collision efficiency (fraction of collisions that result in droplet coalescence, $\beta(\bullet v_i, v_j)$ and $\beta\bullet(v_i, v_k \bullet\bullet)$ are the collision frequencies between droplets with volumes of v_i and v_j and v_i and v_k, n is the droplet number concentration in a size

interval, and *i,j* are subscripts designating droplet size class. The first term of Equation 3.1 represents the formation of droplet size *k* by collision of droplets size *i* and *j*. The second term represents the loss of droplet size *k* by collision with all other droplets. The ratio of ½ in front of the first term is needed to avoid double counting (Ernest *et al.* 1995).

The collision efficiency factor (α) is generally believed to represent the chemistry involved in the coalescence, and the collision frequency, β, has been considered a function of system hydrodynamics. The collision frequency is modeled as the sum of collision frequencies due to the Brownian (β_{Br}), shear (β_{Sh}), and differential sedimentation (β_{ds}) mechanisms (Ernest *et al.*, 1995). Brownian mechanisms predominately describe collisions between droplets with diameters smaller than 1 µm. Differential sedimentation dominates collisions of droplets with diameters greater than 100 µm. Collisions between intermediate sized droplets are described using shear mechanism.

The developed coalescence kernel can be combined with the vertical dispersive and buoyant transport terms to produce a system of equations to describe droplet resurfacing:

$$\frac{\partial C_k}{\partial t} = D_z \frac{\partial^2 C_k}{\partial z^2} - w_k \frac{\partial C_k}{\partial z} + \theta_k \qquad (3.2)$$

where C_k is the volume concentration ($=n_k v_k$), z is the vertical distance from the top of the batch reactor, w_k is the rising velocity of droplets in size class *k*, θ_k is the coalescence

rate in terms of volume concentration ($=r_k v_k$), and other terms are the same as above.

The rising velocity was described using Stokes law:

$$w_k = \frac{g(\rho_{oil} - \rho_{water})d_k^2}{18\mu_{water}}$$

(3.3)

where g is the gravitational constant, d_k is the diameter of the droplets in size class k,

μ_{water} is the viscosity of the water, and ρ_{oil}, ρ_{water} are the densities of the oil droplets and

water, respectively. While Stokes Law may approximately describe rising velocity for

the micron sized droplets in this study, more accurate expressions for rising velocity

would be required for larger droplets (Zheng and Yapa, 2000). Total dispersed oil

concentrations are calculated by the following summation:

$$C_{oil} = \sum_{i=1}^{k} C_i$$

(3.4)

The major assumptions included in this formulation come from Smoluchowski's

equation and the coalesced sphere assumption, and can be summarized as follows: (1)

only binary collisions of droplets are considered; (2) droplet splitting is neglected; (3) α

is constant in the system and independent of droplet size; (4) the droplet collision

mechanisms are modeled using the coalesced sphere assumption; and (5) the collision

functions are based on the rectilinear motion assumption, which neglects the curvilinear

effects due to hydrodynamic and inter-particle forces between colliding droplets

discussed by Han and Lawler (1992). Research by Lee *et al.* (2002) supported the

premise that rectilinear models predict particle aggregation more effectively than

curvilinear models in shear dominant systems.

The experimental system was modeled with an adsorptive top boundary and reflective (zero dispersive flux) bottom boundary (Bonner *et al.*, 1994; Ernest *et al.*, 1995):

$$w_k C_k = D_z \frac{\partial C_k}{\partial z} \quad @ \quad lower\ boundary$$

$$D_z \frac{\partial C_k}{\partial z} = 0 \quad @ \quad upper\ boundary$$

(3.5)

To solve the above system of partial differential equations, a set of initial droplet concentrations for each size range was required as the initial condition. The resulting system of equations were numerically integrated using a fourth order Runge-Kutta method.

EXPERIMENTAL APPROACH

Chemicals

Medium Arabian crude oil obtained from ExxonMobil (Alexandria, VA) was artificially weathered as described in Page *et al.* (2000b). Corexit® 9500 (ExxonMobil, Alexandria, VA), a hydrocarbon based chemical dispersant, was used in this study. It has increased effectiveness and similar toxicity to its predecessor and industrial "standard", Corexit® 9527 (Page *et al.*, 2000b). While the exact composition of Corexit® 9500 is proprietary, current dispersant formulations generally are a mixture of anionic surfactants such as sulfosuccinate esters and oxyalkylated C_{12}-C_{15} alcohols, non-ionic surfactants such as sorbitan monooleate and ethoxylated sorbitan monooleate, and hydrocarbon solvents such as ethylene glycol, glycol ethers, and nonaromatic hydrocarbons (George-Ares and Clark, 2000; NRC, 1989). Deionized water was passed

through a Barnstead water purification system with an ultrapurification unit for organic

matter/particulate removal, to obtain highly purified water with a resistivity of 18.1 MΩ-

cm. The salinity of the water was provided through the addition of simulated sea salt

(Instant Ocean, Aquarium Systems, Mentor, OH). For surface charge measurements, the

pH of solutions was adjusted using reagent grade NaOH and HCl.

Kinetic Testing Apparatus

The reactor configuration used for the kinetic measurements is a derivative of the

standard jar test apparatus. The rectangular reactor vessel has internal dimensions of 20

in. x 10 in. x 12 in., which provides a nominal working volume of 32-L. The reactor and

its internals have been constructed from ½ in thick Plexiglas and assembled using

solvent welding. A series of sampling ports and a drain port have also been fitted to the

reactor. As with the jar test apparatus, this reactor system is agitated using a stainless

steel mixing impeller. The impeller is composed of four cylindrical rods evenly

staggered throughout the depth of the reactor. This impeller design, along with the

addition of side baffles and internals of the reactor's ends increase the uniformity of

reactor mixing.

The mixing energy transferred to the reactor fluid by impeller rotation at a given

speed was determined using a torquemeter. The torquemeter is composed of a 12 VDC

motor, a torque transducer composed of strain gauges configured in a Wheatstone bridge

circuit, and a signal amplification circuit (Bonner *et al.*, 1994). After an initial

calibration in which voltage response is related to applied torque (Bonner *et al.*, 1994),

the torque meter was connected to the impeller, which was positioned in the reactor. For

a set of rotational speeds, the voltage response was recorded and converted to torque

values, according to the aforementioned calibration. The rotational speeds, ω, were measured using a digital tachometer. The values for power, P, transmitted to the water by the impeller was calculated using the following:

$$P = T\omega \tag{3.6}$$

Mean shear rates, G_m, were calculated for the reactor volume using the following (Camp and Stein, 1943):

$$G_m = \left(\frac{P}{\mu V}\right)^{\frac{1}{2}} \tag{3.7}$$

For $20 \leq \omega \leq 90$ rpm, the following empirical calibration resulted for this mixing system

$$G_m = (7.15\omega - 149.2)^{\frac{1}{2}} \qquad (r^2 = 0.99) \tag{3.8}$$

Time-series measurements of droplet size distributions were measured in-situ using a LISST-100 (Laser In-Situ Scattering and Transmissometry). The LISST-100 utilizes a 5 cm laser path length and measures angular scattering distribution obtained with a series of 32 ring detectors to observe particles in 1.25-250 µm size range over 32 logarithmically distributed size classes. Using in-situ measurements prevents alterations of droplet size distribution due to sampling handling and reduces labor requirements in acquiring a statistically accurate representation of droplet size distribution.

Electrophoretic Mobility (EPM) Measurements

A factorial experimental design was used to determine the effects of salinity (10, 30, 50 ‰) and pH (4-10) on the EPM of chemically dispersed crude oil droplets. A solution of 5 ml of crude oil and 0.5 ml of Corexit® 9500 was homogenized using a vortex mixer at low speed. One ml of the oil-dispersant mixture was added to 250 ml of

saline water prepared as in the coalescence kinetic experiments. The mixture was stored for approximately 12 hours before EPM measurements. Prior to conducting EPM measurements, the dispersed oil emulsion was agitated by inverting the capped storage bottle 5-6 times to ensure a homogeneous mixture. Ten ml of the emulsion is removed from this stock mixture, and the solution pH was adjusted using either 0.1 M NaOH or 0.1 M HCl. Droplet mobility was measured in a Rank Brothers Particle Micro-Electrophoresis Apparatus Mark II (Cambridge, England). For all measurements, the flat cell was used at $24^{o}C$ and 20V. Each mobility measurement was made using at least 10 droplets in each direction and averaging the result. Between samples, the glass flat cells used in the EPM measurements were cleaned with methylene chloride. They were then washed by a detergent solution and rinsed with water before being cleaned further in nitric acid solutions for at least 6 hours. Finally, the cells were rinsed with copious amounts of Barnstead purified water before use in subsequent measurements.

Coalescence Kinetic Measurements

A factorial experimental design was used to test the effects of salinity (10, 30 ‰) and mean shear rate (5, 10, 15, 20 s^{-1}) on the coalescence kinetics of chemically dispersed crude oil droplets. Other factors such as dispersant:oil ratio, oil loading, and temperature were held constant throughout the study.

To determine the coalescence kinetics, thirty-two liters of purified water and a nominal amount of sea salt were mixed in the reactor vessel and agitated for about 30 minutes at the experimental shear rate. The reactor salinity was measured using a refractometer. A solution containing 5 ml of crude oil and 0.5 ml of Corexit® 9500 was homogenized using a vortex mixer at low speed. Using a wide tipped pipette, the oil-

dispersant mixture was injected just below the water surface near the impeller shaft. The injection was completed within 2 seconds to model a single pulse input.

Dynamic droplet size distributions were measured using (1) an in-situ laser scattering particle sizer (LISST-100, Sequoia Instruments, Richmond, WA) and (2) an electrozone particle counter (Coulter Counter Multisizer and Sampling Stand II, Miami, FL). Droplet size distributions were measured every 5 minutes using the LISST-100. Droplet size and number distributions were measured at 0, 15, 30, 45, 60, 90, 120, 240, and 480 minutes using the Coulter Counter Multisizer. To limit measurement artifacts, a portion of the saline water composed for reactor fluid was used as the Coulter Counter electrolyte solution. In addition, a 400-μm diameter aperture and a 2000 μl sample volume was used in Coulter Counter measurements. This aperture allowed the measurement of the entire range of droplet sizes present in the reactor.

Total particle counts as measured by the Coulter Counter Multisizer were used to determine the total mass of dispersed oil present in the tank (non-resurfaced oil). The validity of this treatment was confirmed with gravimetric analyses in which the water samples were extracted with methylene chloride, the solvent was evaporated, and the resulting extract weighed. Mass values obtained using Coulter Counter measurements and gravimetric analyses agreed within 10%.

Values for collision efficiency, α, were determined using the parameter estimation algorithm by Ernest *et al.* (1991). This is a generic parameter estimation algorithm that minimizes the variation between predicted and observed data to reach an optimum parameter value. An initial parameter estimate and observed data are required as input. The accuracy of this estimate depends on this initial "guess", so initial values

of 0.1-0.9 in steps of 0.1 were used, covering the 0-1 range of possible collision

efficiency values. The "best" collision efficiency was determined by comparison of a

residual function (Ernest *et al.*, 1995). The lowest residual value (<1) indicated the

optimal results.

RESULTS AND DISCUSSION

Electrophoretic Mobility (EPM) Measurements

Selecting the appropriate relation to convert EPM values measured using

microelectrophoresis to ζ-potentials required estimating κa values. For all tested pH and

salinity values, the mean droplet diameter, a, observed was 17 ± 6 µm. Values for the

reciprocal Debye length, $\kappa \cdot (m^{-1}) \cdot$, was calculated using the following:

$$\kappa = \left(\frac{2000F^2}{\varepsilon_o \varepsilon_r RT} \right)^{\frac{1}{2}} \sqrt{I} \tag{3.9}$$

where F is Faraday's constant (9.649×10^4 C mol^{-1}), ε_o is the permittivity of free space

(8.854×10^{-12} C^2 J^{-1} m^{-1}) , ε_r is the relative permittivity of water (78), R is the gas constant

(8.314 J K^{-1} mol^{-1}), and T is the absolute temperature (298 K).

The ionic strength, I, was calculated using the following:

$$I = \frac{1}{2} \sum c_i z_i^2 . \tag{3.10}$$

where c_i is the molar concentration (mol L^{-1}) of ion i and z_i is the charge valency of ion i.

As all the κa values were greater than 250, the Helmholtz-Smoluchowski equation

(equation 3.11) gave a reliable estimate of the ζ-potential (Hunter, 2001),

$$\zeta = EPM \left(\frac{\mu_{H2O}}{\varepsilon_o \varepsilon_r} \right) \tag{3.11}$$

Figure 3.1 shows the influence of pH and salinity on the ζ-potential of chemically dispersed crude oil droplets. For all experimental pH and salinity values, the ζ-potential values were negative. In similar systems, negative surface charge has been attributed to the hydrogen bonding of OH$^-$ ions to the droplet surface (Marinova et al., 1996) or to the nonionic surfactant (Elworthy *et al.*, 1971). A portion of the negative charge likely resulted from the anionic surfactants present in the dispersant, as the ionic portion of the surfactant was oriented at the droplet surface toward the surrounding aqueous environment.

For a fixed pH value, ζ-potential values became marginally more negative with increased water salinity. Only small changes in ζ-potential resulted as the concentration of multivalent ions present in synthetic seawater was above the critical coalescence concentration (c.c.c) (Stumm and Morgan, 1995). Above the c.c.c., electrical repulsion energy in a colloidal dispersion has been minimized (Stumm and Morgan, 1995). Thus, changes in ζ-potential were likely due to other factors such as increased hydrogen bonding of negatively charged, polar species, i.e., HCO_3^- and SO_4^{2-}, or increased surface adsorption of anionic surfactants due to "salting-out" effects.
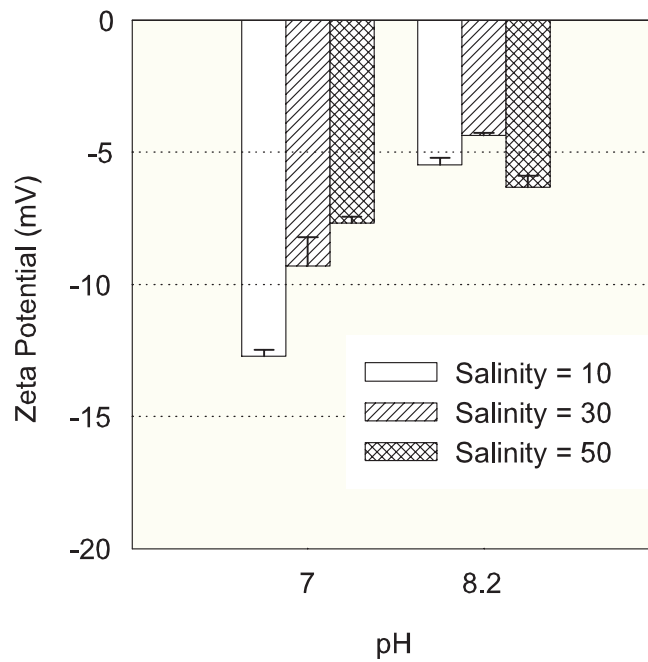
Figure 3.1. Measured zeta potential values of chemically dispersed crude oil droplets at selected pH values

To estimate the effect of pH and salinity on the interfacial interaction potential energy of dispersed oil droplets, potential energy curves between two droplets were calculated using DVLO theory as presented in equation 3.12:

$$V_{TOTAL} = V_A + V_B \tag{3.12}$$

V_A is attractive energy, due mainly to the van der Waals attractive force. For the case of two spherical droplets of radii a_1 and a_2 separated by a shortest distance H, the van der Waals attraction is given by

$$V_A = -\frac{A}{12}\left[\frac{y}{x^2 + xy + x} + \frac{y}{x^2 + xy + x + y} + 2\ln\left(\frac{x^2 + xy + x}{x^2 + xy + x + y}\right)\right] \tag{3.13}$$

where $x = H/(a_1+a_2)$ and $y = a_1/a_2$. The value of the nonretarded Hamaker constant, A, for this system was assumed to be 5×10^{-21} J.

V_R of equation 3.12 is the electrical repulsive energy. For the case of two spherical droplets of radii a_1 and a_2, Stern potentials, ψ_{d1} and ψ_{d2}, and a shortest distance H, between their Stern layers, equation 3.14 presented approximate values for V_R:

$$V_R = \frac{64\pi\varepsilon_o\varepsilon_r a_1 a_2 k^2 T^2 \gamma_1 \gamma_2}{(a_1 + a_2)e^2 z^2}\exp[-\kappa H] \tag{3.14}$$

where

$$\gamma = \frac{\exp\left[ze\psi_d / 2kT\right] - 1}{\exp\left[ze\psi_d / 2kT\right] + 1}. \tag{3.15}$$

Using measured zeta potential values and an estimated Hamaker constant (10^{-21} J), V_R and V_A values were calculated. The electrical repulsion V_R increased with increasing salinity (Table 3.1). The Debye length decreased from 0.96 nm at 10 salinity

units to 0.43 nm at 50 salinity units. However, the magnitude of ζ potential values

increased from 5 mV at 10 salinity units to 11 mV at 50 salinity units. In addition, the

magnitude of V_A values was at least an order of magnitude higher than that of the V_R

values for all measured salinities. Thus, as shown in Table 3.1, the net interaction values

varied less than 10% for the entire salinity range, and there was no significant energy

barrier to coalescence of dispersed oil droplets. Conversely, several workers have noted

that conventional dispersants did not function well in fresh water environments (salinity

< 5 ‰) (Fingas, 2000). However, the reduced effectiveness has been attributed to the

increased solubility of ethoxylated surfactants at reduced salinity (NRC, 1989).

Table 3.1. Calculated van der Waals interdroplet energy potential at salinity = 30 ‰

D (nm)	V_R (10^{-19}J)			V_A (10^{-19}J)
	5 mV	7 mV	11 mV	
0.5	2.19	4.29	7.08	-66.7
1.0	0.89	1.74	2.87	-33.3
1.5	0.36	0.71	1.17	-22.2
2.0	0.15	0.29	0.47	-16.7
2.5	0.06	0.12	0.19	-13.3
3.0	0.02	0.05	0.08	-11.1

Coalescence Kinetic Measurements

Figure 3.2 illustrates the influence of salinity and mixing energy on the collision efficiency of chemically dispersed oil droplets. Statistical comparisons of α values for a given mixing energy at 10 and 30 salinity values showed no significant difference ($P<0.05$). Thus, α was not dependent on the salinity within the range of salinity values tested. This result was not surprising given the insignificant differences in interdroplet potential V_T measured for the given salinity values. Therefore, salinity in brackish (10 ‰) or saline (30 ‰) waters should not influence the collision efficiency of the droplets at a given mixing energy.

In addition, comparisons of α values for a given salinity showed no significant difference ($P<0.05$). Thus, α was not dependent on the mixing energy within the range of values tested. This result was encouraging as it suggested that the hydrodynamic effects were captured effectively within the collision frequency kernel β and excluded from the collision efficiency parameter α.

Figure 3.3 shows the influence of mixing energy and salinity on dispersant effectiveness (C/C_o). As expected from the interdroplet potential data, salinity had no significant impact on dispersant effectiveness. However, increased mixing energy resulted in lower dispersant efficiencies due to increased frequency of droplet collisions β. Increased droplet coalescence resulted in larger droplets that subsequently resurface more quickly. Thus, the resulting concentration of dispersed oil in the reactor and the dispersant efficiency was reduced.
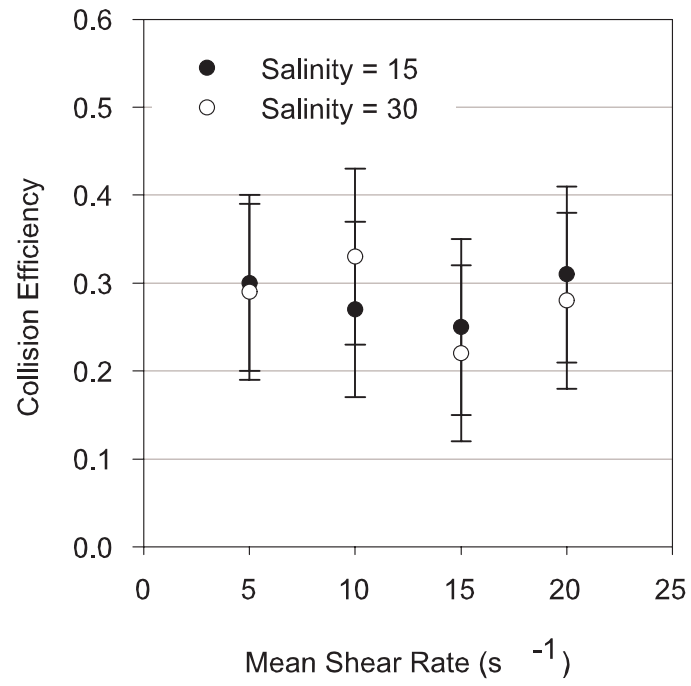
Figure 3.2. Effect of shear rate on collision efficiency
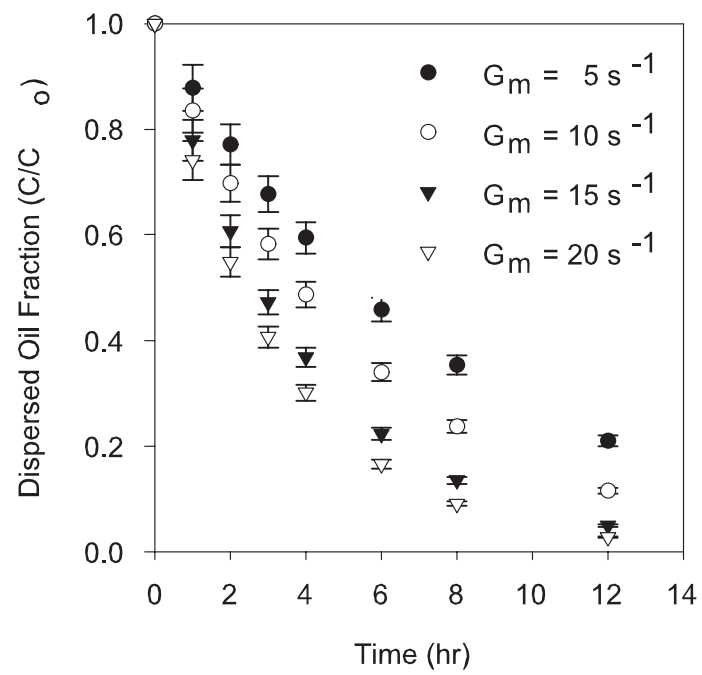
Figure 3.3. Effect of shear rate (G_m) on dispersed oil concentration

Figure 3.4 illustrates model predictions with (1) no droplet interactions allowed, (2) only differential settling, (3) only fluid shear, and (4) both differential settling and fluid shear permitted as droplet collision frequency mechanisms. The influence of Brownian motion (β_{Br}) was minimal due to the relatively large size of the oil droplets (diameter > 1 µm). While the relative dominance of fluid shear and differential settling is dependent on the dynamic droplet size distribution, droplet density, and shear levels, the primary collision mechanism is shear flocculation (β_{Sh}) at the shear levels of this experiment, with an smaller contribution presented by differential sedimentation (β_{ds}) (Ernest *et al.*, 1995, Lee *et al.*, 2002). Thus, quantifying the fluid shear level is necessary when investigating the transport of dispersed oil droplets under turbulent hydrodynamic regimes.

Coalescence in Observed Dispersant Efficiency

The significance of coalescence in determining the efficiency of chemical dispersion is illustrated in Figure 3.5, which compares the mass of oil dispersed in the water with and without droplet coalescence. In both the coalescence and non-coalescence ($\alpha = 0$) models, the disappearance of the largest droplets resulted from resurfacing losses. In addition to resurfacing losses, smaller droplets combined to form larger droplets that subsequently resurfaced. This loss of dispersed oil mass was illustrated by the decreasing area under the droplet size distribution curve at later times. Figure 3.5 highlights how the mean droplet size changed over time. Both in the coalescence and non-coalescence models, the observed mean droplet size decreased.
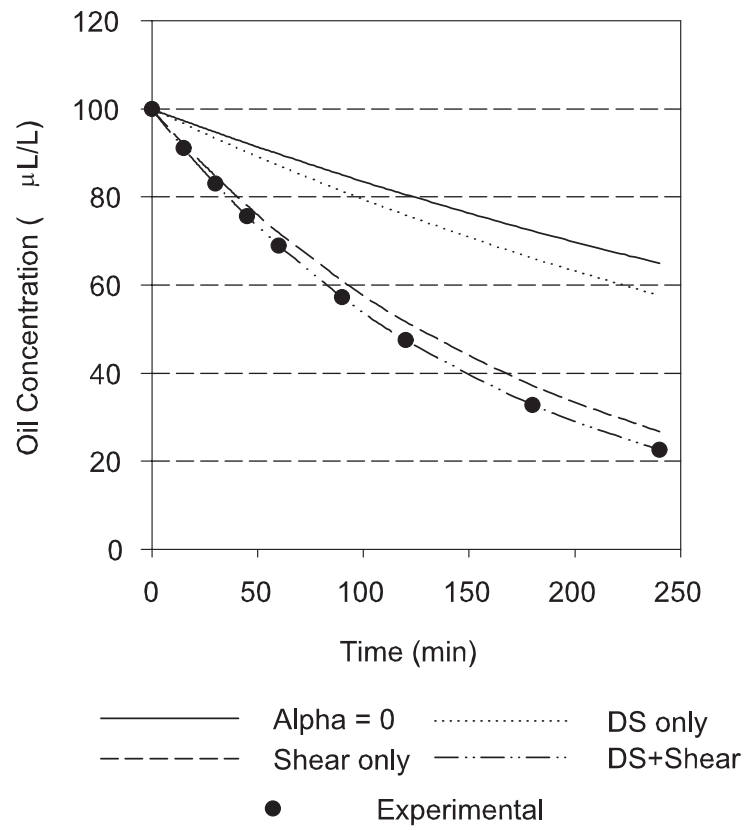
Figure 3.4. Influence of hydrodynamic mechanisms on oil droplet resurfacing
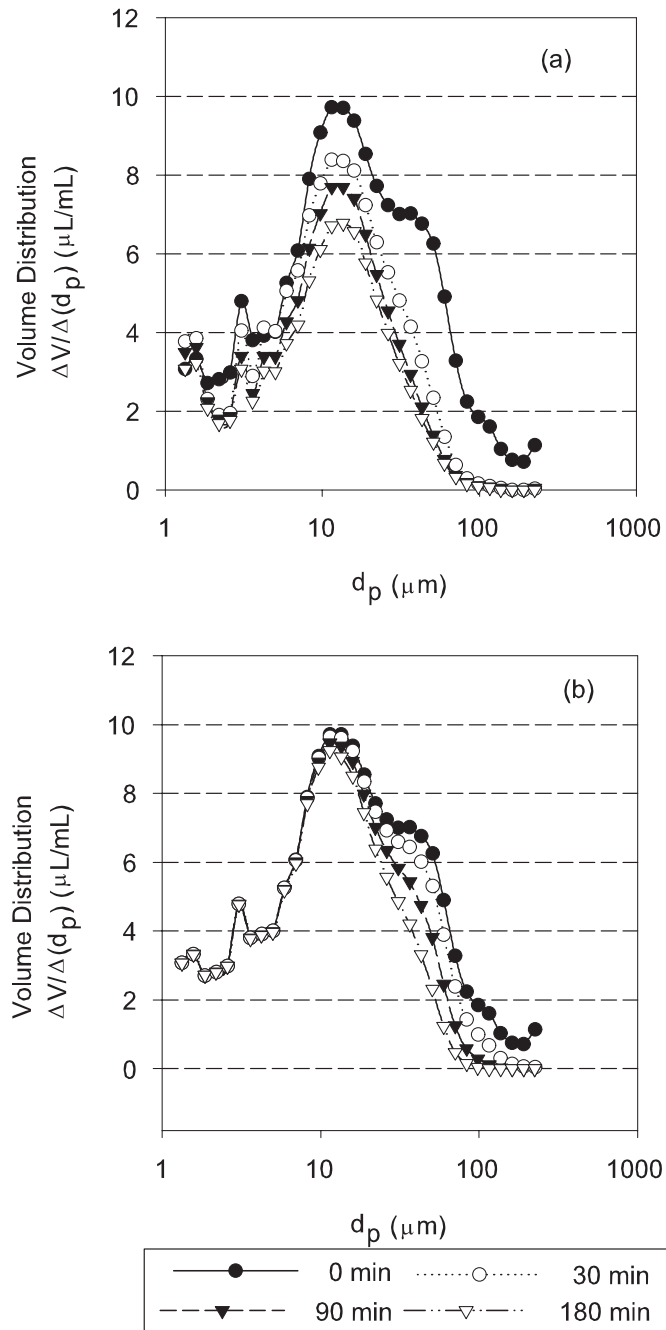
Figure 3.5. Evolution of droplet size distribution at $G_m = 20$ s^{-1}, salinity = 30 ‰ (a) collision efficiency = 0.25 (b) collision efficiency = 0.0

 However, in the coalescence model, the observed mean droplet size decreased faster as the resurfacing rate increased due to coalescence.

The relative unimportance of salinity in dispersant effectiveness testing was counter to results obtained using other apparatus and protocols. Using a swirling flask method, Fingas *et al.* (1994) found a distinct salinity-effectiveness interaction in three different dispersants, including Corexit®9527. Using a modified version of the swirling flask efficacy test, Blondina *et al.* (1999) determined that Corexit® 9500 was effective over a wide range of salinities. However, its effectiveness decreased sharply at salinity values below 15 ‰.

Likely, this apparent discrepancy was based on different operational definitions of dispersant effectiveness. Conceptually, chemical dispersion occurs in two stages: (1) contacting the crude oil and dispersant to form droplets and (2) the transport of the oil in the water column. The total dispersant efficiency (α_{total}) can be defined as the product of the contacting efficiency ($\alpha_{contact}$) and of the transport efficiency ($\alpha_{transport}$). As the oil and dispersant are generally added to the water sequentially in the swirling flask methods, these procedures measured efficiency defined as α_{total}. Similarly, because the oil and dispersant were premixed before being added to the water in this experiment, the $\alpha_{contact}$ values were closer to their maximum values of 1, resulting in a measured efficiency defined as $\alpha_{transport}$. The importance of the dispersant/oil mixing process was documented for a tank test in which different results were obtained by (1) premixing the oil and dispersant, (2) adding the dispersant neat to the oil, and (3) adding the dispersant in water solution (Mackay *et al.* 1984).   While a distinct disadvantage of premixing is that

it does not occur under normal application conditions, advantages include (1)
mechanistically separating the contributions of and to the overall dispersion efficiency
and (2) greater uniformity and reproducibility for toxicity studies (Wells *et al.*, 1984).

The importance of mixing energy in dispersant efficiency testing has been well
documented. In a comparison of common dispersant effectiveness protocols, Daling *et
al.* (1990) determined that swirling flask test (WSL) yielded lower efficiencies than
those of the constant agitation tank tests (IFP and MNS). A primary reason was the
WSL settling regime allowed droplets larger than 60 μm to resurface while the droplets
smaller than 100-125 μm remained dispersed in the tank tests studied. A rapid drop in
dispersant effectiveness with increased settling time was also noted by Fingas *et al.*
(1996). As the maximum droplet sizes measured in the present study are similar to those
of previous tank studies at comparable salinity (30 ‰), the hydrodynamic conditions
between this tank and those of previous tank studies seem comparable.

CONCLUSIONS

The interaction potential of chemically dispersed crude oil droplets was
determined using DVLO theory. Kinetic studies of chemically dispersed crude oil were
conducted with the resulting data synthesized into a modeling framework using a
parameter estimation algorithm as a calibration tool. The following conclusions may be
drawn from this work:

1. For salinity and pH values found in natural waters, the ζ-potential values of
   chemical dispersed crude oil were slightly negative. For a fixed pH value, ζ-
   potential values became marginally more negative with increased water

salinity. Using DLVO theory, no significant electrostatic energy barrier to droplet coalescence was present.

2. Within the tested experimental conditions, the collision efficiency parameter, α, was significantly greater than 0. This result suggests that coalescence kinetics were important in estimating dispersant efficiency in laboratory scale protocols and may be important in some coastal spills. Mean shear rate, G_m, was the dominant parameter in estimating observed coalescence rates and dispersant efficiency.

3. Salinity had a limited influence on effectiveness values measured in this protocol with premixed oil-dispersant compared with values measured in protocols with addition of dispersant to an oil layer. This suggests that salinity has a greater influence on initial droplet formation than on its subsequent entrainment.

CHAPTER IV

CHARACTERIZING SEDIMENT-OIL AGGREGATES USING IN-SITU INSTRUMENTS

OVERVIEW

The effects of emulsified crude oil and salinity (15, 30 ‰) on the steady state aggregate volume distributions and fractal dimensions were determined for a range of mean velocity gradients, ($G_m = 5\text{-}50$ s^{-1}). Aggregation was performed in a 40-L cylindrical tank with a 4-blade paddle mixer. Three-dimensional fractal dimensions (D_3) and volume distributions were determined using a procedure integrating data from an electrozone and an in-situ light scattering instrument. Two-dimensional fractal dimensions (D_2) and derived volume distributions were determined using a recently developed submersible flow cytometer equipped with a digital camera and image analysis software. For latex beads or emulsified crude oil systems, the above listed instruments yielded consistent size distributions and fractal dimensions ($D_2 = 1.92\pm0.16$, $D_3 = 2.94\pm0.12$). Mean volume aggregate diameters determined using the FlowCAM were consistently larger that those determined using the LISST-100 or Coulter Multisizer due to aggregate orientations during measurements. With increasing G_m values, all colloidal aggregates showed increasing D_3 values due to reduced aggregate length. Because of the compactness of all the aggregates ($D_3 > 2$), D_2 values remained constant at 2. Neither salinity nor sediment type significantly affected D_3 values calculated for sediment-crude oil aggregates. However, clay-oil aggregates showed

higher D_3 values than clay aggregates. This suggests that colloidal oil and mixing shear are the more dominant factors influencing aggregate morphology in nearshore waters. Overall, the data suggests that the analysis methods provide consistent size distribution results. However, because of the shear and salinity of coastal waters, resulting aggregates are too compact to estimate their D_3 values using image analysis alone.

INTRODUCTION

Coastal margins are of enormous economic, environmental, and societal value to many countries around the world. It is critically important to quantitatively describe water and ecological quality evolution and predict impact to these areas by episodic events such as accidental oil spills, contaminant release during resuspension events, algal and harmful algal blooms, etc. The traditional sampling approach would miss the environmental activity during pulsed events, but increasingly the frequency of this sampling regime is cost prohibitive. Thus, a "smart sampling" regime is needed to capture the effects of these episodes or pulses. This can be accomplished by integrating existing observation networks, new technologies, and basic research from diverse engineering and natural and social sciences disciplines. This new paradigm involves continuous, real-time in situ monitoring to provide data for development of comprehensive modeling protocols to accurately predicting ecosystem response.

Of particular environmental interest is the aggregation of colloidal crude oil droplets with suspended sediment. This situation can occur in environment when a spilled crude oil is physically or chemically dispersed in a nearshore environment with significant suspended sediment. The aggregation may affect both the transport of the

combined aggregate and fate of the crude oil. The vertical transport is altered not only

because of changes in aggregate density, but also because of reduced sediment aggregate

porosity due to the presence of the oil. Lee (2002) notes that while some studies have

linked oil-particle interaction with the physical transport of spilled oil from the sea

surface to the ocean bottom, other studies have attributed the added buoyancy

contributed by the oil in the oil-clay aggregate to longer suspension periods in the water

column.

Monitoring the geometric characteristics of aquatic particulate aggregates has

relevance to the transport of pollutant particles or pollutant associated particles. For the

past two decades, aquatic aggregates have been characterized using fractal dimensions.

Most aggregates have a non-uniform structure and the aggregate density decreases as

aggregate size increases. The geometry of such aggregates can be described using the

scaling relationship

$$N \propto l^{D_n} \tag{4.1}$$

where N is the number of the primary particles in the aggregate, D_n is the fractal

dimension determined for the aggregate in n dimensions, and l is the characteristic

length scale of the aggregate. Both fractal dimension and aggregate size impact

aggregate aggregation and vertical settling rates. For example, decreasing the fractal

dimension of an aggregate to $D_3 = 2.0$ or $D_3 = 2.5$ also increases the contact frequency of

two aggregates in water by increasing their contact sphere diameter. Considering

collisions between same sized aggregates only in a turbulent shear system, the collision

frequency of aggregates with D_3 = 2.5 or 2.0 is related to that of an aggregate with D_3 = 3.0 by the following:

$$\beta_{2.5} = \beta_{3.0} * r^{1/5} \tag{4.2a}$$

$$\beta_{2.0} = \beta_{3.0} * r^{1/2} \tag{4.2b}$$

where $\beta_{2.0}$, $\beta_{2.5}$, $\beta_{3.0}$ are turbulent shear collision frequencies for same sized aggregates of radius r and fractal dimensions of 2.0, 2.5, and 3.0, respectively. Thus for a radius of 10 μm, aggregates with a D_3 of 2.5 or 2.0 collide approximately 1.6 or 3.2 times more frequently than aggregates with D_3 of 3.0. For a sediment aggregate, decreasing D_3 generally increases its settling velocity by increasing its aggregate diameter, despite decreasing its aggregate density. However, for a sediment-oil aggregate, changes in settling velocity become more dependent on aggregate density, because of the buoyancy contribution of the oil present in the aggregate.

Experimenters have utilized a number of methods to estimate aggregate fractal dimension (Vicsek, 1992; Li and Ganczarczyk, 1989; Logan and Wilkenson, 1991; Jackson *et al.*, 1995). The following relationships can be used to determine the fractal dimensions for aggregates:

$$A \propto l^{D_2} \tag{4.3}$$

$$v \propto l^{D_3} \tag{4.4}$$

where A is the aggregate projected area, v the solid volume, and D_2 and D_3 the two- and three-dimensional fractal dimensions, respectively. The values of the fractal dimensions can be obtained from slopes of log-log plots of A or v versus the aggregate length (l).

For real time coastal monitoring, the lack of a deployable instrument for determining particle size distributions based on v precludes real-time, direct D_3 estimations. However, for short term monitoring, size distributions taken from an in-situ light scattering instrument can be integrated with distribution data from discrete sampling coupled with ex-situ aggregate analysis, i.e., electrozone particle counting or sieving. Light scattering and particle counting provides distribution data based on aggregate length and solid volume, respectively.

For coastal studies, direct imaging has been conducted using a combination of underwater cameras and image processing software (Knowles and Wells, 1998; Fennesy et al., 1994; Heffler et al., 1991). Recently, a submersible flow cytometer and imaging system (FlowCAM, Fluid Imaging Technologies, Edgecomb, Maine) has been developed which measures particles from 2-1000 µm (Sieracki et al., 1998). Designed primarily for phytoplankton analysis, this instrument has not been used for sediment aggregate analysis. However, because its image analysis program provides projected area and maximum length data for each measured aggregate, data from the FlowCAM can be used to determine aggregate D_2 values in an in-situ real time monitoring system.

Variations in mixing shear, as expected in coastal and estuarine environments, have been shown to influence suspended aggregate aggregation (Ernest et al., 1995; Lee et al., 2002) and the steady state mean aggregate lengths. Although the complexity of this relationship varies with investigators (Tambo and Francois, 1991), the formulations can be represented by the following equation:

$$d_{50} = \frac{C}{G_m^n} \tag{4.5}$$

where d_{50} is the mean stable aggregate size, C is a coefficient related to the strength

characteristics of the aggregate aggregate, G_m is the characteristic average velocity

gradient in the mixing vessel, n is a coefficient related to the particle breakup mode, the

size of eddies that cause the disruption, and the fractal dimension of the aggregate

aggregate. Thus, C and n are coefficients that depend on the water salinity and the

relative concentration and types of aqueous particles.

However, there have been limited studies detailing the effects of mixing crude oil

and suspended sediments on the resulting aggregate size or fractal dimension. Lee *et al.*

(2002) have determined size distributions of aggregates formed on crude oil droplets

stabilized by aquatic sediments. However, no attempt was made to characterize the

resulting aggregates in terms of fractal dimension. Additionally, the effects of oil

emulsification before sediment contact, as expected in chemical dispersion, have not

been examined.

Similarly, only a few studies have tested the influence of salinity on the

morphology of these aggregates. Studies by Bassin and Ichiye (1977) and Bragg and

Yang (1995) showed that saline water is required for interactions between oil and clay

sediments. Recent studies further support this contention, showing that clay-oil

aggregate formation was not significantly different from that of seawater at salinity

values as low as 1.5-0.15 (1/20 to 1/200 of oceanic water) (Lee, 2002). However, below

this salinity threshold, there was a linear decrease in the amount of oil incorporated in

the clay-oil aggregate until practically zero in distilled water. Thus, in the salinity range expected in coastal or estuarine systems, salinity may not influence oil-clay aggregate morphology.

A number of authors have used simulation methods to relate D_2 and D_3 fractal dimensions (Pao *et al.*, 1990, Nelson *et al.*, 1990). As a general rule, it has been proposed that for $D_3 < 2$, D_2 values measured from the two-dimensional projected areas concur with D_3 (Thouy and Jullien, 1994; Nelson *et al.*, 1990). Some authors disagree (Pao *et al.*, 1990) and have developed empirical relationships between D_3 and D_2 for $D_3 < 2$. However, for all D_3 values greater than 2, D_2 is equal to 2. Thus, if the clay or sediment-oil D_3 values are less than 2, an empirical relationship may validate previously obtained simulation results.

The objectives of this study are to compare the above methods for determining in-situ particle size distributions and fractal dimensions of a complex aquatic aggregate; to compare the influences of mixing shear, dispersed oil, and particle type on aggregate size and fractal dimensions; and to relate D_2 and D_3 fractal dimension measurements of sediment-oil aggregates. Particle size distributions and fractal dimension measurements were taken for the following 5 systems: latex beads, emulsified crude oil, clay, clay-oil, and silica-oil. Clay-oil aggregation was monitored at salinities of 15 and 30; the remaining systems were monitored only at a salinity of 30. The steady state volume mean aggregate size (d_{50}), aggregate standard deviation (d_σ), and aggregate fractal dimensions (D_2 and D_3) were determined for a range of mean shear rates (G_m). For spherical calibration beads and emulsified oil droplets, the FlowCAM, LISST-100, and

Coulter Multisizer yielded equivalent size measurements. Aggregate maximum diameters measured using the FlowCAM were higher than diameters measured using the LISST-100. Similarly, aggregate equivalent spherical diameters measured using the FlowCAM were higher than conserved volume equivalent diameters measured using the Coulter Multisizer. Differences in aggregate length and conserved diameters indicated significant porosity in the aggregates. Because of the compactness of the aggregates (D_3 > 2), D_2 values remained constant at 2. While salinity did not effect D_3 values, emulsified crude oil resulted in increased D_3 values. In summary, because of the shear and high salinity in coastal environments, D_3 values can not be determined through in-situ image analysis. However, the data suggests that the analysis methods provide consistent aggregate size distribution results. Thus, in-situ monitoring can be used partially to characterize aquatic particle aggregates or particle-oil aggregates.

MATERIALS AND METHODS

Particle Size Distributions

The volume mean aggregate diameter and the standard deviation were determined for each experimental condition using the following equations:

$$\bar{d}_p = \frac{\int Vol(d_p) d_p d(d_p)}{\int Vol(d_p) d(d_p)} \tag{4.6}$$

$$\sigma_{dp} = \left[\frac{\int Vol(d_p) d_p^2 d(d_p)}{\int Vol(d_p) d(d_p)} - \bar{d}_p^2 \right]^{\frac{1}{2}} \tag{4.7}$$

where d_p is the particle size bin, and $Vol(d_p)$ is the total volume within the d_p bin size.

Fractal Dimensions

Average D_3 fractal dimensions of aggregates were calculated using the particle

concentration technique (PCT) (Logan and Wilkerson, 1991). In this method, the fractal

dimension can be calculated by measuring the cumulative size distribution (N) in terms

of both actual length (l) and solid volume (V) for the same population of particles. The

volume can be converted to a length scale using $V = \pi d_s^3$, where d_s is the solid

equivalent diameter, defined as the size that the aggregate would have if it was spherical

and had no porosity. The cumulative length distribution, N(l), was obtained using

LISST-100 (Sequoia Scientific, Bellevue, WA). The LISST-100 utilizes a 5 cm laser

path length and measures angular scattering distribution obtained with a series of 32 ring

detectors to observe particles in 1.25-250 μm size range over 32 logarithmically

distributed size classes. A Coulter Counter (Multisizer and Sampling Stand II, Beckman

Coulter, Hialeah, FL) with apertures of 140 μm and 400 μm was used to measure the

solid volume distribution of the particles, resulting in a measurable size range from $2.8 \leq$

$d_s \leq 240$ μm.

Equation 4.4 relates D_3 to the solid volume and actual lengths of aggregates. The

aggregate size (l) that corresponds to the solid volume can be identified using the two

cumulative size distributions. Particle sizes can be matched when the number of

particles in one of the cumulative distributions is the same as in the other distribution or

when N(l) = N(V). A series of points are therefore matched for several different values

of the characteristic length and solid volume. Using equation 4.4, the slope of a log-log

plot of the paired values of V and l can be used to estimate the value of the fractal dimension D_3.

Using direct imaging and image analysis, D_2 values of each aggregate was calculated (Li and Ganczarczyk, 1989). The fractal geometrical properties used for determining D_2 values (equation 4.3) were obtained using a combined flow cytometer and in-situ photography/image analysis system (FlowCAM, Fluid Imaging Technologies, Edgecomb, Maine). Instrument software was used for image processing and analysis. The aggregate maximum lengths were taken as the length of the longest feret from a series of ferets measured at 32 angles (between 0 and 180°) centered on the area of aggregates. The projected area of an aggregate was calculated as the product of the area of a pixel and the number of pixels within the aggregate image. All measurements were made at 4x objective magnification with a resolution of 2 μm. For a group of aggregates, the max lengths (l) and the corresponding projected aggregate areas (A) were plotted on a logarithmic chart yielding a line with a slope equal to D_2 (equation 4.3). At least 1000 particles were measured for each sample.

Single Latex Beads Measurements

Initial measurements were conducted to compare latex bead diameters and fractal dimensions obtained using the FlowCAM imaging system, the Coulter counter, and the LISST-100 light scattering instrument. Latex particles are widely used for calibrating instruments that measure colloidal properties because of their constant size, sphericity, and initial monodispersivity. The latex particles (Coulter Electronics, Hieleah, FL) used in this work were made of a surfactant-free zwitterionic polystyrene latex. Latex

calibration beads of a given diameter (2, 5, 20, 43, 65, or 90 µm) were added to 200 mL

of electrolyte solution (Isoton, Beckman Coulter, Hialeah, FL). Each calibration bead

solution was then analyzed using the LISST-100 coupled with its small volume mixing

chamber (Sequoia Scientific, Bellevue, WA). A subsequent measurement was done

using the Coulter particle counter. For Coulter analyses, a 140 µm aperture was used for

measuring calibration beads smaller than 65 µm. For 65 and 90 µm calibration beads, a

400 µm aperture was used. Finally, each bead solution was analyzed using the

FlowCAM.

Emulsified Oil Measurements

An emulsified crude oil solution was also analyzed using these three instruments.

While this solution also contained spherical particles, it had a continuous, broad size

distribution unlike that of single latex beads. Artificially weathered Medium Arabian

crude oil (ExxonMobil, Alexandria, VA) was mixed with Corexit® 9500 (ExxonMobil,

Alexandria, VA), a hydrocarbon based chemical dispersant, at a volume ratio of 10:1.

For analysis, 0.1 mL of the dispersant-crude oil was added to 200 mL of Isoton

electrolyte solution. For measurements using the LISST-100, the small volume mixing

chamber was used to contain the diluted emulsified crude oil solution. Using a multi-

tube analysis method, 140 µm and 400 µm apertures were used for the Coulter

Multisizer, allowing droplet diameter measurements of 2.8-240 µm.

Clay Measurements

The effects of mean shear rate (5, 20, 35, 50 s^{-1}) on the steady state mean

aggregate sizes, standard deviations, and fractal dimensions of colloidal clay were

determined. Other factors such as salinity (30‰), particle loading (0.3 mg/L) and temperature (25°C) were held constant throughout the study. A 40-L PVC cylindrical reactor vessel was used for all subsequent aggregation tests. A series of sampling ports and a drain port have been fitted to the reactor. This reactor system is agitated using a stainless steel mixing impeller. The impeller is composed of four cylindrical rods evenly staggered throughout the depth of the reactor, increasing the uniformity of reactor mixing. The mixing energy transferred to the reactor fluid by impeller rotation at a given speed was determined using a torquemeter. Camp and Stein (1943) developed G_m by considering the angular distortion of an elemental volume of water due to tangential surface forces or shear stresses. G_m can be defined as:

$$G_m = \sqrt{\frac{P}{V\mu}} \tag{4.8}$$

where P is the power input by impeller, V is the tank volume, and μ is the dynamic viscosity. For $20 \leq \omega \leq 100$ rpm, the following empirical calibration resulted for this mixing system:

$$G_m = (2.85\omega - 53.4)^{\frac{1}{2}}, \quad r^2 = 0.989 \tag{4.9}$$

Time-series measurements of droplet diameter distributions were measured in-situ using a LISST-100 and ex-situ using the Coulter Multisizer and FlowCAM.

For forming clay aggregates, thirty-six liters of deionized, filtered water and a nominal amount of simulated sea salt (Instant Ocean, Aquarium Systems, Mentor, OH) were mixed in the reactor vessel and agitated for about 30 minutes at the experimental shear rate. The reactor salinity was verified using a refractometer. Bentonite clay

(Fisher Chemical, Hanover Park, IL) was used as model aquatic suspended particulate matter (SPM). Clay was added to water of the same salinity, creating a 100 mL slurry solution. The particle slurry was sonicated for 15 minutes to break preexisting aggregates. The slurry was then added to the mixing vessel and rapid mixed for 1 minute before beginning to collect size distribution data. The impeller motor was started at the proper rpm to achieve a nominal G_m and the aggregation process was monitored for 4 hours. Aggregate size distributions were measured every 5 seconds using the LISST-100, while samples for the remaining instruments were taken every 30 minutes.

Clay-Oil Measurements

The effects of mean shear rate (5, 20, 35, 50 s^{-1}) and salinity (15, 30 ‰) on the steady state mean aggregate sizes, standard deviations, and fractal dimensions of colloidal clay-emulsified crude oil aggregates were determined. Oil loading (1.0 mg/L), clay loading (0.3 mg/L), and temperature (25°C) were held constant throughout the study. Characterizations of clay-oil aggregates were conducted as the clay aggregate diameter measurements. After mixing the clay slurry, 0.5 mL amount of crude oil and Corexit® 9500 at a 10:1 ratio was added to 100 mL of saline water and sonicated for 10 minutes. The clay and oil slurries were then added to the mixing vessel and rapid mixed for 1 minute before beginning to collect size distribution data. The impeller motor was started at the proper rpm to achieve a nominal G_m and the aggregation process was observed for 4 hours.

Silica-Oil Measurements

The effects of mean shear rate (5, 20, 35, 50 s^{-1}) on the steady state mean aggregate sizes, standard deviations, and fractal dimensions of colloidal silica (Fisher Chemical)-emulsified crude oil aggregates were determined. Oil loading (1.0 mg/L), salinity (30 ‰), silica loading (0.3 mg/L), and temperature (25°C) were held constant throughout the study. Reactor addition and subsequent characterizations of silica-oil aggregates were conducted as the clay-oil aggregate diameter measurements.

Data Correlation

To determine an empirical relationship, corresponding values of D_2 and D_3 determined from each experiment were plotted. A linear least squares fitting routine (Excel 5.0) was used to determine a best fit line and quality of fit parameters. At least 3 measurements were taken for each experimental condition.

RESULTS

Single Latex Beads Measurements

Initial measurements were conducted using latex beads and emulsified crude oil. These particles were approximately spherical, the ideal geometry for comparing particle diameter results from the selected suite of instruments. Additionally, the fractal dimensions for spherical particles are known ($D_2 = 2.0$ and $D_3 = 3.0$). Figures 4.1a and 4.1b compare the measured diameters of latex calibration beads. Error bars at each point represent the measured standard deviation about the mean diameter for each bead size. Between the instruments, mean diameter values are nearly identical. Standard deviations measured by the LISST-100 are larger than those measured by the FlowCAM at 65 and
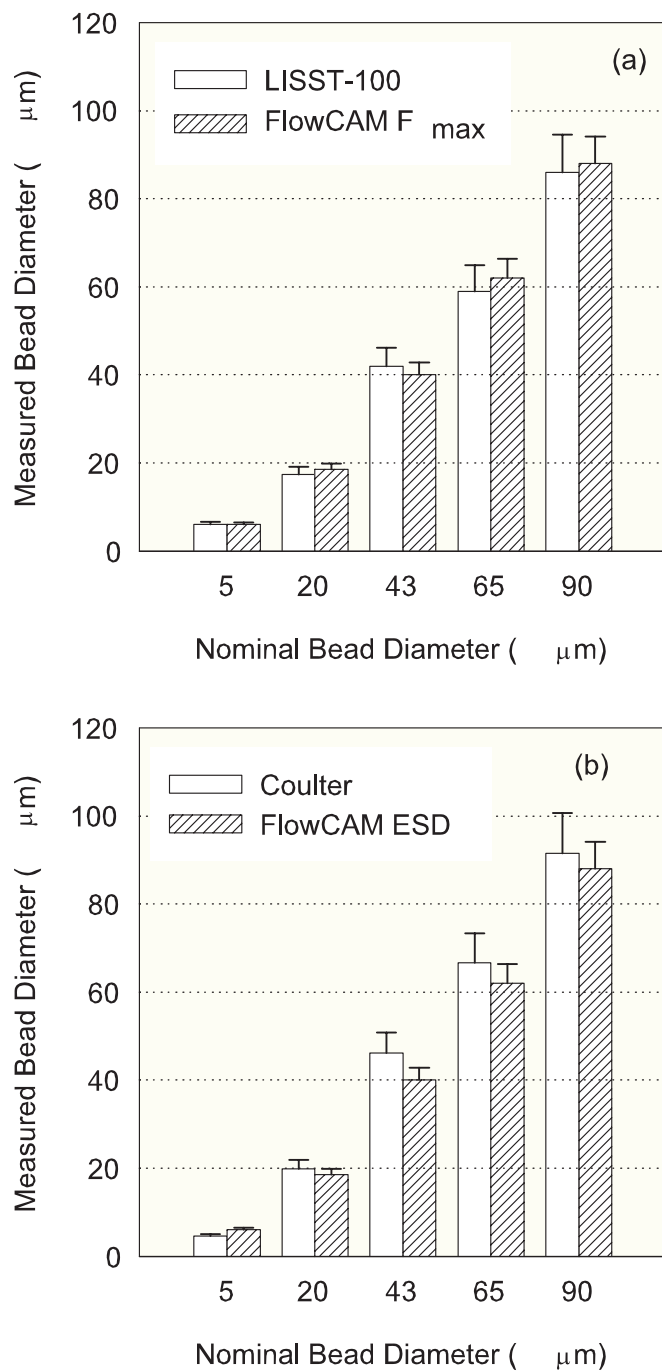
Figure 4.1. Comparison of aggregate dimensions as measured by particle size instruments. Aggregate diameters were determined from (a) projection measurements and (b) conserved volume/area measurements

90 µm. This increase is due to wider size bins at this size range. Consequently, false readings in adjacent bins result in increased standard deviation values. Nevertheless, the coefficient of variation (C.V.) remains less than 10% for each measured diameter.

The measured particle diameters in Figures 4.1a and 4.1b were plotted logarithmically to derive D_2 and D_3 values (equations 4.3 and 4.4). A plot of $d_{50,Fmax}$ vs. $d_{50,ESD}$ resulted in $D_2 = 1.96 \pm 0.12$. A logarithmic plot of $d_{50, L}$ vs. $d_{50,C}$ resulted in $D_3 = 2.94 \pm 0.12$ ($r^2 = 0.994$). The D_2 and D_3 values are near theoretical circular and spherical values because the $d_{50,Fmax}$, $d_{50,ESD}$, $d_{50, L}$ and $d_{50,C}$ values are virtually identical. This is the expected result for a spherical particle in a Euclidean geometry.

Emulsified Oil Measurements

An emulsified crude oil was analyzed to characterize a broader continuous size distribution. Using the LISST-100, the mean diameter ($d_{50,L}$) and standard deviation ($d_{\sigma,L}$) values are 24.9 ± 2.3 µm and 26.9 ± 3.2 µm, respectively. The maximum Feret diameters determined by the FlowCAM yielded similar values to the LISST-100 ($d_{50,Fmax} = 26.4 \pm 2.2$ µm and $d_{\sigma,Fmax} = 21.3 \pm 2.3$ µm). Using the Coulter Multisizer, the mean diameter ($d_{50,C}$) and standard deviation ($d_{\sigma,C}$) values are 28.5 ± 0.3 µm and 19.4 ± 0.5 µm, respectively. The equivalent spherical diameters measured by the FlowCAM yielded comparable values to the Coulter Multisizer ($d_{50,ESD} = 27.3 \pm 0.7$ µm and $d_{\sigma,ESD} = 16.3 \pm 0.3$ µm). As with the latex beads, the measured fractal dimensions of the emulsified oil were near theoretical values with $D_2 = 1.94 \pm 0.13$ and $D_3 = 2.91 \pm 0.18$.

The above data demonstrate consistent diameter measurements for spherical particles. This result supports the validity of each measurement technique by verifying

the properties of geometrically simple samples. However, in natural aquatic systems, aquatic particles are generally characterized as aggregates described using fractal geometry. Thus, the remaining experiments characterize clay aggregate and SPM-oil aggregate diameters and fractal dimensions. Crude oil was chosen as a typical anthropogenic contaminant that may be "sensed" using a continuous coastal monitoring system.

Clay Measurements

These experiments were conducted to determine the effects of mean shear rate (G_m) and particle type on the aggregate diameter distributions and fractal dimensions. Unlike calibration beads or emulsified oil, sediment aggregates are not expected to be spherical ($D_3<3.0$). Table 4.1 lists the mean volume aggregate diameters and standard deviations as measured by the LISST-100, Coulter Multisizer, and FlowCAM. For the FlowCAM, diameter measurements are presented as maximum Feret diameters and equivalent spherical diameters. The experiments are grouped according the experimental treatments (sediment type: C = clay, S = silica; oil concentration: O = oil (1mg/L), NO = no oil added; salinity level: S15 = salinity 15, S30 = salinity 30). As G_m values increase (C_NO_S30), the aggregate length as measured by all instruments decreases. In addition, the standard deviations of the projected aggregate distributions in this group (C_NO_S30) decrease with increased shear rate. This result suggests that either aggregate breakage or restructuring occurs with increased G_m. Increasing values of D_3

Table 4.1. Experimentally measured sediment and sediment-oil aggregate lengths

Group #	SPM Type	Oil (mg/L)	S (‰)	G(s⁻¹)	Maximum Diameter				Conserved Diameter			
					LISST-100		FlowCAM		Coulter		FlowCAM	
					$d_{50,L}$ (μm)	$d_{\sigma,L}$ (μm)	d_{50,F_max} (μm)	d_{σ,F_max} (μm)	$d_{50,C}$ (μm)	$d_{\sigma,C}$ (μm)	$d_{50,ESD}$ (μm)	$d_{\sigma,ESD}$ (μm)
C_NO_S30	Clay	0.0	15	5	77.8	39.2	91.0	45.9	15.4	7.57	21.1	10.4
				20	60.9	27.2	69.4	31.0	15.8	4.7	21.2	6.3
				35	46.2	24.5	53.1	28.2	16.9	9.0	22.8	12.2
				50	36.4	22.1	40.8	24.8	15.8	6.1	20.9	8.1
C_O_S30	Clay	1.0	15	5	89.7	44.0	107.6	52.8	20.8	20.4	29.1	28.6
				20	56.6	29.6	64.5	33.7	21.6	17.8	28.9	23.9
				35	37.4	27.7	43.4	32.1	20.3	13.0	27.6	17.7
				50	34.4	27.1	40.2	31.7	32.8	30.3	44.9	41.5
C_O_S15	Clay	1.0	30	5	109.1	30.0	129.8	35.7	26.7	20.4	37.1	28.4
				20	57.7	24.5	65.2	27.7	30.5	24.4	40.6	32.5
				35	47.1	27.3	52.8	30.6	28.7	20.3	37.9	26.8
				50	38.3	28.5	43.3	32.2	29.5	22.5	39.2	29.9
S_O_S30	Silica	1.0	15	5	73.2	28.2	84.2	32.4	16.9	6.7	22.8	9.0
				20	46.2	24.1	54.1	28.2	17.3	6.2	23.7	8.5
				35	31.8	28.0	35.9	31.6	23.3	18.4	31.0	24.5
				50	25.9	17.7	28.7	19.6	18.4	7.2	24.1	9.4

Figure 4.2. Influence of mean shear rate (G_m) on (a) two-dimensional (D_2) and (b) three-dimensional (D_3) clay and clay-oil aggregate fractal dimensions

with increased G_m supports the hypothesis of aggregate restructuring (Figure 4.2). D_2 values remained at approximately 2 because of the relative compactness of the aggregates ($D_3 > 2$) (Figure 4.2).

Clay-Oil Measurements

Experiments (C_O_S30) were conducted to determine the effects of shear rate and emulsified oil on the aggregate diameter distributions and fractal dimensions. Comparing data from experimental groups C_NO_S30 and C_O_S30 presents the effect of emulsified oil on aggregate diameter and fractal dimension. As G_m increases (C_O_S30), the projected aggregate lengths and standard deviations decrease as with group C_NO_S30. However, the n value for clay aggregates (0.31 ± 0.05) and clay-oil aggregates (0.43 ± 0.08) are significantly different. Solid aggregate diameters and standard deviations, as measured by the Coulter Multisizer or FlowCAM equivalent spherical diameter, are constant with G_m. However, the clay-oil solid aggregate diameter is significantly higher than that of the clay solid aggregate diameter. Calculated fractal dimension data (Figure 4.2) shows that higher G_m values result in increased fractal dimensions. However, the fractal dimensions of clay-oil aggregates increase faster than that of clay aggregates. At $G_m = 50 \text{ s}^{-1}$, the clay-oil aggregates are approximately spherical ($D_3 = 2.96$).

A second set of clay-oil aggregation experiments (C_O_S15) was conducted to determine the effects of shear rate and salinity on the clay-oil aggregate diameter distributions and fractal dimensions. Comparing data from C_O_S15 and C_O_S30 highlights the influence of salinity on aggregate diameter and fractal dimension. As G_m

increases, the projected aggregate lengths and standard deviations in C_O_S15 decrease

(Table 4.1). The n value at 15 ‰ (0.45±0.06) was not significantly different than that at

30 ‰ (0.43±0.08). Solid aggregate diameters and standard deviations, as measured by

the Coulter Multisizer or FlowCAM equivalent spherical diameter, are constant with G_m.

However, the mean clay-oil solid aggregate diameter is significantly higher at 15 ‰ than

at 30 ‰ (Table 4.1). Calculated fractal dimension data (Figure 4.3) shows that higher G_m

values result in increased fractal dimensions. However, the fractal dimensions of clay-

oil aggregates increase similarly at both 15 ‰ and 30 ‰. At $G_m = 50$ s^{-1}, the clay-oil

aggregates are approximately spherical at salinities of 15 ($D_3 = 2.96$) and 30 ($D_3 =$

2.78).

Silica-Oil Measurements

A set of silica-crude oil experiments (S_O_S30) was conducted to determine the

effects of shear rate and emulsified oil on the aggregate diameter distributions and fractal

dimensions on silica-oil aggregates. As with other aggregates, higher G_m values result in

smaller aggregate lengths and increased D_3 values (Figure 4.4). Data from experimental

groups C_O_S30 and S_O_S30 allow the comparison of sediment type on the sediment-

oil aggregate size and dimension.   Calculated fractal dimension data suggests that

restructuring is occurring (Figure 4.4). At increasing G_m values, silica-oil aggregates

similar fractal dimensions to that of clay-oil aggregates. Also, the empirically

determined n value for silica-oil aggregates (0.44±0.12) is similar to that of clay-oil
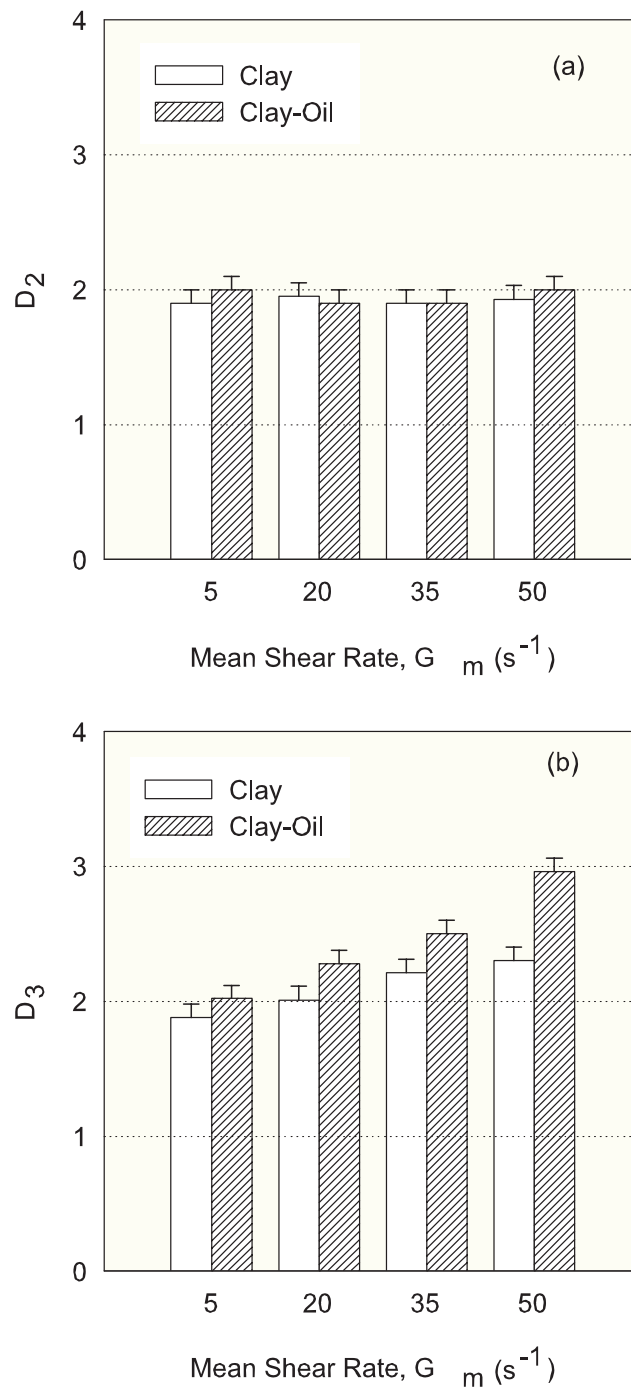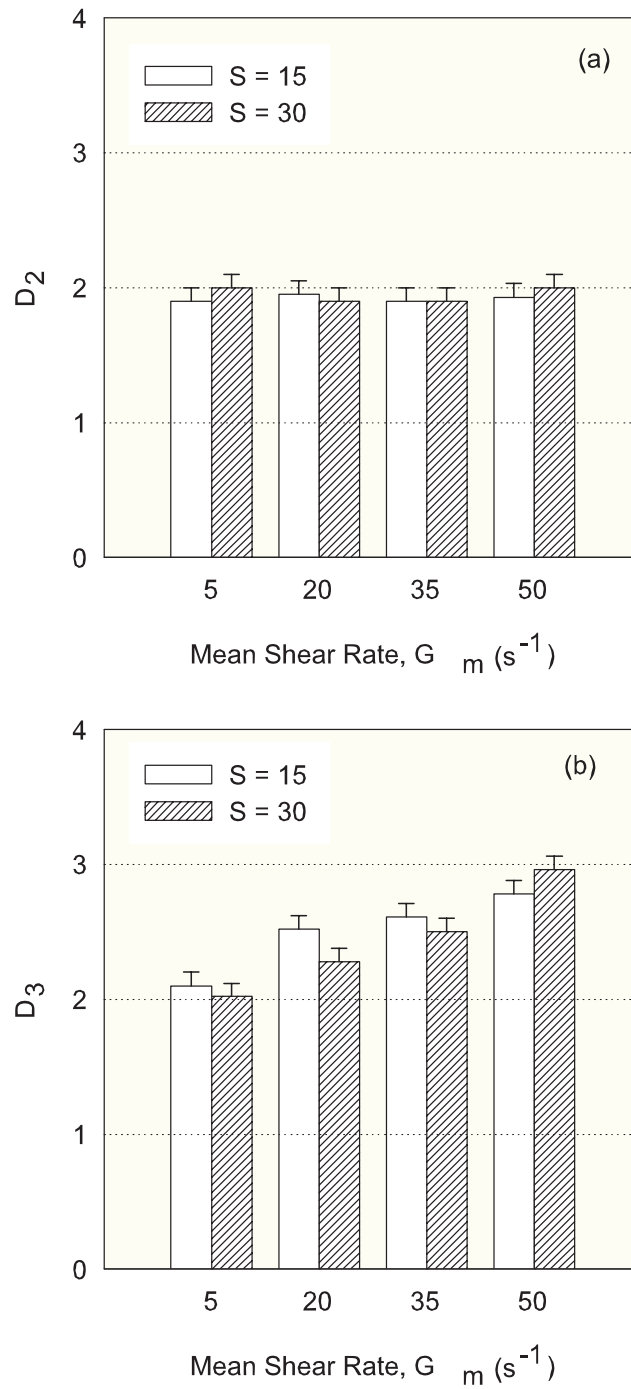
Figure 4.3. Influence of mean shear rate (G_m) and salinity on (a) two-dimensional (D_2) and (b) three-dimensional (D_3) clay-oil aggregate fractal dimensions
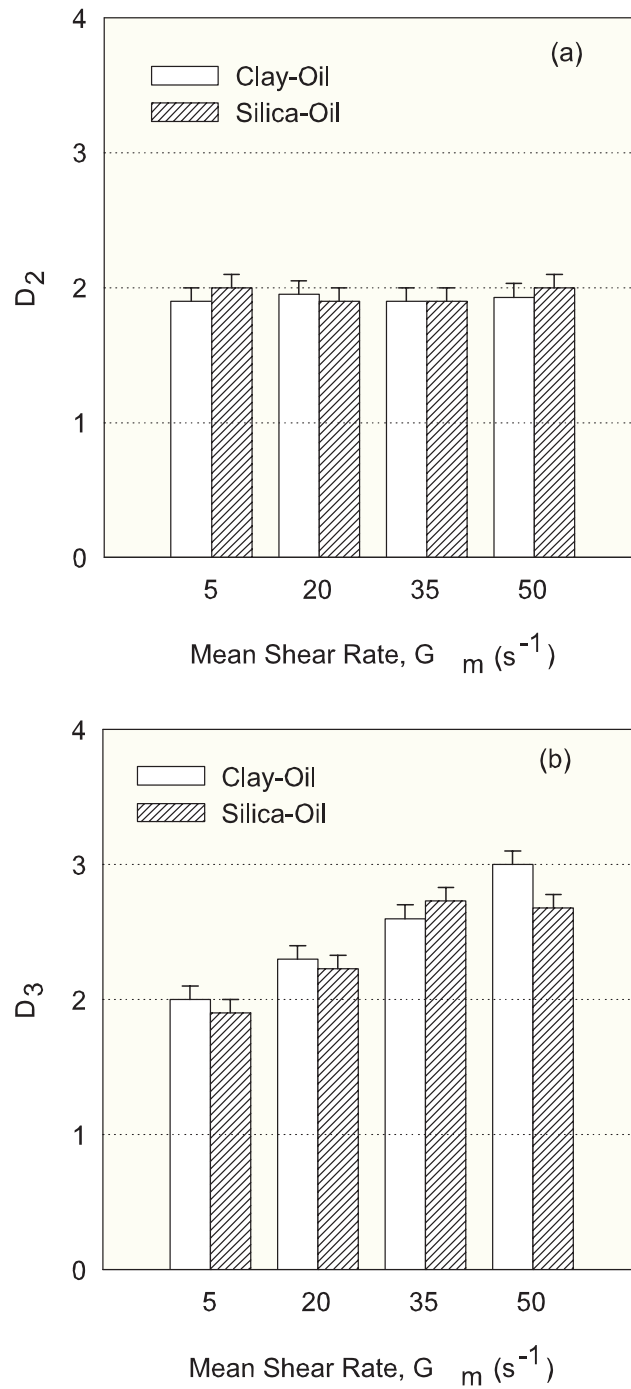
Figure 4.4. Influence of mean shear rate (G_m) and sediment type on (a) two-dimensional (D_2) and (b) three-dimensional (D_3) sediment-oil aggregate fractal dimensions

aggregates (0.43 ± 0.08). These facts suggest that silica and clay particles form similar aggregates with emulsified crude oil.

Data Correlation

Because of the suitability of the submersible FlowCAM for aggregate size measurements, a relationship between D_2 and D_3 was determined empirically. However, as the D_3 values for the studied aggregates ranged from 2-3, D_2 values were approximately 2. Thus, because of the restricted D_3 values obtained, a non-trivial correlation between D_2 and D_3 could not be obtained. As a result, the FlowCAM can not be used to determine D_3 values for sediment or sediment-oil aggregates in coastal environments.

DISCUSSION

Estuarine and coastal water bodies demonstrate variability in salinity and mixing shear due to fluctuations in wind and current influences. Because of their proximity to the shoreline, these water bodies also have significant levels of SPM. This experimental data shows that hydrodynamics significantly impact the morphology of suspended sediment. Differences in the influence of shear on the restructuring of clay-oil and clay aggregates suggest that differences in surface energy are the primary reason. At 20°C, tetradecane (a model oil) and bentonite clay have surface energies of 22.3 and 55.5 mJ/m^2, respectively (Van Oss, 1994). Through the Dupré equation, the energy expended in separating two particles is related their interfacial energies (Israelachvili, 1992). Thus, by thermodynamic reasoning, more work is required to restructure clay aggregates than clay-oil aggregates, a conclusion also reached through empirical analysis.

Another noteworthy result is that changes in salinity did not result in changes in the morphology of the clay-oil aggregates. Because of the relatively high salinity of coastal and ocean waters, electrostatic resistance to aggregation is virtually nonexistent. Conversely, in fresh water environments (salinity < 1‰), salinity variations are likely to be more significant (Lee, 2002). However, testing at such low salinities was outside the scope of this study.

This research focuses on the steady state morphology of clay-oil aggregates under different hydrodynamic and salinity conditions. Another relevant line of questions regards the kinetics of these aggregate formations. Currently, a modeling effort is underway to incorporate these aggregate formations in an existing sediment transport model (Lee *et al.*, 2002; 2000; Garton *et al.*, 1996; Ernest *et al.*, 1995). This model is required in order to predict the fate of spilled oil in a coastal or estuarine environment.

Implications for coastal monitoring also result from this study. The experimental data suggests that each of these instruments accurately characterize size distributions for spherical particles. However, in order to meet the goal of continuous monitoring, the particle size instrument must be field deployable. Light scattering instruments such as the LISST-100 have been utilized in a number of field deployments for sediment characterization (Fugate and Friedrichs, 2002; Gartner *et al.*, 2001). The FlowCAM has also been used in field deployments for algae characterization (Sieracki and Sieracki, 1999). To the authors knowledge, there are no commercial field deployable particle characterization instruments using electrozone principles.

For actual coastal systems, distinguishing between different types of aquatic particles may be important. The FlowCAM provides the advantage of particle discrimination based on optical properties such as particle fluorescence or color. Because the FlowCAM images each particle, a scientist can "train" the instrument to examine only particles of interest. For example, the instrument can distinguish between a fluorescing algal cell or oil droplet and a non fluorescing sediment particle. Similarly, it can be "trained" to differentiate between harmful red tide algae cells versus typical algae cells. In contrast, the LISST-100 yields size distribution data for all particles present without discrimination regarding particle type. This nondiscrimination can be mitigated somewhat by coupling the LISST-100 with a flourometer. Increases in fluorescing particles measured by the flourometer can be used as a digital actuator for the LISST-100, causing it to measure the size distribution of those particles. If there are other particles present, however, their size data will also be captured in the distribution.

An additional complexity of actual coastal systems is the presence of particle aggregates. These aggregates generally are not spherical and can be described instead using fractal geometry. The FlowCAM can be field deployed and directly yields two-dimensional aggregate fractal dimensions. However, there is not a general theoretical relationship between two and three-dimensional fractal dimensions. Alternatively, a deployed LISST-100 continuously yields aggregate length data. However, grab samples would be required to determine conserved volume distribution data needed to estimate three-dimensional fractal dimensions directly. This requirement would constrain the advantages of continuous deployed coastal monitoring for highly flocculent particles.

CONCLUSIONS

The experimental work demonstrated the validity of using data from the FlowCAM or integrated data from the LISST-100 and Multisizer for determining aggregate size distributions. For spherical particles, measured mean particle sizes and standard deviations were nearly identical regardless of the instrument used. For sediment aggregates, FlowCAM maximum feret diameters and equivalent spherical diameters were larger than diameters measured by the LISST-100 and Coulter Multisizer, respectively. Some of this bias likely results from differences in the aggregate orientation caused by the instruments as the aggregates are measured.

In all experimental groups, the aggregate length decreased with increased mean shear rate, resulting in a higher aggregate fractal dimension. Differences in empirical parameter *n* for clay and sediment-oil particles suggest that particle surface chemistry may be a factor in aggregate restructuring.

The presence of emulsified oil resulted in larger clay aggregate fractal dimensions at all tested mean shear rates. Changes in salinity did not result in significant differences in clay-aggregate fractal dimensions.

Because of the limited range of D_3 values resulting from aggregates formed in shear environment, no significant correlation between measured two-and three-dimensional fractal dimensions could be determined.

CHAPTER V

DETERMINATION OF COLLISION EFFICIENCIES FOR FLOCCULENT

PARTICLE TRANSPORT MODELS: HETEROGENEOUS DENSITY SYSTEMS

OVERVIEW

This chapter describes a modeling approach that simulates changes in particle size distribution and density due to aggregation by extending the Smoluchowski aggregation kinetic model to particles of different density. Batch flocculation studies were conducted from clay, colloidal silica, crude oil, clay-crude oil, and silica-crude oil systems. A parameter estimation algorithm was used to estimate homogeneous collision efficiencies (α_{HOMO}) for single particle type systems and heterogeneous collision efficiencies (α_{HET}) for two particle type systems. Homogeneous collision efficiency values (α_{HOMO}) were greater for clay (0.7) and for crude oil (0.3) than for silica (0.01). Thus, clay and crude oil were classified as cohesive particles while silica was classified as noncohesive. Heterogeneous collision efficiencies were similar for clay-oil (0.4) and silica-oil (0.3) systems. Thus, crude oil increases the aggregation of noncohesive particles. Apparent first order flocculation rates were determined for oil, clay and silica using laboratory data. Apparent second order flocculation rates for oil and clay in oil-clay systems and for oil and silica in oil-silica systems were estimated using simulation data. In single particle type systems, aggregation Damköhler numbers for clay and oil ranged from 0.1-1.0. This result suggests that clay flocculation and oil coalescence may occur on the same timescales as clay sedimentation and oil resurfacing, respectively.

For clay and oil in clay-oil systems, aggregation Damköhler numbers ranged from 0.1-1.0. These results suggest that clay-oil aggregation may occur on the same timescale as sedimentation.

INTRODUCTION

Discrete settling and particle-particle interactions are significant mechanisms in the transport of particulate material (Morel and Schiff, 1980; Hunt and Pandya, 1984). In the simplest case, in which the suspension is stable with respect to the hydrodynamic and particulate surface conditions, the system may be treated as noninteractive, thereby eliminating particle interaction terms. Under these conditions, a simple advective-dispersive transport model may be used to represent the system. However, for unstable conditions, in which particle agglomeration and breakup are possible, description of the system becomes more complex. In this case, heterogeneous particle interaction terms must also be included (Bonner *et al.*, 1994). The particle interaction terms of consequence result from collisions due to Brownian motion, fluid shear, and differential settling (Hunt and Pandya, 1984, Gibbs and Hopkins, 1984). For particles larger than 1µm in diameter, fluid shear and differential settling are dominant collision mechanisms (Friedlander, 1977; Lawler, 1979).

Ernest *et al.* (1995) presented an aggregation and settling model for multiple-sized sediment particles. The work presented herein extends this model to aquatic particles of multiple densities. Suspended sediment particles carry a number of highly toxic and persistent contaminants through an aquatic system. To assess the impact of the contaminants that are associated with the sediment on the water quality and the benthic

organisms in the aquatic environment, a better understanding of the transport processes of the suspended particles is needed. For example, for cohesive sediments, particle aggregation can significantly influence the observed resuspension and deposition rates (Garton *et al.*, 1996). The resuspension of deposited sediment affects both the water quality and organisms that thrive in the water column.

Because of the high volume of crude oil brought into ports along the Gulf of Mexico and because of significant releases of oil from natural seeps (MacDonald *et al.*, 2002; MacDonald *et al.*, 1993), an environmentally interesting phenomena is the aggregation of colloidal crude oil droplets with suspended sediment. This situation can occur in environment when a crude oil is physically or chemically dispersed in a nearshore environment with suspended sediment. The aggregation may affect both the transport of the combined aggregate and fate of the crude oil (Page *et al.*, 2000b; Le Floch *et al.*, 2002; Page *et al.*, 2003; Bassin and Ichiye, 1977; Lee *et al.*, 2002). The vertical transport is altered not only because of changes in aggregate density, but also because of reduced aggregate porosity due to the presence of the oil. Lee (2002) notes that while some studies have linked oil-particle interaction with the physical transport of oil from the sea surface to the ocean bottom, other studies have attributed the added buoyancy contributed by the oil in the oil-clay aggregate to longer suspension periods in the water column.

This chapter presents the application of an aggregation model to a system of suspended sediment and emulsified droplets. An expression relating homogeneous (α_{HOMO}) and heterogeneous (α_{HET}) collision efficiency values to the observed collision

efficiency (α_{OBS}) was developed using a probabilistic approach. Values of α_{HOMO} were determined experimentally for crude oil droplets, clay aggregates, and silica particles at different mean shear rates (G_m). Values of α_{HET} were determined experimentally for crude oil-clay and crude oil-silica particle systems at G_m values and oil-sediment ratios. Apparent first order flocculation rates (K') for oil, clay and silica were determined using laboratory data. Apparent second order removal rates (K'') for free oil in oil-clay systems and in oil-silica systems were estimated using simulation data.

METHODS

Modeling Background

Since coagulation affects the distribution of particle settling rates, one must consider coagulation and settling simultaneously to describe sedimentation kinetics. For a settling column, the dynamic equation for the particle size distribution is described by the following:

$$\frac{dn_{k,q}}{dt} = D_z \frac{\partial^2 n_{k,q}}{\partial z^2} - w_{k,q} \frac{\partial n_{k,q}}{\partial z} + \theta_{k,q} \qquad (5.1)$$

where $n_{k,q}$ is the particle size distribution, given as the number concentration of particles (number cm^{-3}) as a function of particle volume k (cm^3)and effective density q (g cm^{-3}), z is the vertical distance from the top of the water column (cm), D_z is the vertical dispersion coefficient (cm^2 s^{-1}), $w_{k,q}$ is the settling velocity (cm s^{-1}) of particle volume k and effective density q, and $\theta_{k,q}$ is the interaction term (number cm^{-3} s^{-1}) due to coagulation.

In a system of particles (flocs) composed of primary particles of two densities (ρ_{p1} and ρ_{p2}), particles (flocs) of densities o and p (ρ_o and ρ_p) can be calculated using the following:

$$\rho_o = (1 - e_o)(x_{1,o}\rho_{p1} + x_{2,o}\rho_{p2}) + e_o\rho_{H_2O} \tag{5.2a}$$

$$\rho_p = (1 - e_p)(x_{1,p}\rho_{p1} + x_{2,p}\rho_{p2}) + e_p\rho_{H_2O} \tag{5.2b}$$

where e_o is the porosity of particle of density o, e_p is the porosity of particle of density p, ρ_{H2O} is the water density, $x_{1,o}$ is the volume fraction of ρ_{p1} in particle of density o (v_{p1}/v_o), $x_{1,o}$ is the volume fraction of ρ_{p1} in particle of density o (v_{p2}/v_o), $x_{1,o}$ is the volume fraction of ρ_{p1} in particle of density p (v_{p1}/v_p), and $x_{1,p}$ is the volume fraction of ρ_{p1} in particle of density p (v_{p2}/v_p). The effective particle density (q) (floc density) can be calculated using the following:

$$\rho_q(o, p) = (x_o\rho_o + x_p\rho_p) \tag{5.3}$$

where x_o and x_p are the volume fractions of particle types o ($= v_o/v_q$) and p ($= v_p/v_q$), respectively. In this analysis, aggregate density is assumed constant with size, i.e., no increase in floc porosity due to increased aggregate size. The settling velocity is assumed to follow Stokes law; therefore

$$w_{k,q} = \frac{(\rho_q - \rho_{H_2O})l_k^2 g}{18\mu} \tag{5.4}$$

where μ is the fluid viscosity (g cm^{-1} s^{-1}), l_k is the effective spherical diameter (cm) and g is the gravitational constant (981.0 cm^2 s^{-1}).

The interaction term, $\theta_{k,q}$, represents the particle contact mechanisms of Brownian motion, fluid shear, and differential sedimentation. It is represented by the following relationship:

$$\theta_{k,q} = \frac{dn_{k,q}}{dt} = \frac{1}{2} \sum_{M_{i,i}+M_{j,p}=M_{k,q}} \alpha_{obs}(o,p)\beta(i,j,o,p)n_{i,o}n_{j,p}$$
$$-n_{k,q} \sum_{o=1}^{c_{density}} \sum_{i=1}^{c_{size}} \alpha_{obs}(o,q)\beta(i,k,o,q)n_{i,o} \tag{5.5}$$

where i, j, and k denote volume categories; o, p, and q denote effective density categories; $c_{density}$ and c_{size} are the maximum number of density and volume categories; $n_{i,o}$, $n_{j,p}$, and $n_{k,q}$ are the number concentration of particle volumes i, j, and k and of effective particle densities o, p, and q; $\alpha_{obs}(o,p)$ is the observed collision efficiency function (i.e., number of effective collisions/number of total collisions), which depends on the interparticle surface forces; and $\beta(i,j)$ is the collision frequency function, which depends on the mode of interparticle contact. Equation 5.5 is a system of discrete, nonlinear differential equations. The first term on the right-hand side of equation 5.5 sums the rate of formation of particles of k-volume and q-density classes from all collisions of particles smaller than the k-volume particles. The summation is over all volume classes i and j and all density classes o and p such that the mass of the sum of the i-volume, o-density particle and of the j-volume, p-density particle equals the mass of the k-volume, q-density particle:

$$M_{k,q} = M_{i,o} + M_{j,p} \tag{5.6}$$

In the particle conjunction represented by equation 5.6, mass is conserved. The second set of summation terms reflects the loss of k-volume and q-density aggregates as they combine with all other aggregate sizes to form larger aggregates.

The observed interaction frequency ($\beta_{obs,ijop}$) is given by the sum of the individual collision frequencies:

$$\beta_{obs,ijop} = \beta_{Br,ij} + \beta_{sh,ij} + \beta_{ds,ijop}$$

$$\beta_{Br,ij} = \frac{2kT}{3\mu}\left(\frac{1}{l_i} + \frac{1}{l_j}\right)(l_i + l_j)$$

$$\beta_{sh,ij} = \frac{G_m}{6}(l_i + l_j)^3$$

$$\beta_{ds,ijop} = \frac{\pi}{4}(l_i + l_j)^2(w_{i,o} - w_{j,p})$$

(5.7)

where $\beta_{Br,ij}$ is the collision efficiency due to Brownian motion, $\beta_{sh,ij}$ is the collision efficiency due to fluid shear, and $\beta_{ds,ij}$ is the collision efficiency due to differential sedimentation. Specific functions for each of these collision frequencies are as presented previously (Bonner *et al.*, 1994; Ernest *et al.*, 1995; Lee *et al.*, 2000).

The observed collision efficiency, α_{obs}, is operationally defined as the ratio of the actual number of "successful" aggregations to the number predicted in "unhindered" conditions. This parameter describes the effects of the electrostatic energy barrier in reducing "successful" collisions. In previous studies of single particle type systems (Ernest *et al.*, 1995; Lee *et al.*, 2000), collision efficiency values for a given particle type were assumed constant with size. In systems of two particle types, aggregates are composed of both particle types. Between composite aggregates, observed collision efficiency is defined by the sum of probabilities of successful surface interactions, i.e.,

$$\alpha_{obs}(o,p)=\alpha_{HOMO,1}\left(sf_{1,o}\right)\left(sf_{1,p}\right)+\alpha_{HOMO,2}\left(sf_{2,o}\right)\left(sf_{2,p}\right)+\alpha_{HET,1-2}\left(sf_{1,o}sf_{2,p}+sf_{1,p}sf_{2,o}\right) \tag{5.8}$$

where $sf_{1,o}$, $sf_{2,o}$, $sf_{1,p}$ and $sf_{2,p}$ are surface fractions of constituent particles 1 and 2 in

aggregate with density o and constituent particles 1 and 2 in aggregate with density p,

respectively. The coefficients $\alpha_{HOMO,1}$, $\alpha_{HOMO,2}$, α_{HET} are probabilities of successful

aggregation through contacts of floc constituent types 1-1, 2-2, and 1-2, respectively.

Equation 5.8 can also be viewed as a weighted average of aggregation probabilities

based on the fraction of constituent particles in each pair of aggregating flocs. Assuming

that the surface fraction of particle constituents is proportional to their volume fraction,

equation 5.8 can be written as the following:

$$\alpha_{obs}(o,p)=\alpha_{HOMO,1}\left(x_{1,o}\right)\left(x_{1,p}\right)+\alpha_{HOMO,2}\left(x_{2,o}\right)\left(x_{2,p}\right)+\alpha_{HET}\left(x_{1,o}x_{2,p}+x_{1,p}x_{2,o}\right) \tag{5.9}$$

where $x_{1,o}$, $x_{2,o}$, $x_{1,p}$ and $x_{2,p}$ are volume fractions of constituent particles 1 and 2 in

aggregate with density o and constituent particles 1 and 2 in aggregate with density p,

respectively. The volume fractions of constituent particle 1 and particle 2 in an

aggregate with density o is calculated by the following:

$$x_{1,o}=\frac{\rho_o-\rho_2}{\rho_1-\rho_2} \tag{5.10a}$$

$$x_{1,p}=1-x_{1,o} \tag{5.10b}$$

In this description of aggregation, the following assumptions have been made:

(1) only binary collisions of particles are considered; (2) particle breakup is neglected;

(3) particles before and after each aggregation are spherical; (4) particles approach one

another on rectilinear paths, the path of one particle not being affected by the presence of

another; (5) collision functions for Brownian motion, fluid shear, and differential settling

are additive; (6) the floc density does not vary with aggregate size, and (7) α_{HOMO} and α_{HET} are constant with particle size.

Summary of Experimental Methods

To estimate homogeneous and heterogeneous collision efficiency values, a series of batch mixing experiments were conducted. Detailed descriptions of reagents, experimental apparatus have been presented in chapter four. In the experiments, a 40-L batch mixing tank was used to measure changes in particle size distribution (PSD) under different experimental conditions. In the experiments, PSD was measured in-situ using a light scattering particle size analyzer (LISST-100, Sequoia Instruments, Bellevue, WA), and ex-situ using an electronic particle counter (Sampling Stand II and Multisizer, Coulter Electronics Limited, Hialeah, FL). Using this tank and artificial seawater, a series of experiments was performed to measure changes in PSD of bentonite clay, colloidal silica, chemically dispersed crude oil, clay-crude oil, and silica-crude oil systems. An initial set of experiments (Table 5.1) was conducted to determine the effects of particle type (crude oil, clay, or silica) and mean shear rate (G_m) on homogeneous collision efficiency (α_{HOMO}) and apparent first order collision rate (K'). A second set of experiments (Table 5.2) was conducted to determine the effects of sediment type (silica, clay) and G_m on heterogeneous collision efficiency (α_{HET}) and apparent second order collision rates (K'') of silica or clay and crude oil in a sediment-crude oil system. The third set of experiments (Table 5.2) was conducted to determine

Table 5.1. Experimental design for estimating homogeneous collision efficiency

Experiment Name	Mean Shear Rate (G_m, s^{-1})	Particle Type	Particle Loading (mg/L)	Particle Loading (μL/L)	K' (s^{-1})	α_{HOMO}
G05_Oil12	5.0	Oil	12.5	14.0	1.25E-04	0.25
G20_Oil12	20.0	Oil	12.5	14.0	5.17E-04	0.22
G35_Oil12	35.0	Oil	12.5	14.0	9.63E-04	0.28
G50_Oil12	50.0	Oil	12.5	14.0	1.25E-03	0.24
G05_Cl08	5.0	Clay	8.3	4.9	1.82E-04	0.77
G20_Cl08	20.0	Clay	8.3	4.9	8.25E-04	0.78
G35_Cl08	35.0	Clay	8.3	4.9	1.21E-03	0.77
G50_Cl08	50.0	Clay	8.3	4.9	1.60E-03	0.76
G05_Si08	5.0	Silica	8.3	3.5	8.33E-06	0.01
G20_Si08	20.0	Silica	8.3	3.5	2.83E-05	0.01
G35_Si08	35.0	Silica	8.3	3.5	6.50E-05	0.01
G50_Si08	50.0	Silica	8.3	3.5	9.33E-05	0.01

Table 5.2. Experimental design for estimating heterogeneous collision efficiency

Experiment Name	Mean Shear Rate (G_m, s⁻¹)	Sediment Type	Sediment Loading (mg/L)	Oil Loading (mg/L)	Sediment:Oil Volume Ratio	K" (mL μm⁻³ s⁻¹)	α_{HET}
Effects of Mean Shear Rate							
G05_Cl08_Oil12	5.0	Clay	8.3	12.5	1:3	6.59E-11	0.61
G20_Cl08_Oil12	20.0	Clay	8.3	12.5	1:3	2.47E-10	0.55
G35_Cl08_Oil12	35.0	Clay	8.3	12.5	1:3	5.52E-10	0.63
G50_Cl08_Oil12	50.0	Clay	8.3	12.5	1:3	1.01E-09	0.58
G05_Si08_Oil12	5.0	Silica	8.3	12.5	1:4	8.53E-11	0.38
G20_Si08_Oil12	20.0	Silica	8.3	12.5	1:4	3.50E-10	0.41
G35_Si08_Oil12	35.0	Silica	8.3	12.5	1:4	6.14E-10	0.38
G50_Si08_Oil12	50.0	Silica	8.3	12.5	1:4	1.08E-09	0.39
Effects of Sediment:Oil Ratio							
G20_Cl08_Oil06	20.0	Clay	8.3	6.2	2:3	2.39E-10	0.62
G20_Cl08_Oil01.3	20.0	Clay	8.3	1.3	6:1	2.53E-10	0.64
G20_Si08_Oil06	20.0	Silica	8.3	6.2	1:2	3.37E-10	0.44
G20_Si08_Oil01.3	20.0	Silica	8.3	1.3	5:1	3.46E-10	0.46

effects of sediment-crude oil concentration ratios on heterogeneous collision efficiency

(α_{HET}).

Parameter Estimation Procedure

In this research, twenty-four data sets were used for parameter estimation. The

fixed parameters used in the simulation are shown in Table 5.3.

Table 5.3. Fixed parameters used in the coalesced sphere model

Parameters	Values
Absolute temperature (T)	293 K
Density of water (ρ_w)	1.0 g cm^{-3}
Dynamic viscosity (μ)	1.04 x 10^{-2} g cm^{-1} s^{-1}
Density of Weathered Crude Oil	0.9 g cm^{-3}
Density (wet) of Silica	3.0 g cm^{-3}
Density (wet) of Clay	2.4 g cm^{-3}

The raw Coulter Counter data, which has 256 size categories, was compressed to 32 size

discretized categories (Ernest *et al.*, 1995). In the single particle type simulations, all

parameters except α_{HOMO} were treated as fixed parameters. In the two particle type

simulations, $\alpha_{HOMO,1}$ and $\alpha_{HOMO,2}$ values were taken from the results of single particle

type simulations, leaving only α_{HET} as the single "free" parameter. In all the parameter

estimation simulations, all parameters except α were treated as fixed parameters. The

Newton Rhapson method implemented in the nonlinear parameter estimation algorithm

PARMEST (Ernest *et al.*, 1991) was used in this simulation to find the optimum value of

the "free" parameter. All computer simulations for the parameter estimations were

compiled with Lahey Fortran 95 and performed on an Dell personal computer equipped with an Intel Pentium 4 CPU 2.0GHz.

RESULTS AND DISCUSSION

Single Particle Type Aggregation

A characteristic of a flocculation experiment is the reduction in the number of particles over time. To estimate first order aggregation rate constants (K') in a shear reactor, the initial rate of change in total particle concentration ($C(t)$) with time (t) due to shear aggregation is given by

$$\left(\frac{dC(t)}{dt}\right) = -K'C(t) \tag{5.11}$$

The solution of the differential equation 5.11 is given by equation 5.12

$$\ln\left(\frac{C}{C(0)}\right) = -K't \tag{5.12}$$

where $C(0)$ is the initial number concentration. K' is determined for these data sets through linear regression of the left hand side of equation 5.12 versus time. Values for the total particle number $C(t)$ are related to the moment of the size distribution

$$C = \sum_{q=1}^{c_{density}} \sum_{k=1}^{c_{volume}} n_{k,q} \tag{5.13}$$

Total particle volume V is calculated by the following

$$V = \sum_{q=1}^{c_{density}} \sum_{k=1}^{c_{volume}} n_{k,q} v_k \tag{5.14}$$

where v_k is the median particle volume in size class k. For a batch system, total particle volume remains constant.

Figure 5.1 illustrates the reduction of particle number concentration due to aggregation in a batch system. The total particle volume concentration, plotted as $\ln(V/V_o)$ on the secondary y-axis, remained constant because the batch system did not permit particles to settle and be removed from the system. The slope K' (Figure 5.1, equation 5.12), represents the rate of change of the total particle number. More rapid flocculation corresponds to larger absolute values of K'. Table 5.1 lists K' values for experiments with different mean shear rates G_m and single particle systems (oil droplets, clay, or colloidal silica). In general, increased shear rates resulted in more rapid flocculation (larger absolute value of K'). Significant differences in K' values result from differences in particle collision efficiencies (α_{HOMO}). At higher shear rates collision frequency increased, thus increasing the opportunity for a "successful" collision to occur. However, a lower K' magnitude suggests a lower collision efficiency (α_{HOMO}) for flocculation. Assuming equal collision frequencies at a given G_m, the α_{HOMO} value for silica is significantly less than those for crude oil droplets or clay.

Using inverse parameter estimation and the flocculation model, α_{HOMO} values for silica, clay, and crude oil were estimated (Table 5.1). For a given particle type, α_{HOMO} values remained relatively constant within the mean shear rates tested. This result supports the modeling assumption that α_{HOMO} is primarily a function of particle surface chemistry. Additionally, for oil, silica, and clay, α_{HOMO} values are significantly different from each other. The average α_{HOMO} value for silica (0.01) was an order of magnitude lower than that of clay ($\alpha_{HOMO} = 0.7$) or oil ($\alpha_{HOMO} = 0.3$) aggregation, as predicted by the first order flocculation rates. These results are consistent with the characterization of
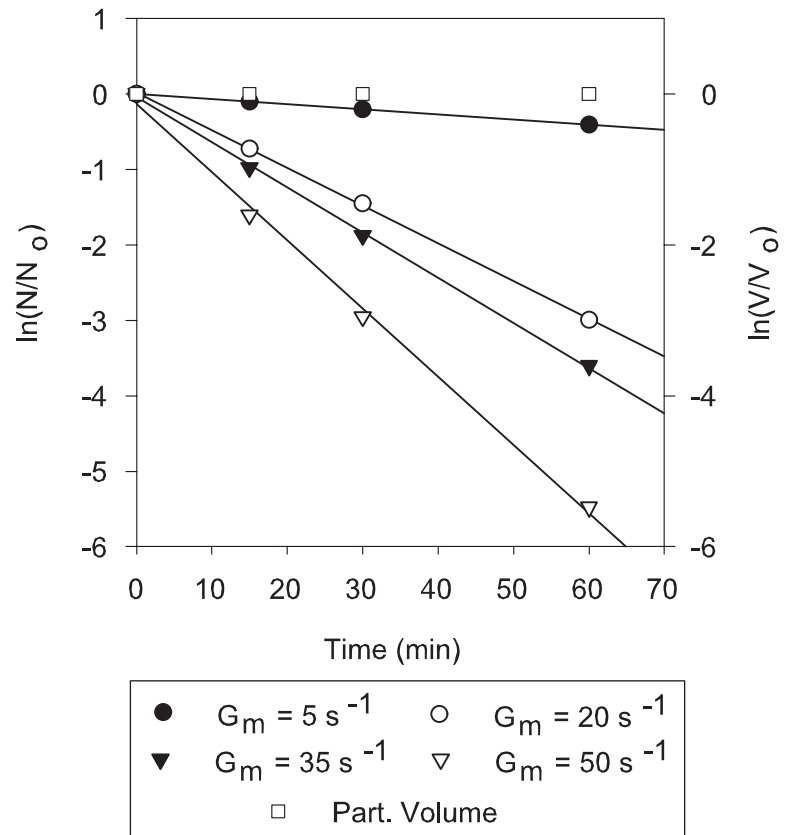
Figure 5.1. Change in total particle number versus mean shear rate as a function of time for clay aggregation (clay concentration = 8 mg/L). Total particle volume constant for all experiments

silica as a non-flocculating sediment and clay as a cohesive sediment (Edzwald *et al.*, 1974; Stumm and Morgan, 1995). The estimated α_{HOMO} values for clay and oil was similar to that obtained by others for coagulation in seawater solutions (Farley and Morel, 1986; Gibbs, 1983; Sterling *et al.*, 2002).

Surface chemistry is the primary cause of different α_{HOMO} values for clay, oil, and silica particles. Clay particles have a weak negative charge, and are attracted to the polarized water molecules, which attract more clay particles. This attraction results in a strong cohesion between clay particles and a relatively high α_{HOMO} value. Oil droplets are cohesive in aqueous systems because of hydrophobic attraction. Theoretical and experimental studies indicate that the reorientation, or restructuring, of water around non-polar surfaces is entropically very unfavorable, since it disrupts the existing water structure and imposes a new and more ordered structure on the surrounding water molecules (Israelachvili, 1992). Silica particles are not attractive as they do not bind with water molecules. Thus, silica particles have a low α_{HOMO} value.

The flocculation parameters (α_{HOMO} and K') determined from these experiments are useful in addressing issues of resurfacing of entrained crude oil or resedimenting of suspended sediment in coastal areas. This is discussed further below in the *Sediment-Oil Aggregation Simulation* section. Additionally, α_{HOMO} values for clay, silica, or oil systems were used as constants in the multi-particle aggregation model.

Sediment-Oil Aggregation

A second order rate expression is used to estimate the loss of "free" oil droplets to aggregation with sediment flocs in a two-particle type mixed batch system:

$$r_{oil\,loss} = \frac{dV_{oil}}{dt} = -K''V_{oil}\left(V - V_{oil}\right) \tag{5.15}$$

Free oil droplets are classified by a density class q. The total particle volume V_q in a given density class q is calculated as the following:

$$V_q = \sum_{k=1}^{c_{volume}} n_{k,q} v_k \tag{5.16}$$

where v_k is the median particle volume in size class k. If $V_{oil} = [A]$ and $V - V_{oil} = [B]$, then the solution of the differential equation 5.15 is given by 5.17.

$$\left(\frac{1}{[B]_o - [A]_o}\right)\ln\left(\frac{[A]_o[B]}{[A][B]_o}\right) = -K''t \tag{5.17}$$

Initial volume concentrations in equation 5.17 are indicated by the subscript o. Second order rate constants, K'', are determined through linear regression of the left hand side of equation 5.17 versus time.

As with single particle type systems, the K'' values (Table 5.2) for these two particle type experimental groups increase linearly with increasing mean shear rate. Additionally, the estimated α_{HET} values (Table 5.2) for clay-oil aggregates and silica-oil aggregates are approximately constant for a given sediment-oil system. This was somewhat surprising because of the radically different aggregation efficiencies of silica ($\alpha_{HOMO} = 0.01$) and clay ($\alpha_{HOMO} = 0.7$) systems. Because the α_{HOMO} value of crude oil systems ($\alpha_{HOMO} = 0.3$) is equal to that of clay-oil aggregates and silica-oil aggregates, it appears that the oil portion of mixed aggregates increase their overall aggregation.

Table 5.2 also lists the effects of relative oil-sediment concentration on α_{HET} values. Relative sediment-oil volumes (Table 5.2) ranged from 1:4 to 6:1. The relative

consistency in the estimated α_{HET} values suggests the probabilistic formulation of α_{OBS} is consistent with the experimental data for a range of sediment-oil ratios. Consequently, the assumption that the ratio of aggregate constituents on the surface is equal to the ratio of the constituent volumes in the aggregate seems valid. The validity of this assumption suggests that the surface character of sediment-oil aggregates was not disproportionately impacted by the oil or sediment constituents. This result may be due partially to the relative sizes of the sediment and oil droplets (Mennon and Wasan, 1988). For the formation of solid-stabilized emulsions, researchers have recommended that the solid particles are less than 1/10 the volume of the liquid droplets (Mennon and Wasan, 1988). The order in which the crude oil and sediment were mixed (Mennon and Wasan, 1988) may also be important in not creating stable dispersions. For surf washing applications, authors have noted that sediment encases oil droplets, providing a barrier to aggregation (Lee, 2002). In that application, sediment was added to a crude oil dispersion. In this study, the oil was added to a sediment dispersion to simulate the effects of a crude oil spill in a coastal system. Further studies can be conducted to test the effects of the order of constituent addition on observed collision efficiencies.

Sediment-Oil Aggregation Simulation

Clay-oil aggregates and silica-oil aggregates are composed of subunits with nonidentical fractal dimension, a practice that has not been conventionally studied in fractal aggregation modeling. Thus, it was of interest to determine the correspondence between the aggregation model and experimental data. Figure 5.2 illustrate a time series of particle size distributions in terms of number concentrations and volume concentrations. In Figure 5.2, the number of small aggregates decreases with time while

the total number of larger aggregates increase. However, because the formed aggregates are larger and distributed over a broader size range the increase is not as obvious in Figure 5.2. The formation of larger aggregates is observable in the time series of particle volume distributions (Figure 5.2). The area under each of the size distribution curves corresponds to the total particle volume in the reactor. As the area corresponding to the smaller particles decreases with time, the area corresponding to the larger particles increases. In both cases, clear correspondence between predicted and observed concentration data is highlighted.

Figures 5.3a, 5.3b, and 5.3c show the evolution of clay-oil aggregates with different densities. The density range has been discretized into 4 equally spaced bins with midpoints of 0.9, 1.4, 1.9 and 2.4 g cm^{-3}, corresponding to aggregate clay volume fractions of 0.0-0.25, 0.26-0.50, 0.51-0.75, and 0.76-1.00, respectively. The total particle volume of a given density was calculated using equation 5.19 at each time.

The plots show how different initial clay-oil ratios impact the formation of oil-clay aggregates with different densities. In all cases, the volume fractions of particles with densities 0.9 and 2.4 decrease over time as clay and oil aggregate to form flocs with intermediate densities 1.4 and 1.9. The volume fractions with intermediate densities increased at approximately equal rates. For cases G20_Cl08_Oil12 and G20_Cl08_Oil06, the combined volume fraction of intermediate densities is greater than the combined volume fraction of the initial particle densities at 30 min. For the case

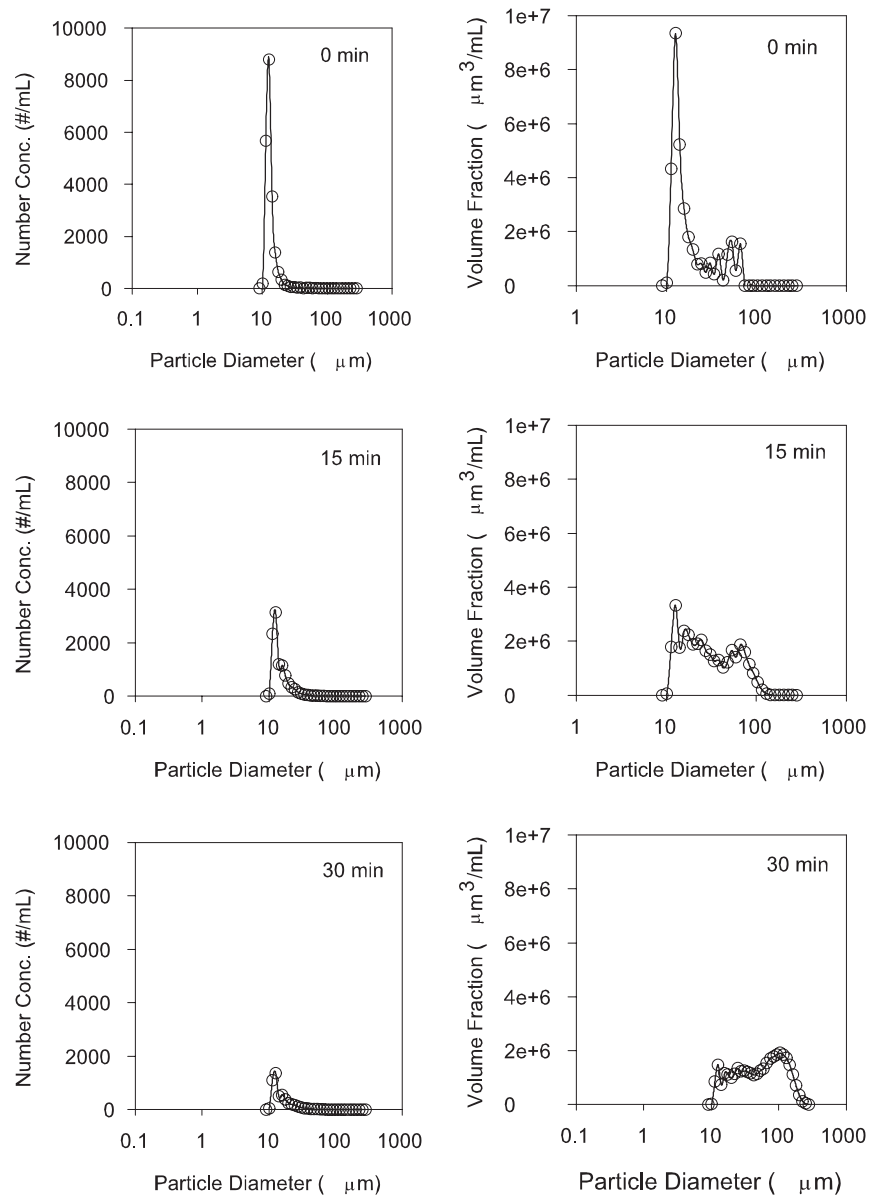Figure 5.2. Time series of particle number and particle volume concentrations (G20_Cl08_Oil12). Solid lines represent model predicted particle distributions; open symbols represent experimentally measured particle distributions

Figure 5.3. Formation of clay oil aggregates of different densities at different initial oil-clay ratios: (a) G20_Cl08_Oil12, (b) G20_Cl08_Oil06, and (c) G20_Cl08_Oil012

G20_Cl08_Oil012, the combined volume fraction of intermediate densities remains smaller than the combined volume fraction of the initial particle densities at 30 min. This was due in part to the larger mean volume of oil droplets, which resulted in clay-oil aggregates with a higher oil fraction.

Figures 5.4a, 5.4b, and 5.4c show the evolution of silica-oil aggregates with different densities. The density range has been discretized into 4 equally spaced bins with midpoints of 0.9, 1.6, 2.3 and 3.0 g cm^{-3}, corresponding to aggregate silica volume fractions of 0.0-0.25, 0.26-0.50, 0.51-0.75, and 0.76-1.00, respectively. In all cases, the volume fractions of particles with densities 0.9 and 3.0 decrease over time as silica and oil aggregate to form flocs with intermediate densities 1.6 and 2.3. As with the clay-oil systems, the volume fractions with intermediate densities increased at approximately equal rates. For cases G20_Si08_Oil12, G20_Si08_Oil06, and G20_Si08_Oil012, the combined volume fraction of intermediate densities is greater than the combined volume fraction of the initial particle densities at 30 min. In experiment G20_Si08_Oil012, the oil fraction has nearly been removed.

To estimate the relative influence of vertical dispersion, settling velocity and aggregation in particle removal, one can compare the time scales at which each of these processes occurs. First, using equation 5.14, equation 5.1 is written in terms of total volume V with density q

$$\frac{dV_q}{dt} = D_z \frac{\partial^2 V_q}{\partial z^2} - w_{k,q} \frac{\partial V_q}{\partial z} + K'' V_q \left(V - V_q \right) \qquad (5.18)$$
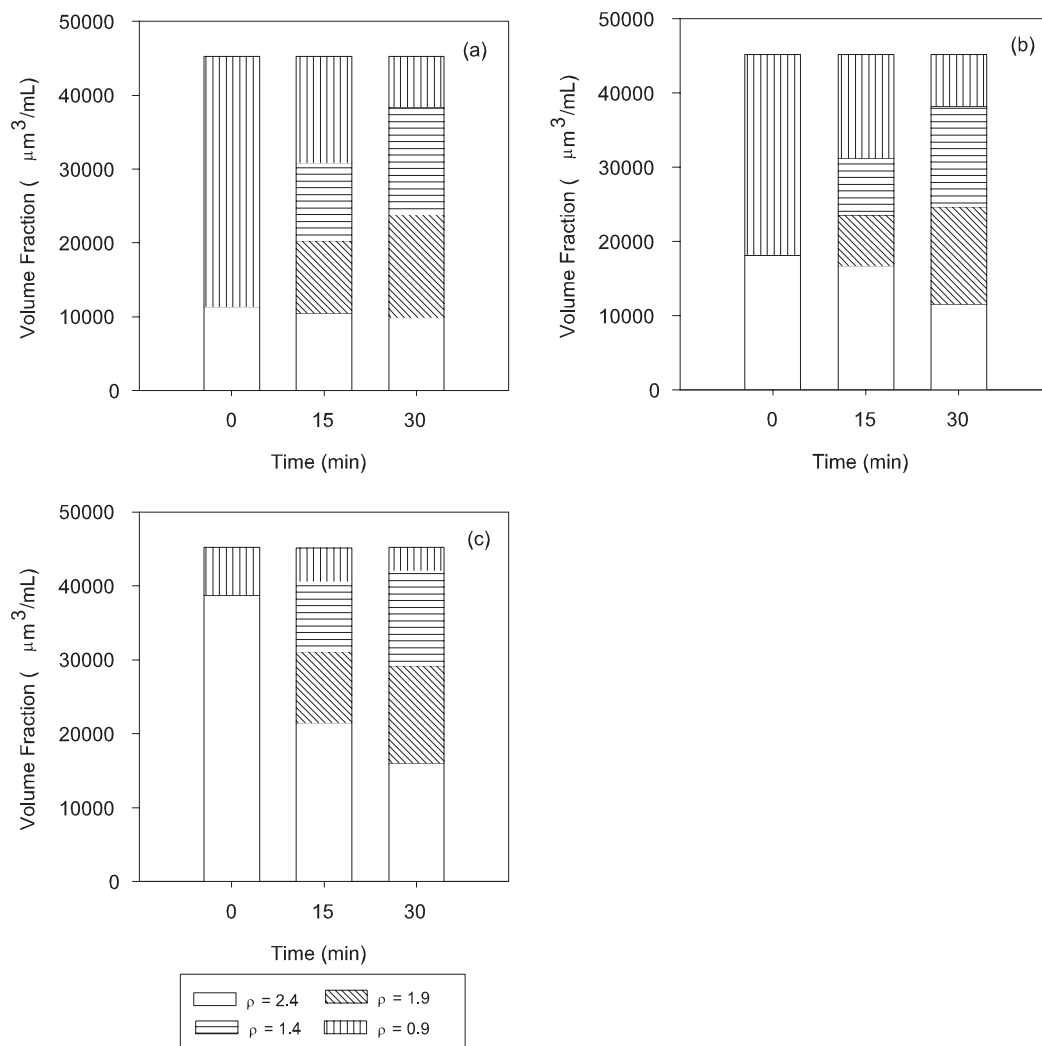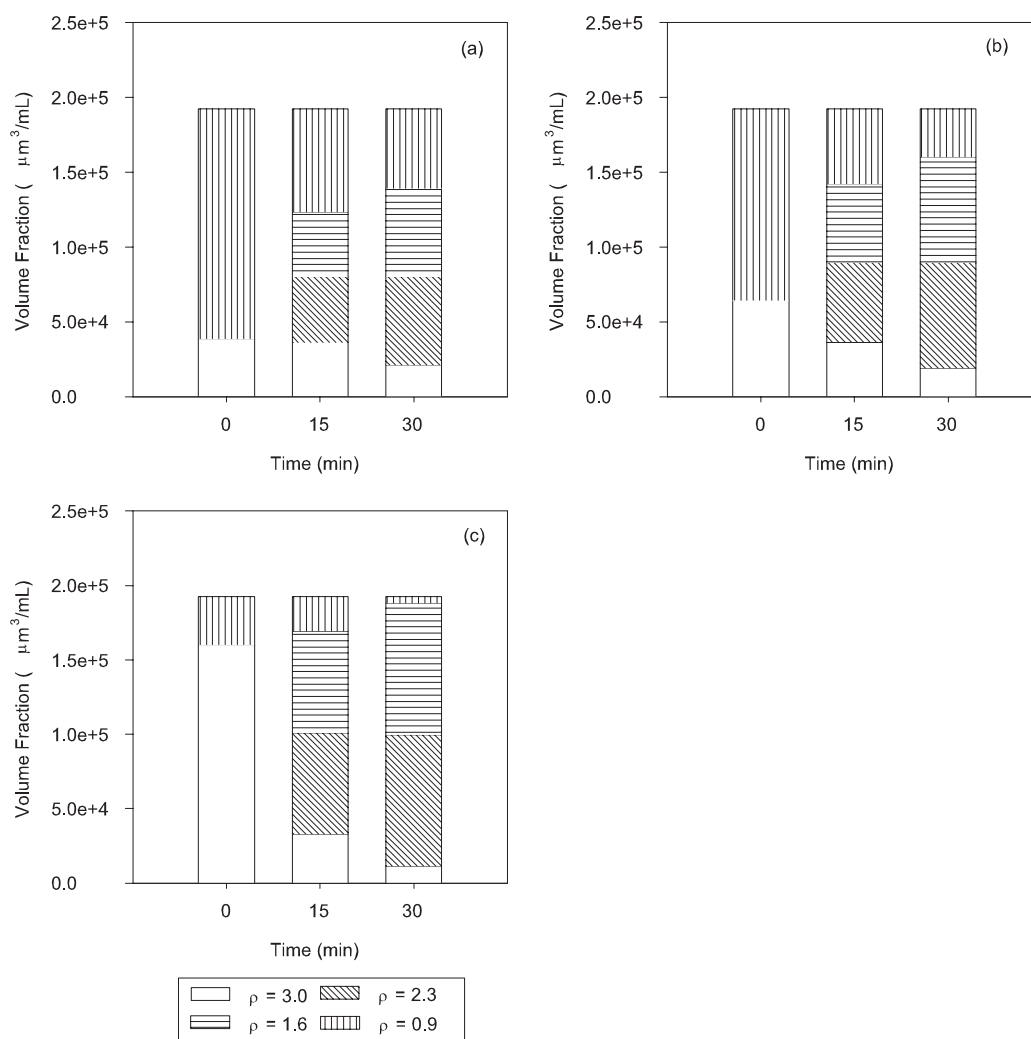
Figure 5.4. Formation of silica oil aggregates of different densities at different initial oil-silica ratios: G20_Si08_Oil12, (b) G20_Si08_Oil06, and (c) G20_Si08_Oil012

The nonlinear aggregation kinetic expression has been replaced with a second order rate expression (equation 5.15), in which the apparent second order reaction rate constant K_q'' was estimated from model results. Equation 5.18 is nondimensionalized by letting $\psi_q = V_q/V_q(0)$, $\zeta = z/Z$, and $\tau = tw_{k,q}/Z$

$$\frac{d\psi_q}{d\tau} = \frac{D_z}{w_{q,avg}Z}\frac{\partial^2\psi_q}{\partial\zeta^2} - \frac{\partial\psi_q}{\partial\zeta} + \frac{K_q''[B]_o\psi_q Z}{w_{q,avg}}$$

(5.19)

where Z is a characteristic depth, $[B]_o$ is as defined in equation 5.17, and $w_{q,avg}$ is the volume averaged particle settling velocity as defined in the following:

$$w_{q,avg} = \frac{1}{V_q}\sum_{k=1}^{c_{volume}} w_{k,q}v_k$$

(5.20)

For this case, Z is specified as 2m, the mixed layer depth of a coastal estuary. The quantity $(K_q''[B]_oZ/w_{q,avg})$ appearing in equation 5.19 is called the Damköhler number for convection, Da, and physically represents the ratio

$$Da = \frac{rate\ of\ consumption\ of\ V_q\ by\ reaction}{rate\ of\ transport\ of\ V_q\ by\ convection} = \frac{K_q''[B]_o Z}{w_{q,avg}}$$

(5.21)

For a single type particle system (silica, clay, or oil only), the nonlinear kinetic expression in 5.1 has been replaced with a first order rate expression $(dV_q/dt = K'V_q)$, in which K' was estimated from experiment data. After nondimensionalizing the vertical transport equation as above, the Damköhler number is the following

$$Da = \frac{rate\ of\ consumption\ of\ V_q\ by\ reaction}{rate\ of\ transport\ of\ V_q\ by\ convection} = \frac{K_q'Z}{w_{q,avg}}$$

(5.22)

If Da<<1, then particle settling rates are much faster than the aggregation rates and particle aggregation can be ignored with negligible error. Average settling rates were
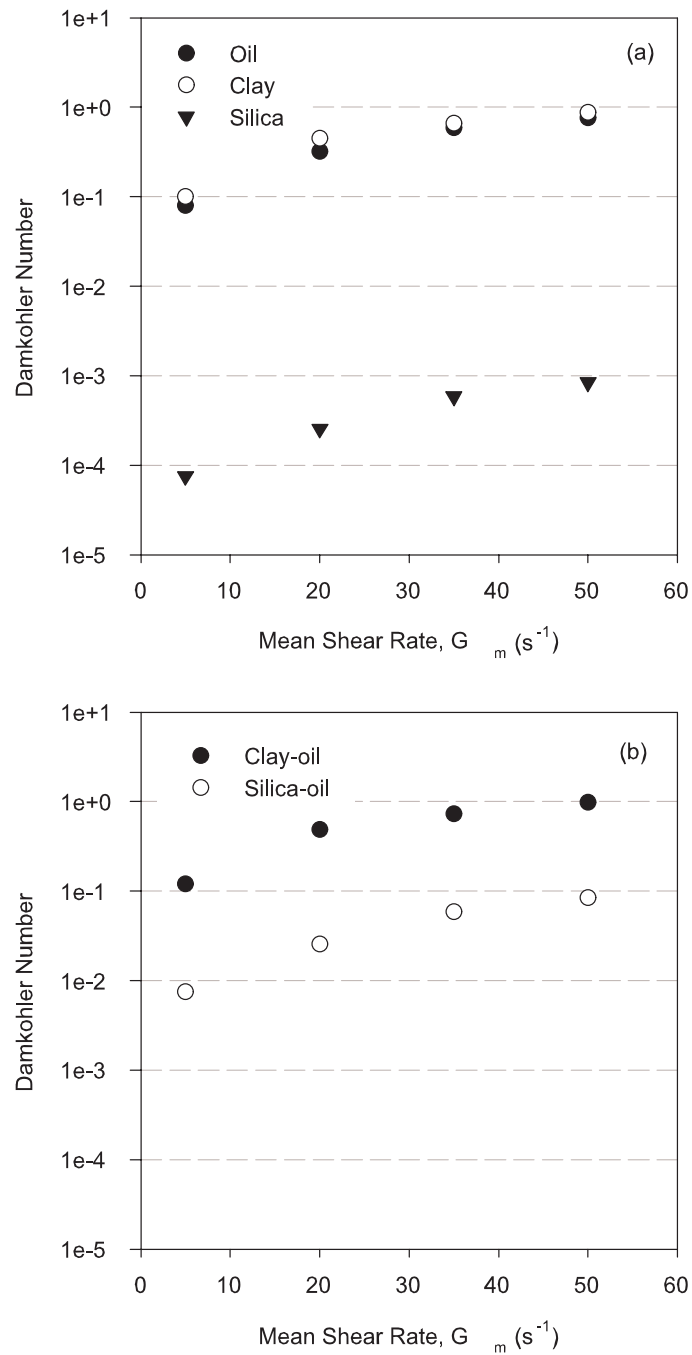
Figure 5.5. Effect of shear on aggregation Damköhler (Da) number for (a) single particle systems and for (b) oil in two particle type systems in a 2 meter settling column

calculated using equations 5.4 and 5.20. Da numbers for each single particle type systems (Figure 5.5a) and two particle type systems (Figure 5.5b) have been calculated for a range of G_m values. Based on these values, aggregation processes may be significant in all cases for clay systems and oil systems, but insignificant for silica systems. The removal of oil by clay sediments may be significant in mixed particle type systems. Because of the higher settling velocity of silica particles relative to clay, the removal of oil by silica is less than by clay.

Overall, the presented aggregation model can be used to study a number of problems related to sediment and oil aggregation and transport. Natural clay-oil flocculation after a crude oil spill has been termed surf washing and is of interest in the spill responder community. Additionally, the transport and fate of physically or chemically dispersed spilled crude oil in coastal environments can be more accurately modeled by including potential interactions with suspended sediments. Accurately describing each of the above scenarios is important in understanding ecological risks presented by response countermeasures to an oil spill.

CHAPTER VI

DETERMINATION OF COLLISION EFFICIENCIES FOR FLOCCULENT PARTICLE TRANSPORT MODELS: HETEROGENEOUS FRACTAL SYSTEMS

OVERVIEW

Conventional aggregation kinetic models do not describe flocculation between particles with different fractal dimensions and densities as expected in estuarine and coastal environments. This chapter describes a modeling approach that simulates changes in particle size distribution (PSD), fractal dimension, and floc density due to aggregation. Model predictions were compared with a series of PSD data obtained from laboratory batch coagulation data collected from clay, colloidal silica, emulsified crude oil, clay-crude oil, and silica-crude oil systems. In the parameter estimation algorithm, the minimized objective function, mean of the sum of the squares of the relative residuals (MSSRR), was a relative least squares residual rather than the typical unweighted least squares residual. The mCFS model had MSSRR values up to 15% lower than that obtained using the Euclidean model. For the mCFS model, estimated D values were between 2.6 and 3.0. Values of α_{HOMO} or α_{HET} were also up to 50% lower in the mCFS model than those obtained using the Euclidean model. D values estimated by the mCFS model were higher than that estimated experimentally by the particle concentration technique (PCT). For a given aggregate mass, reducing an aggregate's fractal dimension lowered its settling velocity. Thus, the timescale of sedimentation

becomes greater than that of clay-oil aggregation. Thus, the mCFS model provides clearer insights to the fate of spilled oil in coastal environments.

INTRODUCTION

In traditional water quality models, colloidal aggregate structures and formation are important for understanding the fate and transport of contaminants. Developments in fractal geometry and aggregation modeling have been successful in describing the morphology and formation kinetics of aggregate structures (Lee *et al.*, 2000; 2002). Most of these models assume that all particles in the system of interest are identical in size, shape, and other physicochemical properties. However, in most environmental systems, aggregation occurs between particles of different sizes and physicochemical properties. For these more complex systems, models proposed for the simulation of aggregation dynamics include simple empirical models (Serra and Logan, 1999) and two- and three-dimensional lattice simulations (Stoll and Buffle, 1996). Empirical models generally assume an average fractal dimension and do not give information regarding the evolution of the floc fractal dimension. Conversely, two- and three-dimensional lattice simulations provide detailed information regarding particle aggregate interactions and morphological evolution. However, these types of simulations are not integrated with transport models, making them less useful for parameter estimation in environmental systems.

Recently, an aggregation model for fractal flocs was presented based on a set of coalesced fractal sphere (CFS) assumptions (Lee *et al.*, 2000). Relaxing the CFS assumptions in the aggregation model would allow the introduction of multiple

monomer densities and aggregate fractal dimensions. Coupling this model with a parameter estimation program allows systematic experimental studies of aggregation in complex aquatic systems.

There are environmentally relevant applications in which systems of mixed populations of solid particles and emulsion droplets occur. Examples in engineered and natural systems include oil-assisted removal of coal fines from water and emulsion stabilization by solid particles. Modeling the aggregation of colloidal crude oil droplets with suspended aquatic sediments is of interest for understanding the fate and transport of crude oil from natural seeps and human releases in nearshore waters. Because the density of oil is less than water, oil droplet coalescence leads to increased surfacing. Similarly, oil aggregation with suspended sediment can lead to settling to the benthic layer.

This chapter presents the application of a modified coalesced sphere fractal (mCFS) aggregation model to a system of solid floc aggregates and emulsified droplets. Specifically, we tested whether the Euclidean or mCFS model fit observed data sets better. This involved non-linear parameter estimation techniques to determine free parameters (fractal dimension and collision efficiency). The minimized objective function (MSSRR) was a relative least squares residual rather than the typical unweighted least squares residual. In all cases, α_{HOMO} or α_{HET} values estimated by the mCFS model were equal to or lower than that estimated using the Euclidean model. Additionally, MSSRR values are lower for the mCFS model than for the Euclidean model, meaning that the mCFS model fits the experimental data better. D values

estimated by the mCFS model were lower than that estimated by the Euclidean model but higher than that estimated experimentally by the particle concentration technique (PCT). For a given aggregate mass, reducing an aggregate's fractal dimension lowered its settling velocity. Thus, the timescale of sedimentation becomes greater than that of clay-oil aggregation. Thus, the mCFS model provides clearer insights to the transport and aggregation within oil-sediment systems.

METHODS

Modeling Background

Fractal aggregates have an aggregate mass that is explained by a power law relationship:

$$m \propto d^D \tag{6.1}$$

where m is the aggregate mass, d is the characteristic length of aggregate, and D is the fractal dimension. The fractal dimension represents the structure of the aggregate with higher fractal dimensions indicating denser structure. For fractal aggregates, density is also inversely related to aggregate size. A fractal dimension of 3.0 represents a uniformly distributed structure or, more commonly, a compact structure.

In the three-dimensional space of Euclidian geometry, the number (N) of spherical monomers with diameter d_o that can be packed into a larger sphere of diameter d is (Feder, 1988):

$$N = \zeta \left(\frac{d}{d_o} \right)^3 \tag{6.2}$$

where ζ is a packing factor indicating how the monomers are packed. This equation applies only in the limit $d/d_o \gg 1$. The value of ζ depends on shapes of both the cluster and the monomers, and on the degree of packing. In the case of spherical monomers, $\zeta = \pi/(3\sqrt{2}) = 0.7405$ for close cluster packing, and $\zeta = 0.637$ for random cluster packing (Feder, 1988).

The conventional CS assumption is equivalent to

$$N = \left(\frac{d}{d_o} \right)^3 \tag{6.3}$$

i.e., ζ is assumed to be unity. This means that there is no pore space in the aggregate due to packing effects.

In contrast, for the case of fractal aggregates, the following relationship exists (Feder, 1988):

$$N = \zeta \left(\frac{d}{d_o} \right)^D \tag{6.4}$$

where D is the fractal dimension. This equation applies also in the limit $d/d_o \gg 1$. For fractal aggregates in this work, d is the encased diameter of a fractal aggregate, following Jiang and Logan's (1991) definition of the characteristic length of a fractal aggregate as the longest aggregate length. Definitions of diameter used by others include hydraulic diameter or the diameter based on the radius of gyration (Jackson *et al.*, 1995).

The CFS assumption is equivalent to

$$N = \left(\frac{d}{d_o}\right)^{D}$$
(6.5)

where $\zeta = 1$ again, meaning that there is no pore space in the spherical fractal aggregate due to packing effects (Lee *et al.*, 2000). In fractal aggregates, the interparticle pore space in an aggregate is considered to come from two sources (Jiang, 1993): the fractal nature and the packing effects. The fractal nature is related to the fundamental aggregation process, and the packing effects are related to the shapes of the monomers and the aggregates. So when the packing factor is assumed as unity, it means that there is no pore space resulting from the shape effects of the aggregates. However, pore space resulting from shape effects is less important than that due to the essential fractal nature, represented by the fractal dimension parameter (Lee *et al.*, 2000). Thus, this approach results in simplification of the fractal modeling approach while still conveying the core nature of fractal aggregation dynamics.

The derived basic equations for the modified coalesced fractal sphere (mCFS) assumptions are summarized in Table 6.1. The porosity and density of aggregate q, formed from monomers p_1 and p_2, are calculated using these relations. In this analysis, p_1 and p_2 have been defined as having equal volumes. Thus, the porosity of the aggregate q can be calculated as

$$e = \frac{\left(N_{p_1} + N_{p_2}\right) v_o}{v_a} = \frac{N_{TOT} v_o}{v_a}$$
(6.6)

where $v_o = \pi d_o^3/6$ and $v_q = \pi d^3/6$ are the monomer and aggregate volumes.

Table 6.1. Basic equations for fractal aggregates under the modified coalesced fractal sphere assumption

Description	Equations	Description	Equations
Monomer Volume	$v_s = v_{o,1} = v_{o,2}$	Floc Diameter	$d = \left(\dfrac{\pi}{6}\right)^{-\frac{1}{3}} v_o^{(\frac{1}{3}-\frac{1}{D})} v_s^{(\frac{1}{D})}$
Monomer Diameter	$d_o = \dfrac{6}{\pi}(v_o)^{\frac{1}{3}}$	Floc Encased Volume	$v_a = \dfrac{\pi}{6} d^3$
Conserved Mass	$m = m_{o,1} N_{o,1} + m_{o,2} N_{o,2}$	Floc Packing Porosity	$\varepsilon = 1 - \left(\dfrac{d}{d_o}\right)^{D-3}$
Conserved Volume	$v_s = v_{s,1} + v_{s,2}$	Floc Density	$\rho = \rho_o(1-\varepsilon) + \rho_{H_2O}\varepsilon$
Conserved Density	$\rho_o = \dfrac{m}{v_s}$	Settling Velocity	$w_s = \dfrac{g}{18\mu}\left(\dfrac{\rho - \rho_{H_2O}}{\rho_{H_2O}}\right) d_o^{3-D} d^{D-1}$

Combining this result with equation 6.5, the aggregate porosity is

$$e = 1 - \left(\frac{d}{d_o}\right)^{D-3} \tag{6.7}$$

The density of aggregate q is calculated as the following:

$$\rho_q = (1-e)(x_{p1}\rho_{p1} + x_{p2}\rho_{p2}) + e\rho_{H2O} \tag{6.8}$$

where x_{p1} is the number fraction of monomer p_1 in aggregate q ($=N_{p1}/N_{TOT}$) and x_{p2} is

the number fraction of monomer p_2 in aggregate q ($=N_{p2}/N_{TOT}$). Note that both the

aggregate porosity and density are functions of size if $D < 3$. For a given D, the density

of the aggregate decreases as the size of the aggregate increases, and the porosity of the

aggregate increases as the size of the aggregate increases. This is the core nature of the

fractal properties of aggregates. Therefore, although the resulting equations based on the

mCFS assumption are relatively simple, they convey the essential characteristics of

fractal aggregates.

When a new aggregate is formed, the number of monomers in the new aggregate

is equal to the sum of the monomers in each of the colliding aggregates. Thus, the

monomer volume is conserved in the aggregation process. Aggregate conserved volume

v_s is related to its length d by the following

$$v_s = \frac{\pi}{6} d_o^{3-D} (d)^D \tag{6.9}$$

where D is the cluster fractal dimension, d_o the monomer diameter, and d the aggregate

diameter. For an aggregate q formed from the collision of o and p aggregates, a

conserved density can be defined as the following:

$$\widetilde{\rho}_q = \frac{m_o + m_p}{v_{s,o} + v_{s,p}}$$ (6.10)

where m_o and m_p are the masses of aggregates m_o and m_p. The conserved density is equal to the actual aggregate density when $D = 3$. The length of the newly formed aggregate q is determined from

$$\lambda_q = \lambda_o + \lambda_p$$ (6.11)

where $\lambda = d^D$ is a fundamental, conserved quantity of the aggregation interaction, d is the aggregate characteristic length, and D is the aggregate fractal dimension (Jackson, 1998). In this study, it was assumed that the fractal dimension of the new aggregate can be calculated by the following:

$$D_q = y_o D_o + y_p D_p$$ (6.12)

where y_o and y_p are the volume fractions of aggregate o and p in aggregate q.

In summary, the mCFS assumptions are defined as the following: 1) All aggregates consist of monomers that are compact spheres but may have different fractal dimensions and densities; 2) All aggregates in the particular system have spherical forms with a fractal dimension defined by the relative monomer concentration, independent of aggregate size; and 3) When two aggregates collide and attach, the conserved volume of the newly formed aggregate is the sum of the conserved volumes of the colliding aggregates. The mCFS assumptions simplify to the CS assumption when the system has a single monomer density and $D = 3$.

Since coagulation may affect particle settling rates, one may need to consider coagulation and settling simultaneously to describe sedimentation kinetics. For a

settling column, the dynamic equation for the particle size distribution is described by the following:

$$\frac{dn_{k,q}}{dt} = D_z \frac{\partial^2 n_{k,q}}{\partial z^2} - w_{k,q} \frac{\partial n_{k,q}}{\partial z} + \theta_{k,q} \qquad (6.13)$$

where $n_{k,q}$ is the particle size distribution, given as the number concentration of particles as a function of particle volume (k) and conserved density (q) (number mL^{-1}), z is the vertical distance from the top of the water column, D_z is the vertical dispersion coefficient, $w_{k,q}$ is the settling velocity of particle volume (k) and conserved density (q), and $\theta_{k,q}$ is the interaction term due to coagulation. The settling velocity is assumed to follow Stokes law; therefore

$$w_{k,q} = \frac{g}{18\mu} \frac{\left(\tilde{\rho}_q - \rho_{H_2O}\right)}{\rho_{H_2O}} d_o^{3-D} d^{D-1} \qquad (6.14)$$

where d is the particle diameter and g is the gravitational constant (980.0 cm^2/s). The interaction term, $\theta_{k,q}$, represents the particle contact mechanisms of Brownian motion, fluid shear, and differential sedimentation. It is represented by the following relationship:

$$\theta_{h,k,q} = \frac{dn_{h,k,q}}{dt} = \frac{1}{2} \sum_{M_{e,i,i}+M_{f,j,p}=M_{h,k,q}} \alpha_{obs}(o,p)\beta(e,f,o,p,i,j)n_{e,i,o}n_{f,j,p}$$

$$- n_{h,k,q} \sum_{o=1}^{c_{density}} \sum_{e=1}^{c_{fdim}} \sum_{i=1}^{c_{size}} \alpha_{obs}(o,q)\beta(e,h,o,q,i,k)n_{e,i,o} \qquad (6.15)$$

where i, j, and k denote particle diameter categories; o, p, and q denote conserved density categories; e, f, and h denote fractal dimension categories; $c_{density}$, c_{fdim} and c_{size} are the maximum number of conserved density, fractal dimension and diameter categories; $n_{e,o,i}$,

$n_{f,j,p}$, and $n_{h,k,q}$ are the number concentration of particle diameters $i, j,$ and $k,$ of conserved

particle densities $o, p,$ and $q,$ and of fractal dimensions $e, f,$ and h; $\alpha_{obs}(o,p)$ is the

observed collision efficiency function, which depends on the interparticle surface forces

(Table 6.2); and $\beta_{obs}(e,f,o,p,i,j)$ is the observed collision frequency function (Table 6.2),

which depends on the mode of interparticle contact. Equation 6.15 is a system of

discrete, nonlinear differential equations. The first term on the right-hand side of

equation 6.15 sums the rate of formation of particles of k-diameter, h-fractal dimension

and q-conserved density classes from all collisions of particles smaller than the k-size

particles. The summation is over all diameter classes i and j, all fractal dimension

classes e and f, and all conserved density classes o and p such that the mass of the sum

of the i-diameter, e-fractal dimension, o-conserved density particle and of the j-diameter,

f-fractal dimension, p-conserved density particle equals the mass of the k-size, h-fractal

dimension, q-conserved density particle:

$$M_{h,k,q} = M_{e,i,o} + M_{f,j,p} \tag{6.16}$$

In the particle conjunction represented by equation 6.16, mass is conserved. The second

set of summation terms reflects the loss of k-diameter, h-fractal dimension and q-

conserved density aggregates as they combine with all other aggregate sizes to form

larger aggregates.

Table 6.2. Equations for aggregate collision frequency and collision efficiency under the modified coalesced fractal sphere (mCFS) model

Observed Collision Frequency Function (Ernest *et al.*, 1995, Lee *et al.*, 2002)	
$\beta_{obs,efopij} = \beta_{Br,ij} + \beta_{sh,ij} + \beta_{ds,efopij}$	
Collision Frequency Due to Brownian Motion	$\beta_{ij,Br} = \dfrac{2kT}{3\mu}\left(\dfrac{1}{d_i} + \dfrac{1}{d_j}\right)(d_i + d_j)$
Collision Frequency Due to Shear	$\beta_{sh,ij} = \dfrac{G_m}{6}(d_i + d_j)^3$
Collision Frequency Due to Differential Settling	$\beta_{ds,opij} = \dfrac{\pi}{4}(d_i + d_j)^2(w_i - w_j)$
Observed Collision Efficiency Function	
$\alpha_{obs}(o,p) = \alpha_{HOMO,1}(x_{p1,o})(x_{p2,o}) + \alpha_{HOMO,2}(x_{p1,p})(x_{p2,p}) + \alpha_{HET,1-2}(x_{p1,o}x_{p2,p} + x_{p1,p}x_{p2,o})$	

Summary of Experimental Methods

To estimate homogeneous and heterogeneous collision efficiency values, a series of batch mixing experiments were conducted. Detailed descriptions of reagents, experimental apparatus have been presented in chapter four. In the experiments, a 40-L batch mixing tank was used to measure changes in particle size distribution (PSD) under different experimental conditions. In the experiments, PSD was measured in-situ using a light scattering particle size analyzer (LISST-100, Sequoia Instruments, Bellevue, WA), and ex-situ using an electronic particle counter (Sampling Stand II and Multisizer, Coulter Electronics Limited, Hialeah, FL). Using this tank and artificial seawater, a series of experiments was performed to measure changes in PSD of bentonite clay, colloidal silica, chemically dispersed crude oil, clay-crude oil, and silica-crude oil systems. An initial set of experiments (Table 6.3) was conducted to determine the effects of particle type (crude oil, clay, or silica), mean shear rate (G_m), and aggregation model on estimated homogeneous collision efficiency (α_{HOMO}) and MSSRR values. A second set of experiments (Table 6.4) was conducted to determine the effects of sediment type (silica, clay), G_m, and aggregation model on heterogeneous collision efficiency (α_{HET}) MSSRR values. The PCT method (Logan and Wilkinson, 1991) was used to determine average D values at the end of each for each single and two monomer type aggregation experiment.

Table 6.3. Effect of particle type and mean shear rate on homogeneous collision efficiency (α_{HOMO})

Experiment	G (s^{-1})	Part. Type	Nominal Conc. (mg/L)	Euclid. Rect. Model		Fractal Rectilinear Model		
				α	MSSRR	α	D	MSSRR
G05_Cl08	5	Clay	8	0.77	0.14	0.43	2.6	0.08
G20_Cl08	20	Clay	8	0.78	0.09	0.63	2.7	0.07
G35_Cl08	35	Clay	8	0.77	0.16	0.68	2.8	0.14
G50_Cl08	50	Clay	8	0.76	0.13	0.76	3.0	0.13
G05_Oil12	5	Oil	12	0.25	0.17	0.25	3.0	0.17
G20_Oil12	20	Oil	12	0.22	0.13	0.22	3.0	0.13
G35_Oil12	35	Oil	12	0.28	0.14	0.28	3.0	0.14
G50_Oil12	50	Oil	12	0.24	0.08	0.24	3.0	0.08
G05_Si08	5	Silica	8	0.01	0.22	0.01	3.0	0.22
G20_Si08	20	Silica	8	0.01	0.18	0.01	3.0	0.18
G35_Si08	35	Silica	8	0.01	0.07	0.01	3.0	0.07
G50_Si08	50	Silica	8	0.01	0.20	0.01	3.0	0.20

Table 6.4. Effect of particle type and mean shear rate on heterogeneous collision efficiency (α_{HET})

Experiment	G (s^{-1})	Sed. Type	Nominal Sed. Conc. (mg/L)	Euclid. Rect. model		Fractal Rectilinear Model		
				α	MSSRR	α	D	MSSRR
G05_Cl08_Oil12	5	Clay	8	0.61	0.13	0.57	2.7	0.09
G20_Cl08_Oil12	20	Clay	8	0.55	0.17	0.53	2.8	0.15
G35_Cl08_Oil12	35	Clay	8	0.63	0.23	0.63	3.0	0.23
G50_Cl08_Oil12	50	Clay	8	0.58	0.22	0.58	3.0	0.22
G05_Si08_Oil12	5	Silica	8	0.38	0.13	0.36	2.8	0.09
G20_Si08_Oil12	20	Silica	8	0.41	0.13	0.41	3.0	0.13
G35_Si08_Oil12	35	Silica	8	0.38	0.21	0.38	3.0	0.21
G50_Si08_Oil12	50	Silica	8	0.39	0.11	0.39	3.0	0.11

Parameter Estimation Procedure

In this research, twenty-four data sets were used for parameter estimation. The fixed parameters used in the simulation are shown in Table 6.5.

Table 6.5. Fixed parameters used in the fractal simulation

Parameters	Values
Absolute temperature (T)	293 K
Density of water (ρ_w)	1.0 g cm^{-3}
Dynamic viscosity (μ)	1.04 x 10^{-2} g cm^{-1} s^{-1}
Density of Weathered Crude Oil	0.9 g cm^{-3}
Density (wet) of Silica	3.0 g cm^{-3}
Density (wet) of Clay	2.4 g cm^{-3}

The raw Coulter Counter data, which has 256 size categories, was compressed to 32 size discretized categories (Lee *et al.*, 2002; Ernest *et al.*, 1995). In the single particle type simulations, all parameters except α_{HOMO} and D were treated as fixed parameters. In the two particle type simulations, α_{HOMO} for free sediment and oil droplets and D for oil droplets were taken from the results of single particle type simulations, leaving D for sediment and α_{HET} as the "free" parameters. Experimentally measured initial PSDs, D and α_{HOMO} values in two particle type systems, and monomer densities are coupled with an estimate of the "free" parameters. The correspondence of the experimental and calculated PSDs was measured using the mean of the sum of the squares of relative residuals (MSSRR), defined as

$$MSSRR = \frac{1}{N} \sum_{i=1}^{N} \left(\frac{\hat{y}_i - y_i}{y_i} \right)^2 \tag{6.17}$$

where N is the total number of observations, $\bullet_i$ and y_i are the predicted and the observed

number concentrations (# cm^{-3}) of each size category at each time of the ith observation,

respectively. The Newton Rhapson method implemented in the nonlinear parameter

estimation algorithm PARMEST (Lee *et al.*, 2002; Ernest *et al.*, 1991) was used in this

simulation to find the optimum value of the "free" parameters. All computer simulations

for the parameter estimations were compiled with Lahey Fortran 95 and performed on an

Dell personal computer equipped with an Intel Pentium 4 CPU 2.0GHz.

RESULTS AND DISCUSSION

Fractal vs. Euclidean Model Fit

  The main goal of this research was to investigate which modeling approach of

the two rectilinear coagulation models (Euclidean or mCFS) best described the observed

data PSD evolution. The mCFS model is a generalized form of the Euclidean rectilinear

model, i.e., under D = 3.0, the mCFS model is reduced to the Euclidean model. So, with

one more free parameter, D, the mCFS model should be better than, or at least as good

as, the Euclidean rectilinear model.

  The predicted volume distribution from the mCFS model is presented in Figure

6.1b using the optimum values of D and α_{HET} for Experiment G05_Cl08_Oil12 (Table

6.4). This graph is similar to the Euclidean rectilinear case (Figure 6.1a). Though the

difference is not obvious in the volume distribution graph, the predicted volume

concentrations of the larger size categories were higher than in the Euclidean rectilinear

case. Thus, the mCFS model makes predictions closer to the observed data in the larger

size categories, improving the overall model fit. Similar results were obtained by

previous researchers (Lee *et al.*, 2002).

Comparisons of the mean of the sum of the squares of the relative residuals (MSSRR) values provide another means of comparing the data fit between the Euclidean and mCFS models. The MSSRR served as a measure of the error between the model predictions and the observed PSD. Parameter estimation results are presented in table 6.3 for single monomer type systems and in table 6.4 for two monomer type systems. For silica particles and for oil droplets (table 6.3), the optimum estimated fractal dimension in using the mCFS model was equal to 3.0. In these cases, the mCFS model was equivalent to the Euclidean model and the MSSRR values were equal. For clay systems (table 6.3), the fractal dimension was generally less than 3. The resulting MSSRR values decreased in experiment G05_Cl08 from 0.14 in the Euclidean model to 0.08 in the mCFS model (42.8 %), in experiment G20_Cl08 from 0.09 to 0.07 (22.2%), and in experiment G35_Cl08 from 0.16 to 0.14 (12.5%).

A similar reduction of MSSRR values can be noted in the two monomer systems. For clay-oil systems, the MSSRR values decreased in experiment G05_Cl08_Oil12 from 0.13 to 0.09 (30.8 %) and in experiment G20_Cl08_Oil12 from 0.17 to 0.15 (11.7 %). The remaining clay-oil experimental systems produced estimated sediment fractal dimensions equal to 3.0. For one silica-oil experiment (G05_Si08_Oil12), a fractal dimension not equal to 3.0 was estimated. In this case, the MSSRR values decreased from 0.13 to 0.09 (30.8 %). The decrease of the MSSRR means the improvement of the model fitting, the improvement based on the criterion of the MSSRR (Lee *et al.*, 2000).
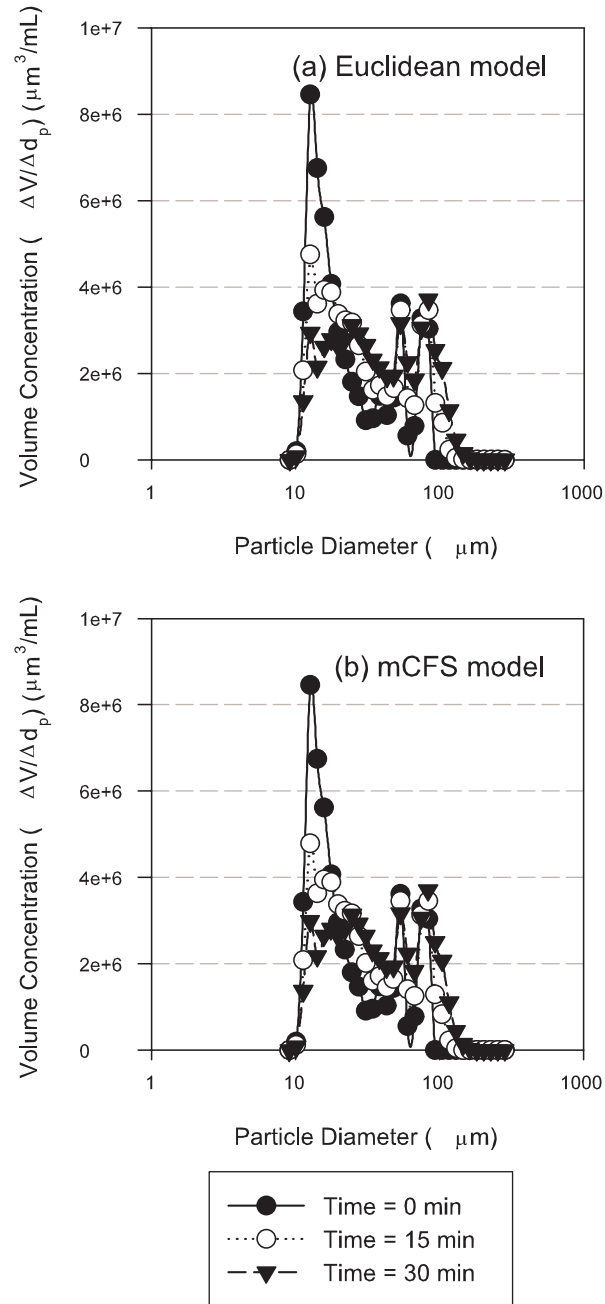
Figure 6.1. Volume distributions for Euclidean model (a) and fractal (mCFS) model (b) for experiment G05_Cl08_Oil12. Symbols are experimental data; lines are model predictions

Therefore, the mCFS model had a better fit to the observed data in all of these cases, and the level of improvement appears to be more significant when D drops more from 3.0.

Collision Efficiency

The effect of model type on estimated collision efficiencies should also be noted. In all experimental cases in which D < 3, the estimated α_{HOMO} (Table 6.3) and α_{HET} (Table 6.4) values are lower in the mCFS model than in the Euclidean model. The explanation for lower α's with lower fractal dimension results from the fact that a floc with a lower fractal dimension is less compact. Thus, it has more surface area by which to contact other particles. As a result, the likelihood of colliding fractals (D < 3) is greater than that of colliding spheres (D = 3). As the collision efficiency value is estimated from a set of experimental data, the collision efficiency estimated by the mCFS model generally should be lower than that estimated using the Euclidean model.

For silica, clay, and crude oil, α_{HOMO} values estimated using the Euclidean model remained relatively constant within the mean shear rates tested. This result supported the modeling assumption that α_{HOMO} is primarily a function of particle surface chemistry. Additionally, for oil, silica, and clay, α_{HOMO} values are significantly different from each other. The average α_{HOMO} value for silica (0.01) was an order of magnitude lower than that of clay ($\alpha_{HOMO} = 0.75$) or oil ($\alpha_{HOMO} = 0.25$) aggregation. These results are consistent with the characterization of silica as a non-flocculating sediment and clay as a cohesive sediment.

Values of α_{HOMO} for clay systems estimated using the mCFS model did not remain constant within the mean shear rates tested varying from 0.43 to 0.76. If the mCFS

model represents real systems better than the Euclidean model, then this trend suggests that α_{HOMO} may be dependent both on floc surface chemistry and the arrangement of the floc surface (fractal dimension). Differences in α_{HOMO} values between clay or oil particles may be due to differences in particle structure as well as surface chemistry. The drainage of an aqueous interparticle film is required before aggregation can occur. The work required to aggregate colliding oil droplets includes work to drain the intervening aqueous film and to overcome short range interparticle repulsive forces. Additional work is required due to energy lost as the droplets deform against the resistance of the aqueous film. Conversely, clay particles have significant porosity, which may allow the interaggregate film to drain more easily. This reduced energy requirement may translate into a larger aggregation efficiency value for clay particles.

Despite the added variation, α_{HOMO} values for clay remained significantly higher than that of oil or silica particles. Surface chemistry is the primary cause of different α_{HOMO} values for clay, oil, and silica particles. Clay particles have a weak negative charge, and are attracted to the polarized water molecules, which attract more clay particles. This attraction results in a strong cohesion between clay particles and a relatively high α_{HOMO} value. Oil droplets are cohesive in aqueous systems because of hydrophobic attraction. Theoretical and experimental studies indicate that the reorientation, or restructuring, of water around non-polar surfaces is entropically very unfavorable, since it disrupts the existing water structure and imposes a new and more ordered structure on the surrounding water molecules (Israelachvili, 1992). Silica

particles are not attractive as they do not bind with water molecules. Thus, silica

particles have a low α_{HOMO} value.

In oil-sediment systems, α_{HET} values are similar for clay-oil and silica-oil

systems. Because of the different surface chemistries of the two model sediments, this

result was somewhat surprising. The most likely cause of the increased aggregation

efficiency in the silica-oil systems results from sorption of oil constituents onto the

surface of some of the silica particles. Thus, the interactions become more as a system

of oil monomers with similar α values.

Overall, these collision efficiency results further emphasize that the estimated

α's are dependent on the model employed. In other words, for the given data, two

different values of α were obtained using the two coagulation models (Euclidean and

mCFS). This possibility has been noted previously (O'Melia and Tiller, 1993; Lee *et al.*,

2002).

Fractal Dimension

The results of the parameter estimation using the fractal rectilinear model

indicate that the estimated fractal dimensions were relatively high, D ranged from 2.7-

3.0 (Tables 6.3 and 6.4). These values were close to the Euclidean case (D = 3),

suggesting that the aggregates had a compact structure. Even though the fractal

dimensions from many different systems are broadly reported between 1.0 and 3.0 (Jiang

and Logan, 1991), they often fall between 1.7 and 2.85 (Wiesner, 1992). However, most

of the simulation and experimental studies have focused on the structure of aggregates

formed through Brownian motion. Aggregates formed by fluid shear or differential

sedimentation may have more compact structure (higher D) than those of Brownian

motion. Experimental research (Logan and Wilkinson, 1991; Logan and Kilps, 1995)

using microbial aggregates in shear dominant mixing conditions, generated aggregates

with fractal dimensions as high as 2.66 and 2.99. Particle material homogeneity (i.e.,

sand and clay are different sizes) has also been listed as a factor affecting aggregate

fractal dimension (Lee *et al.*, 2002).

Several different techniques have been previously used to estimate the fractal

dimension. Indirect methods include measurement of properties related to aggregate

size, such as settling velocity and porosity. Direct methods include measurement of

aggregate mass versus size (the slope of the log-log plot being the fractal dimension)

(Jiang and Logan, 1991). Fractal dimensions can also be determined from PSD data.

Figure 6.2 compares the fractal dimensions estimated for aggregates using the PCT

method and parameter estimation method with the mCFS model. As the fractal

dimension decreases from 3.0, values estimated using the PCT method are lower than

those determined using parameter estimation with the mCFS model. The reason for this

discrepancy is not immediately clear. Other researchers have noted that the PCT method

may underestimate fractal dimension over a broad size range (Jackson *et al.*, 1995). The

assumption of constant fractal dimension throughout the size range is violated as the oil

droplets (D = 3) dominate the upper size range while the fractal clay particles (D < 2)

predominate in the lower sizes. Invalid mCFS model assumptions could also have

resulted in overestimated fractal dimensions. The combining rule proposed for
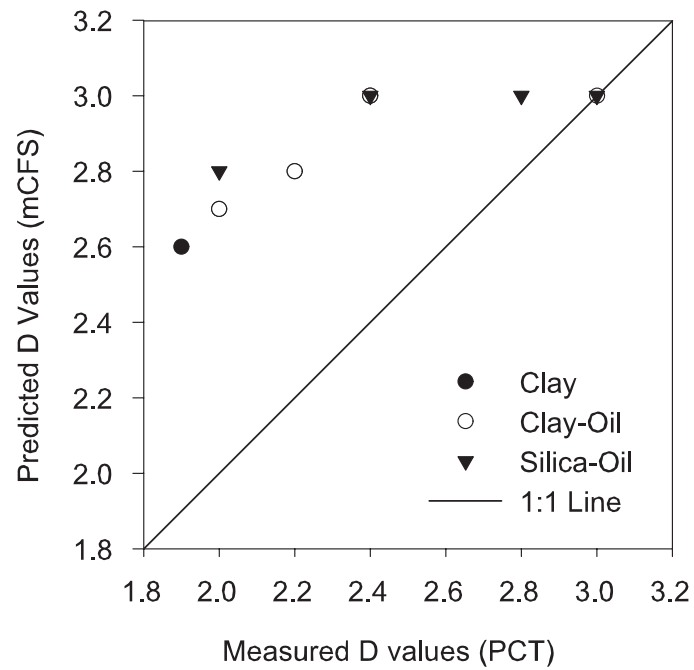
Figure 6.2. Comparison of experimentally measured (PCT) fractal dimension with Euclidean and mCFS estimated fractal dimension

estimating the fractal dimension of a newly formed aggregate forces the fractal dimension of the new aggregate to be an average value of the fractal dimensions of its constituents. This is reasonable in shear systems as fractal objects are believed to restructure to maximize their fractal dimension. However, it is possible that the restructuring is not uniformly applied and that some aggregates maintain a lower fractal dimension. More research in the area of fractal restructuring and mixed monomer type systems is needed.

Figures 6.3a and b show the evolution of clay-oil aggregates in systems with different initial concentrations of clay and oil. At time = 0, the free oil density is represented by a single bar at density = 0.9 while the remaining bars represent various sized clay aggregates (Figures 6.3a and 6.3b). Because of the fractal character of clay, larger aggregates have increased porosity and lowered densities approaching 1.0. In all cases, the volume fractions of particles with densities 0.9 and 2.4 decreased over time as clay and oil aggregate to form flocs with intermediate densities. These patterns of aggregate formation rely on the validity of the fractal dimension combining rule and could not be validated directly through experiment.

To estimate the relative influence of settling velocity and aggregation in "free" oil removal, one can compare the time scales at which each of these processes occurs. Equation 6.15 is written in terms of total volume V with density q

$$\frac{dV_q}{dt} = D_z \frac{\partial^2 V_q}{\partial z^2} - w_{k,q} \frac{\partial V_q}{\partial z} + K'' V_q \left(V - V_q \right) \qquad (6.18)$$

A second order rate expression is used to estimate the loss of "free" oil droplets to aggregation with sediment flocs in a two-particle type mixed batch system:

$$r_{oil\,loss} = \frac{dV_{oil}}{dt} = -K^{"}V_{oil}\left(V - V_{oil}\right) \tag{6.19}$$

Free oil droplets are classified by a conserved density class q. The total particle volume V_q in a given conserved density class q is calculated as the following:

$$V_q = \sum_{k=1}^{c_{volume}} n_{k,q} v_k \tag{6.20}$$

where v_k is the median particle volume in size class k. If $V_{oil} = [A]$ and $V-V_{oil} = [B]$, then the solution of the differential equation 6.19 is given by 6.21.

$$\left(\frac{1}{[B]_o - [A]_o}\right)\ln\left(\frac{[A]_o[B]}{[A][B]_o}\right) = -K^{"}t \tag{6.21}$$

Initial volume concentrations in equation 6.21 are indicated by the subscript o. Apparent second order rate constants, K'', are determined through linear regression of the left hand side of equation 6.21 versus time. Equation 6.18 is nondimensionalized by letting $\psi_q = V_{,q}/V_q(0)$, $\zeta = z/Z$, and $\tau = tw_{k,q}/Z$

$$\frac{d\psi_q}{d\tau} = \frac{D_z}{w_{q,avg}Z}\frac{\partial^2\psi_q}{\partial\zeta^2} - \frac{\partial\psi_q}{\partial\zeta} + \frac{K_q[B]_o\psi_q Z}{w_{q,avg}} \tag{6.22}$$

where Z is a characteristic depth, $[B]_o$ is as defined in equation 6.21, and $w_{q,avg}$ is the volume averaged particle settling velocity as defined in the following:

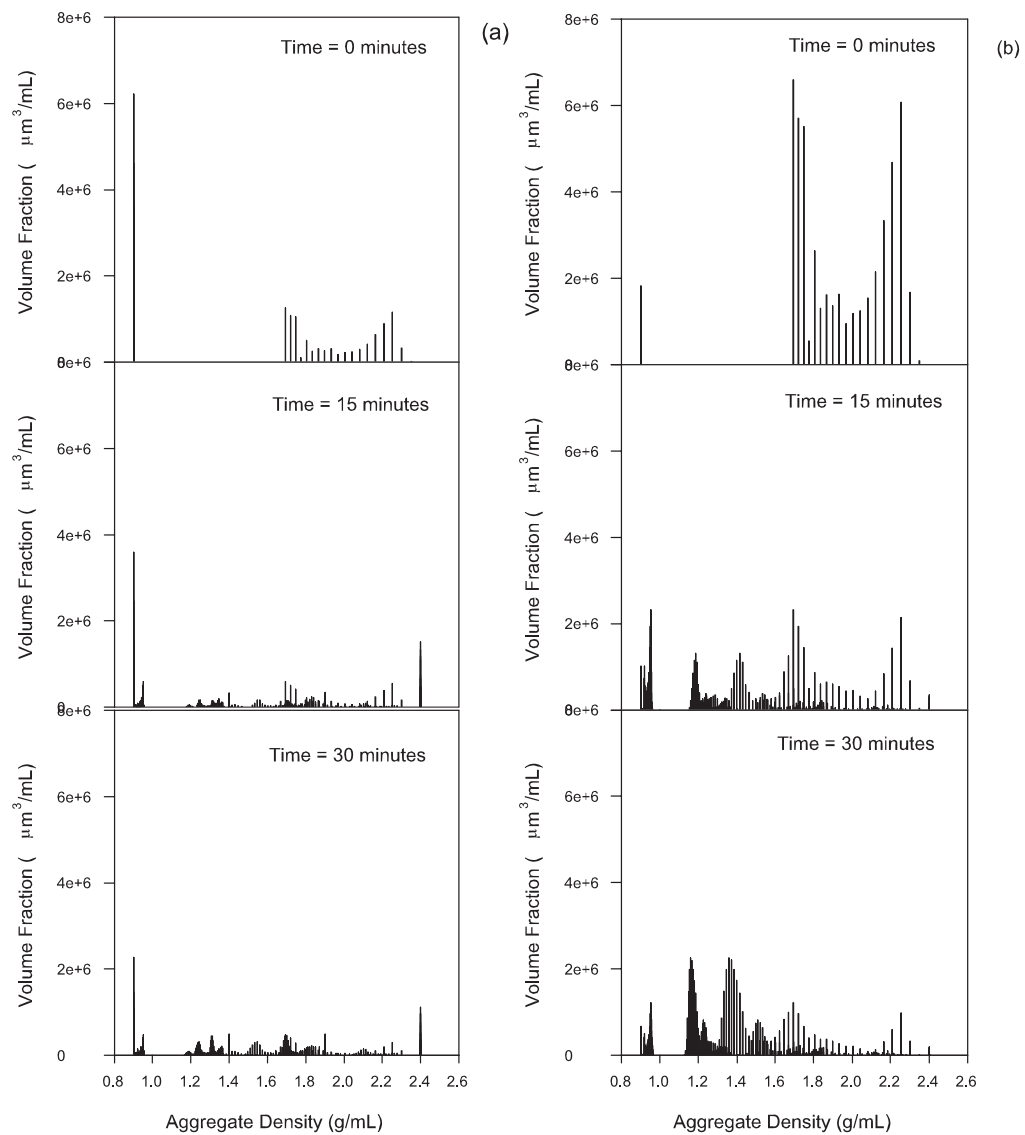$$w_{q,avg} = \frac{1}{V_q}\sum_{k=1}^{c_{volume}} w_{k,q} v_k \tag{6.23}$$

Figure 6.3. Formation of oil-clay flocs with varying fractal dimension D for Experiments (a) G20_Cl08_Oil06 and (b) G20_Cl08_Oil012

For this case, Z is specified as 2m, the mixed layer depth of a coastal estuary. The

quantity ($K_q[B]_o Z /w_{q,avg}$) appearing in equation 6.22 is called the Damköhler number for

convection, Da, and physically represents the ratio

$$Da = \frac{rate\ of\ consumption\ of\ V_q\ by\ reaction}{rate\ of\ transport\ of\ V_q\ by\ convection} = \frac{K_q^{''}[B]_o Z}{w_{q,avg}} \tag{6.24}$$

If Da<<1, then particle settling rates are much faster than the aggregation rates and

aggregation can be ignored with negligible error. Average settling rates were calculated

using equations 6.14 and 6.23. Settling rates for clay flocs and oil-clay aggregation Da

numbers were plotted as a function of mean shear rate (Figure 6.4a-d). When comparing

settling rates and Damköhler numbers of clay using different fractal values, it becomes

clear that more fractal aggregates of a given mass settle more slowly. Thus, the

aggregation Damköhler numbers increase, raising the potential influence of aggregation

in the vertical transport of entrained oil.

Overall, the presented CFS and mCFS aggregation models can be used to study a

number of problems related to sediment and oil aggregation and transport. Natural clay-

oil flocculation after a crude oil spill has been termed surf washing and is of interest in

the spill responder community. Additionally, the transport and fate of physically or

chemically dispersed spilled crude oil and seeped oil in coastal environments can be

more accurately modeled by including potential interactions with suspended sediments.

Accurately describing each of the above scenarios is important in understanding

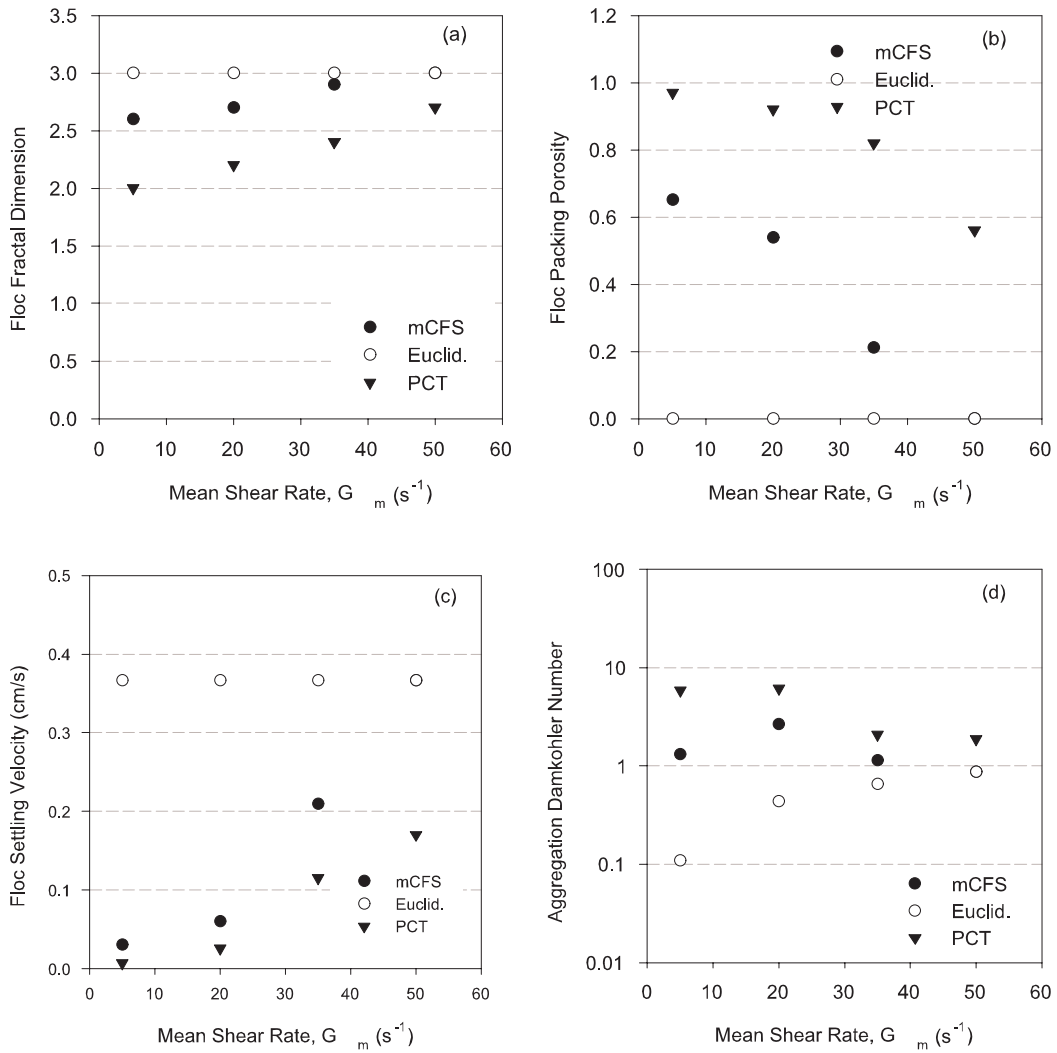ecological risks presented by response countermeasures to an oil spill.

Figure 6.4. Effect of shear on fractal dimensions (a), clay floc porosity (b), clay settling velocity (c) and oil-clay aggregation Damköhler (Da) number (d) in a settling column

This modeling approach would also be useful in describing the flocculation of harmful algal blooms (HABs) and suspended sediments and resulting transport in coastal systems. The modeled aggregation may occur naturally or as a treatment option to remove bacterial blooms from the water surface. Incorporating bacterial transport and their interactions with suspended sediments from sewer outfall release models is another possibility.

CONCLUSIONS

The following conclusions resulted from this study:

1. A mCFS model has been presented to describe formation of multiple particle type flocs in transport and fate models. Estimated values for sediment and crude oil systems can be taken from these experimental data. Aggregation parameters for this model generally can be estimated using laboratory batch studies.

2. Both Euclidean and modified coalesced fractal sphere (mCFS) aggregation models are consistent with clay-oil and silica-oil aggregation data. With decreasing aggregate fractal dimension, MSSRR values are lower with the mCFS model suggesting a better fit with experimental data.

3. In the Euclidean model, homogeneous collision efficiency values (α_{HOMO}) for emulsified crude oil, bentonite clay, and colloidal silica did not change for a given system within the mean shear rates tested ($5 \leq G_m \leq 50 \text{ s}^{-1}$). Heterogeneous collision efficiency values (α_{HET}) for clay-crude oil and silica-crude oil systems also remained constant for a given system in the Euclidean model. However, in

the modified coalesced fractal sphere (mCFS) model, both α_{HOMO} and α_{HET} values decrease with decreasing aggregate fractal dimension.

4. Fractal dimensions (D) for clay, oil, silica, oil-clay, and oil-silica particles were estimated between 2.6-3.0 using the parameter estimation technique. Lower D values were measured using the particle concentration method.

5. The fractal character of clay aggregates reduces its settling velocity and increases the timescale of sedimentation. This increases the aggregation Damköhler number and the relative importance of oil-clay aggregation in the fate of spilled crude oil in the environment.

CHAPTER VII

CONCLUSIONS

Despite the environmental and economic consequences of crude oil in nearshore waters, questions remain related to its transport and fate. Crude oil can be found in coastal areas due to natural seeps or human releases. While crude oil constituents can be "dissolved", the majority of entrained crude oil volume is colloidal. To gain a better understanding of crude oil transport in nearshore waters, a combination of experimental and modeling studies have been conducted.

One of the experimental studies focused on the entrainment of crude oil and the partitioning of crude oil polyaromatic hydrocarbons (PAHs). Crude oil concentrations increased over time according to a first order kinetic model. Generally, the first order rate constant and steady state concentration both increased with increased oil loading and with increased mean shear rate (G_m). In addition, measured PAH concentrations correlated well ($r^2 > 0.96$) with those predicted by a partitioning model.

A second set of experiments focused on the coalescence and resurfacing of crude oil droplets. Thermodynamic and kinetic investigations were performed to determine the influence of coagulation of chemically dispersed crude oil droplets in saline waters. As the DLVO calculated interaction potential values were negative, droplet coagulation was favored thermodynamically. Kinetic experiments illustrated that while mixing energy significantly impacted dispersant efficiency (C/C_o), salinity effects were not significant. Experimentally determined dispersant efficiencies were 10-50% lower than that predicted using a non-interacting droplet model.

A third set of experiments examined the consistency of measurements between in-situ and ex-situ particle sizers. For latex beads or emulsified crude oil systems, all instruments yielded consistent size distributions and fractal dimensions. Mean volume aggregate diameters determined using the FlowCAM were consistently larger that those determined using the LISST-100 or Coulter Multisizer due to aggregate orientations during measurements. Clay-oil aggregates showed higher D_3 values than clay aggregates, suggesting that colloidal oil and mixing shear are dominant factors influencing aggregate morphology in nearshore waters.

To quantify aggregation kinetics and sedimentation rates of oil-sediment flocs, an aggregation and vertical transport model based on coalesced sphere (CS) assumptions was developed. A parameter estimation algorithm was used to estimate homogeneous collision efficiencies (α_{HOMO}) for single particle type systems and heterogeneous collision efficiencies (α_{HET}) for two particle type systems. Clay and crude oil were cohesive particles while silica was noncohesive. Crude oil increases the aggregation of noncohesive particles as shown by similar α_{HET} values for clay-oil (0.4) and silica-oil (0.3) systems. Aggregation Damköhler numbers for clay and oil ranged from 0.1-1.0, suggesting that clay flocculation and oil coalescence may occur on the same timescales as clay sedimentation and oil resurfacing, respectively. For oil in clay-oil systems, aggregation Damköhler numbers ranged from 0.1-1.0, suggesting that oil removal by clay sediment occurs on the same timescale as clay sedimentation.

To incorporate particle morphology effects on aggregation kinetics and sedimentation rates, an aggregation and vertical transport model based on modified

coalesced fractal sphere (mCFS) assumptions was developed. In the parameter estimation algorithm, the minimized objective function, mean of the sum of the squares of the relative residuals (MSSRR), was a relative least squares residual rather than the typical unweighted least squares residual. The mCFS model had MSSRR values up to 15% lower than that obtained using the Euclidean model. For the mCFS model, estimated D values were between 2.6 and 3.0. Values of α_{HOMO} or α_{HET} were also up to 50% lower in the mCFS model than those obtained using the Euclidean model. D values estimated by the mCFS model were lower than that estimated by the Euclidean model but higher than that estimated experimentally by the particle concentration technique (PCT). For a given aggregate mass, reducing an aggregate's fractal dimension lowered its settling velocity. Thus, the timescale of sedimentation becomes greater than that of clay-oil aggregation. Thus, the mCFS model provides clearer insights to the fate of spilled oil in coastal environments.

REFERENCES

Aamo, O.M., Reed, M., Daling, P.S., and Johnson, O. (1993) A laboratory based weathering model for coupling trajectory models. In *Proceedings of the 16th Arctic Marine Oil Spill Program (AMOP),* pp. 617-626. Environment Canada, *Ottawa, Ontario.*

Aamo, O.M., Reed, M., and Downing, K. (1997a) Oil spill contingency and response (OSCAR) model system: sensitivity studies. In *Proceedings of the 1997 International Oil Spill Conference (IOSC),* pp. 429-438. American Petroleum Institute (API), Washington, D.C.

Aamo, O.M., Reed, M., and Lewis, A. (1997b) Regional contingency planning using the OSCAR oil spill contingency and response model. In *Proceedings of the 20th Arctic Marine Oil Spill Program (AMOP),* pp. 373-389. Environment Canada, Ottawa, Ontario.

American Society of Civil Engineers (ASCE). (1996) State of the art review of modeling transport and fate of oil spills. *Journal of Hydraulic Engineering—ASCE*, **122**, 594-609.

Banerjee S. (1987) Calculation of water solubility of organic compounds with UNIFAC-derived parameters. *Environmental Science and Technology,* **19**, 369-370.

Bartha, R. and Atlas, R.M. (1977) The microbiology of aquatic oil spills. *Advances in Applied Microbiology*, **22**, 225-266.

Bassin, N.J. and Ichiye, T. (1977) Flocculation behavior of suspended sediments and oil emulsions. *Journal of Sedimentary Petrology*, **47**, 671-677.

Blondina, G.J., Singer, M.M., Lee, I., Ouano, M.T., Hodgins, M., Tjeerdema, R.S. and Sowby, M.L. (1999) Influence of salinity on petroleum accommodation by dispersants. *Spill Science and Technology Bulletin*, **5**, 127-134.

Bonner, J., Ernest, A., Sanders, S., and Autenrieth, R. (1994) Parameterizing models for contaminanted sediment transport. In *Transport and Transformation of Contaminants Near the Sediment-Water Interface*, eds. J.V. DePinto, W. Lick, and J.F. Paul, pp. 281-306. CRC Press, Boca Raton, FL.

Bragg, J.R. and Yang, S.H. (1995) Clay-oil flocculation and its effects on the rate of natural cleansing in Prince William Sound following the Exxon Valdez oil spill. In *Exxon Valdez Oil Spill—Fate and Effects in Alaskan Waters (ASTM STP*

1219), eds P.G. Wells, J.N. Butler, and J.S. Hughes, pp. 178-214. American Society for Testing and Materials, Philadelphia, PA.

Camp, T.R. and Stein, P.C. (1943) Velocity gradients in laboratory and full-scale systems. *Journal of Boston Society of Civil Engineering, ASCE*, **30**, 219-237.

Daling, P.S., Aamo, O.M., Lewis, A., and Strom-Kristiansen, T. (1997). SINTEF/IKU oil weathering model: predicting oil properties at sea. In *Proceedings of the 1997 Oil Spill Conference*, 297-307. American Petroleum Institute (API), Washington, DC.

Daling, P.S., Brandvik, P.J., and Singsaas, I. (1995) *Weathering of oil and use of dispersants: methods for assessing oils' properties at sea and the feasibility of oil spill dispersants.* NOSCA Seminar on Oil Pollution Control, Malta 31.1-1.2, 7p.

Daling, P.S., Mackay, D., Mackay, N., and Brandvik, P.J. (1990) Droplet size distributions in chemical dispersion of oil-spills—towards a mathematical model. *Oil & Chemical Pollution*, 7, 173-198.

Danov, K.D. Denkov, N.D., Petsev, D.N., Ivanov, I.B., and Borwankar, R. (1993a) Coalescence dynamics of deformable Brownian emulsion droplets. *Langmuir*, **9**, 1731-1740.

Danov, K.D., Ivanov, I.B., Gurkov, T.D., and Borwankar, R.P. (1994) Kinetic-model for the simultaneous processes of flocculation and coalescence in emulsion systems. *Journal of Colloid and Interface Science*, **167**, 8-17.

Danov, K.D., Petsev, D.N., Denkov, N.D., and Borwanker, R. (1993b) Pair interaction energy between deformable drops and bubbles. *Journal of Chemical Physics*, **99**, 7179-7189.

Delvigne, G.A.L. and Sweeney, C.E. (1988) Natural dispersion of oil. *Oil and Chemical Pollution*, **4**, 281-310.

Denkov, N.D., Petsev, D.N., and Danov, K.D. (1993) Interaction between deformable Brownian droplets. *Physics Review Letters*, **71**, 3226-3229.

Dukhin, S., Saether, O., and Sjöblom, J. (2001) Coupling of coalescence and flocculation in dilute o/w emulsions. In *Encyclopedic Handbook of Emulsion Technology*, ed J. Sjöblom, pp.71-94. Marcel Dekker, New York.

Edwards, D.A., Brenner, H. and Wasan, D.T. (1991) *Interfacial Transport Processes and Rheology*, Butterworth-Heinemann, Boston.

Edzwald, J.K., Upchurch, J.B., and O'Melia, C.R. (1974) Coagulation in estuaries. *Environmental Science and Technology*, **8**, 58-63.

Elworthy, P.H., Rogers, J.A., and Florence, A.T. (1971) Stabilization of oil-in-water emulsions by non-ionic detergents. 5. Effect of salts on rates of coalescence in a chlorobenzene emulsion. *Journal of Colloid and Interface Science*, **35**, 23-29.

Ernest, A.N., Bonner, J.S. and Autenrieth, R.L. (1991) Model parameter estimation for particle transport. *Journal of Environmental Engineering*, **117**, 573-594.

Ernest, A.N., Bonner, J.S. and Autenrieth, R.L. (1995) Determination of particle collision efficiencies for flocculent transport models. *Journal of Environmental Engineering*, **121**, 320-329.

Exerowa, D. and Kruglyakov, P.M. (1998) *Foam and Foam Films: Theory, Experiment, Application*. Elsevier, New York.

Farley, K.J. and Morel, F.M.M. (1986) Role of coagulation in the kinetics of sedimentation. *Environmental Science and Technology*, **20**, 187-195.

Feder, J. (1988) *Fractals*. Plenum Press, New York.

Fennesy, M.J., Dyer, K.R., and Huntley, D.A. (1994) INSSEV—an instrument to measure size and settling velocity of flocs in-situ. *Marine Geology*, **117**, 107-117.

Fingas, M. (2000) Use of surfactants for environmental applications. In *Surfactants Fundamentals and Applications in the Petroleum Industry*, ed L.L Schramm, pp. 461-539. Cambridge University Press, Cambridge.

Fingas, M.F., Huang, E., Fieldhouse, B., Wang, L., and J.V. Mullin. (1996) The effect of energy, settling time, and shaking time on the swirling flask dispersant apparatus. *Spill Science and Technology Bulletin*, **3**, 193-194.

Fingas, M.F., Kyle, D.A., Wang, Z., and Ackerman, F. (1994) Testing of oil spill dispersants effectiveness in the laboratory. In *Proceedings of the 17th Arctic and Marine Oilspill Program Technical Seminar*, pp. 905-942. Environment Canada, Ottawa, Ontario.

Friedlander, S.K. (1977) *Smoke, Dust, and Haze*. John Wiley and Sons, New York.

Fugate, D.C. and Friedrichs, C.T. (2002) Determining concentration and fall velocity of estuarine particle populations using ADV, OBS, and LISST. *Continental Shelf Research*, **22**, 1867-1886.

Gartner, J.W., Cheng, R.T., Wang, P.F., and Richter, K. (2001) Laboratory and field evaluations of the LISST-100 instrument for suspended particle size determinations. *Marine Geology*, **175**, 199-219.

Garton, L.S., Bonner, J.S., Ernest, A.N.S., and Autenrieth, R.L. (1996) Fate and transport of PCBs at the New Bedford Harbor superfund site. *Environmental Toxicology and Chemistry*, **15**, 736-745.

George-Ares, A. and Clark, J.R. (2000) Aquatic toxicity of two Corexit® dispersants. *Chemosphere*, **40**, 897-906.

Gibbs, R. and Hopkins, M. (1984) Effects of Solids Concentration and Turbulence upon the Coagulation Rate of Sewage Sludge in Seawater. *Technical Report*, Center for Colloidal Science, College of Marine Studies, University of Delaware, Newark.

Gibbs, R.J. (1983) Coagulation rates of clay-minerals and natural sediments. *Journal of Sedimentary Petrology*, **53**, 1193-1203.

Han, M. and Lawler, D.F. (1992) The (relative) insignificance of G in flocculation. *Journal of American Water Works Association*, **84**, 79-91.

Heffler, D.E., Syvitski, J.P.M., and Asprey, K.W. (1991) The floc camera, In *Principles, Methods, and Application of Particle Size Analysis*, ed J.P.M. Syvitski, pp. 209-221. Cambridge University Press, New York.

Howlett, E. (1998) *Technical Manual: COZOIL for Windows*. Report to US Minerals Management Service. Contract Number 98-0014, 50pp.

Hunt, J.R. and Pandya, J. (1984) Sewage sludge coagulation and settling in seawater. *Environmental Science and Technology*, **18**, 119-121.

Hunter, R.J. (2001) *Foundations of Colloid Science*, Oxford University Press, New York.

Israelachvili, J.N. (1992) *Intermolecular and Surface Forces*, Academic Press Limited, London.

Jackson, G.A. (1998) Using fractal scaling and two-dimensional particle size spectra to calculate coagulation rates for heterogeneous systems. *Journal of Colloid and Interface Science*, **202**, 20-29.

Jackson, G.A., Logan, B.E., Alldredge, A.L., and Dam, H.G. (1995) Combining particle size spectra from a mesocosm experiment measured using photographic and

aperture impedance (Coulter and Elzone) techniques. *Deep-Sea Research II*, **42**, 139-157.

Jiang, Q. (1993) Fractal structure of aggregates induced by shear motion, *Ph.D. dissertation*, University of Arizona, Tucson.

Jiang, Q. and Logan, B.E. (1991) Fractal dimensions of aggregates determined from steady-state size distributions. *Environmental Science and Technology*, **25**, 2031-2038.

Knowles, S.C. and Wells, J.T. (1998) In-situ aggregate analysis camera (ISAAC): a quantitative tool for analyzing fine-grained suspended material. *Limnology and Oceanography*, **43**, 1954-1962.

Lawler, D.F. (1979) A particle approach to thickening. *Ph.D. dissertation*, University of North Carolina at Chapel Hill, Chapel Hill.

Le Floch, S., Guyomarch, J., Merlin, F.X., Stoffyn-Egli, P., Dixon, J., and Lee, K. (2002) The influence of salinity on oil-mineral aggregate formation. *Spill Science and Technology Bulletin*, **8**, 65-71.

Lee, D., Bonner, J.S., Garton, L.S., Ernest, A.N.S., and Autenrieth, R.L. (2000) Modeling coagulation kinetics incorporating fractal theories: a fractal rectilinear approach. *Water Research*, **34**, 1987-2000.

Lee, D., Bonner, J.S., Garton, L.S., Ernest, A.N.S., and Autenrieth, R.L. (2002) Modeling coagulation kinetics incorporating fractal theories: comparison with observed data. *Water Research*, **36**, 1056-1066.

Lee, K. (2002). Oil-particle interactions in aquatic environments: influence on the transport, fate, effect and remediation of oil spills. *Spill Science and Technology Bulletin*, **8**, 3-8.

Lee L.S., Hagwall, M., Delfino, J.J. and Rao, P.S.C. (1992a) Partitioning of polycyclic aromatic hydrocarbons from diesel fuel into water. *Environmental Science and Technology,* **26,** 2104-2110.

Lee L.S., Rao, P.S.C. and Okuda, I. (1992b) Equilibrium partitioning of polycyclic aromatic hydrocarbons from coal tar into water. *Environmental Science and Technology,* **26,** 2110-2115.

Lewis, A., Daling, P.S., Strom-Kristiansen, T., and Brandvik, P.J. (1995) The behavior of Sture blend crude oil spilled at sea and treated with dispersants. In

Proceedings of the 18th Arctic Marine Oil Program (AMOP), pp. 1023-1055. Environment Canada, Ottawa, Ontario.

Li, D. and Ganczarczyk, J. (1989) Fractal geometry of particle aggregates generated in waste and wastewater treatment processes. *Environmental Science and Technology*, **23**, 1385-1389.

Lobo, L., Ivanov, I.B., and Wasan, D.T. (1993) Dispersion coalescence – kinetic stability of creamed dispersions. *AIChE Journal*, **39**, 322-334.

Logan, B.E. and Kilps, J.R. (1995) Fractal dimensions of aggregates formed in different fluid mechanical environments. *Water Research*, **29**, 443-453.

Logan, B.E. and Wilkerson, D.B. (1991) Fractal dimensions and porosities of *Zoogloea ramigera* and *Saccharomyces cerevisae* aggregates. *Biotechnology and Bioengineering*, **38**, 389-396.

Lunel, T. (1993) Dispersion: oil droplet size measurements at sea. In *Proceedings of the 16th Arctic Marine Oil Spill Program (AMOP)*, pp. 1023-1055. Environment Canada, Ottawa, Ontario.

MacDonald, I.R., Guinasso, N.L., Ackleson, S.G., Amos, J.F., Duckworth, R., Sassen, R., and Brooks, J.M. (1993) Natural oil-slicks in the Gulf of Mexico visible from space. *Journal of Geophysical Research-Oceans*, **98,** 16351-16364.

MacDonald, I.R., Leifer, I., Sassen, R., Stine, P., Mitchell, R., and Guinasso, N. (2002) Transfer of hydrocarbons from natural seeps to the water column and atmosphere. *Geofluids*, **2**, 95-107.

Mackay, D., Chau, A., Hossain, K. and M. Bobra. (1984). Measurement and prediction of the effectiveness of oil spill chemical dispersants. In *Oil Spill Chemical Dispersants: Research, Experience, and Recommendations (ASTM STP 840)*, ed T. E. Allen, pp. 38-54. American Society for Testing and Materials, Philadelphia.

Mackay, D., Chau, A., and Poon, Y.C. (1986) A study of the mechanism of chemical dispersion of oil spills. *Publication EE-76*. Environmental Protection Service, Ottawa, Ontario.

Marinova. K.G., Alargova, R.G., Denkov, N.D., Velev, O.D., Petsev, D.N., Ivanov, I.B., and R.P. Borwankar. (1996) Charging of oil-water interfaces due to spontaneous adsorption of hydroxyl ions. *Langmuir*, **12**, 2045-2051.

Mennon, V.B. and Wasan, D.T. (1988) A review of the factors affecting the stability of solids-stabilized emulsions. *Separation Science and Technology,* **23**, 2131-2142.

Mills, M.A., Bonner, J.S., and Autenrieth, R.L. (1999) Method for quantifying the fate of petroleum in the environment. *Chemosphere*, **39**, 2563-2582.

Morel, F.M. and Schiff, S. (1980). *Ocean Disposal of Municipal Wastewater: The Impact on Estuary and Coastal Waters*. MIT Sea Grant College Program, Cambridge, MA.

National Oceanic and Atmospheric Administration (NOAA). (1994). *ADIOS, Automated Data Inquiry for Oil Spills, User's Manual*. NOAA/Hazardous Materials Response and Assessment Division, Seattle, WA.

National Research Council (NRC). (1989) *Using Oil Dispersants on the Sea*. National Academy Press, Washington, D.C.

National Research Council (NRC). (2003) *Oil in the Sea III: Inputs, Fates, and Effects*. National Academy Press, Washington, D.C.

Neff, J.M. (1979) *Polycyclic Aromatic Hydrocarbons in the Aquatic Environment Sources, Fates and Biological Effects*. Applied Science Publishers Ltd., London.

Nelson, J.A., Crookes, R.J., and Simons, S. (1990) On obtaining the fractal dimension of a 3D-cluster from its projection on a plane—application to smoke agglomerates. *Journal of Physics D—Applied Physics*, **23**, 465-468.

O'Melia, C.R. and Tiller, C.L. (1993) Physicochemical aggregation and deposition in aquatic environments, In *Environmental Particles II*, eds J. Buffle and H.P. van Leeuwen, pp. 353-386. Lewis Publishing, Boca Raton, FL.

Page, C.A., Bonner, J.S., McDonald, T.J., and Autenrieth, R.L. (2003) Behavior of a chemically-dispersed oil in a wetland environment. *Water Research,* **36**, 3821-3833.

Page, C.A., Bonner, J.S., Sumner, P.L., and Autenrieth, R.L. (2000a) Solubility of petroleum hydrocarbons in oil/water systems. *Marine Chemistry*, **70**, 79-87.

Page, C.A., Bonner, J.S., Sumner, P.L., McDonald, T.J., Autenrieth, R.L., and Fuller, C.B. (2000b) Behavior of a chemically-dispersed oil and a whole oil in a near-shore environment. *Water Research*, **34**, 2507-2516.

Pao, J.R., Chang, Y.C., and Gentry, J.W. (1990) The use of simulated fractals to determine the relation between a cluster and its projection. *Journal of Aerosol Science*, **21**, S63-S66.

Reed, M., Aamo, O.M., and Daling, P.S. (1995a) Quantitative analysis of alternate oil spill response strategies using OSCAR. *Spill Science and Technology Bulletin*, **2**, 67-74.

Reed, M., Ekrol, N., Rye, H., and Turner, L. (1999a). Oil spill contingency and response (OSCAR) analysis in support of environmental impact offshore Namibia, *Spill Science and Technology Bulletin*, **5**, 29-38.

Reed, M., French, D., Rines, H., and Rye, H. (1995b) A three-dimensional oil and chemical spill model for environmental impact assessment, In *Proceedings of the 1995 International Oil Spill Conference*, pp. 61-63. American Petroleum Institute (API), Washington, D.C.

Reed, M., Gundlach, E., and Kanay, T. (1989) A coastal zone oil spill model: development and sensitivity studies. *Oil and Chemical Pollution*, **5**, 411-449.

Reed, M., Johansen, O., Brandvik, P.J., Daling, P., Lewis, A., Fiocco, R., Mackay, D., and Prentki, R. (1999b) Oil spill modeling towards the close of the 20th century: overview of the state of the art. *Spill Science and Technology Bulletin*, **5**, 3-16.

Serra T, and Logan B.E. (1999) Collision frequencies of fractal bacterial aggregates with small particles in a sheared fluid. *Environmental Science and Technology,* **33**, 2247-2251.

Shaw, D. and Reidy, S. (1979) Chemical and size fractionation of aqueous petroleum dispersions. *Environmental Science and Technology,* **13**, 1259-1263.

Shiu, W.Y., Bobra, M., Maijanen, A., Suntio, L., and Mackay, D. (1990) The water solubility of crude oils and petroleum products. *Oil and Chemical Pollution*, **7**, 57-84.

Sieracki, C.K. and Sieracki, M.E. (1999) Results of continuous and discrete FlowCAM measurements of plankton community structure, Boothbay Harbor, Maine, USA. In *Proceedings of ASLO/AGU Ocean Sciences Meeting*, p. 45. American Geophysical Union (AGU), Washington D.C.

Sieracki, C.K., Sieracki, M.E., and Yentsch, C.S. (1998) An imaging in-flow system for automated analysis of marine microplankton. *Marine Ecology Progress*, **168**, 285-296.

Smoluchowski, M. (1917) Versuch einer mathematiischer theorie der koagulation kinetic kolloides lasungen. *Zeitschrift Fur Physikalische Chemie—Leipzig*, **92**, 128-168.

Spaulding, M. (1988) A state of the art review of oil spill trajectory and fate modeling. *Oil and Chemical Pollution*, **4**, 39-55.

Spaulding, M., Odulo, A., and Kolluru, V. (1992) A hybrid model to predict the entrainment and subsurface transport of oil. In *Proceedings of the 15th Arctic Marine Oil Spill Program (AMOP)*, pp. 67-92. Environment Canada, Ottawa, Ontario.

Sterling, M.C., Bonner, J.S., Ojo, T., Page, C.A., Ernest, A.N.S., and Autenrieth, R.L. (2002) Coalescence kinetics of dispersed crude oil in a laboratory reactor. In *Proceedings of the 25th Arctic Marine Oil Spill Program (AMOP)*, pp. 741-754. Environment Canada, Ottawa, Ontario.

Stoll, S. and Buffle, J. (1996) Computer simulation of bridging flocculation processes: the role of colloid to polymer concentration ratio on aggregation kinetics. *Journal of Colloid and Interface Science*, **180,** 548-563.

Stumm, W. and Morgan, J.J. (1995) *Aquatic Chemistry: Chemical Equilibria and Rates in Natural Waters*, Wiley, New York.

Tambo, N. and Francois, R.J. (1991) Mixing, breakup, and aggregate characteristics. In *Mixing in Coagulation and Flocculation*, eds A. Amirtharajah and M. Clark, pp. 647-702. American Water Works Association (AWWA), Denver, CO.

Thouy, R. and Jullien, R. (1994) A cluster-cluster aggregation model with tunable fractal dimension. *Journal of Physics A—Mathematical and General*, **27**, 2953-2963.

Turner, J.S. (1973) *Buoyancy Effects in Fluids*. Cambridge University Press, New York.

U.S. Coast Guard (USCG). (1987) *Polluting Incidents In and Around U.S. Waters. Calendar Year 1983 and 1984.* COMDTINST M16450.2G. U.S. Department of Transportation, Washington, D.C.

Valkovska, D.S., Danov, K.D., and Ivanov, I.B. (1999) Surfactants role on the deformation of colliding small bubbles. *Colloids and Surfaces A—Physicochemical and Engineering Aspects*, **156**, 547-566.

Van Oss, C.J. (1994) *Interfacial Forces in Aqueous Media*, Marcel Decker, New York.

Vicsek, T. (1992) *Fractal Growth Phenomena*, World Scientific, River Edge, NJ.

Wells, P.G., Anderson, J.W., and Mackay, D. (1984) Uniform methods for exposure regimes in aquatic toxicology experiments with chemically dispersed oils. In *Oil Spill Chemical Dispersants: Research, Experience, and Recommendations (STP*

840), ed T.E. Allen, pp. 23-37. American Society for Testing and Materials, Philadelphia.

Wiesner, M.R. (1992) Kinetics of aggregate formation in rapid mix. *Water Research*, **26**, 379-387.

Xie W.H, Shiu W.Y. and Mackay D. (1997) A review of the effect of salts on the solubility of organic compounds in seawater. *Marine Environmental Research*, **44**, 429-444.

Zheng, L. and Yapa, P.D. (2000) Buoyant velocity of spherical and nonspherical bubbles/droplets. *Journal of Hydraulic Engineering*, **126**, 852-854.

VITA

Name:	Michael Conroy Sterling, Jr.
Current Address:	3309 Longleaf Circle College Station, TX 77845
Permanent Address:	230 Winding Oaks Waco, TX 76705
Education:	Bachelor of Science 1994 Chemical Engineering The University of Oklahoma Norman, OK
	Master of Science 1998 Agricultural Engineering Texas A&M University College Station, TX
	Doctor of Philosophy 2003 Civil Engineering Texas A&M University College Station, TX